

Andreev bound states in potentially topological setups

Barakov, H.S.

DOI

[10.4233/uuid:7bde9932-e775-431d-8dc0-34623b9eb5fc](https://doi.org/10.4233/uuid:7bde9932-e775-431d-8dc0-34623b9eb5fc)

Publication date

2022

Document Version

Final published version

Citation (APA)

Barakov, H. S. (2022). *Andreev bound states in potentially topological setups*. [Dissertation (TU Delft), Delft University of Technology]. <https://doi.org/10.4233/uuid:7bde9932-e775-431d-8dc0-34623b9eb5fc>

Important note

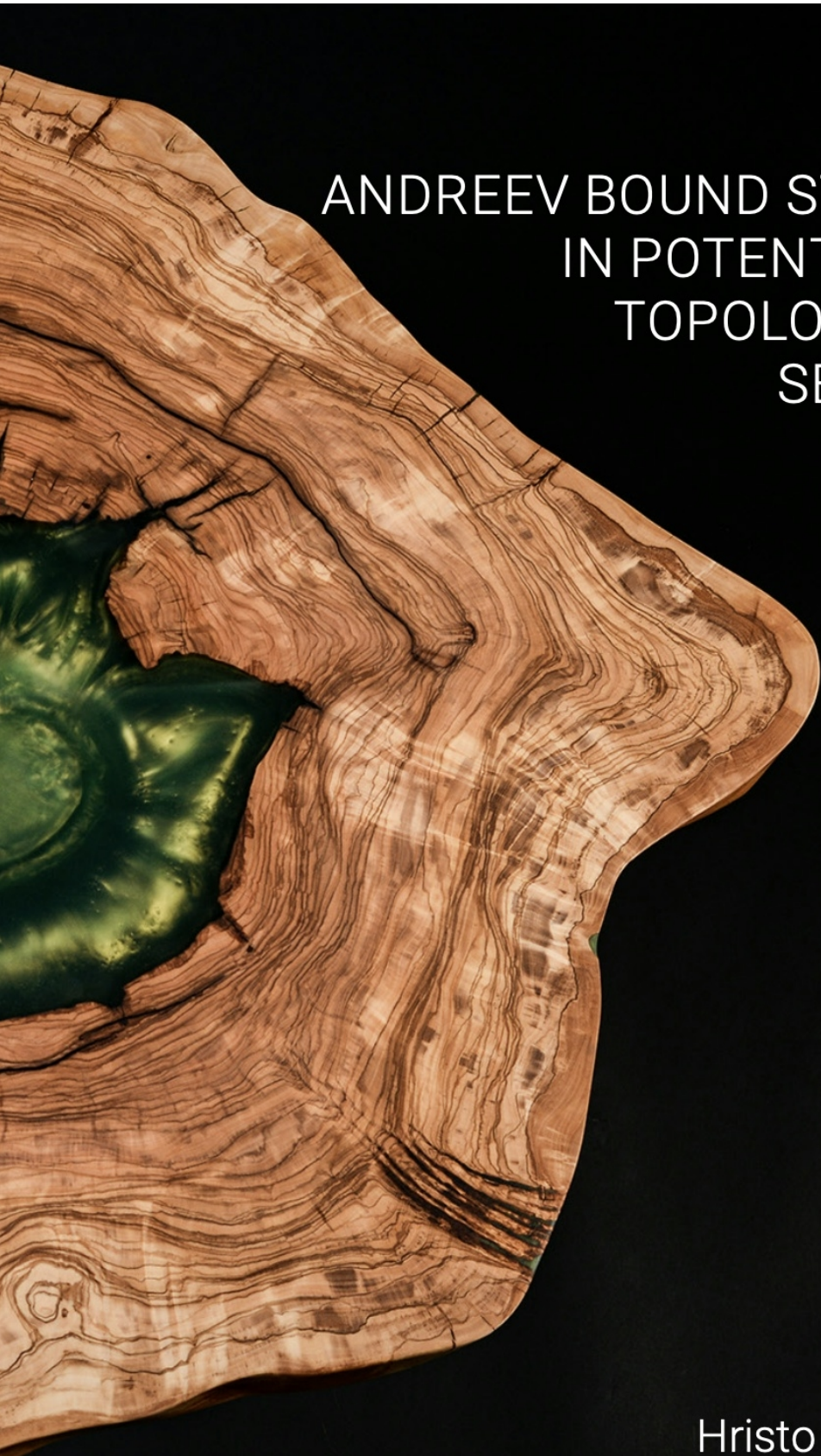
To cite this publication, please use the final published version (if applicable).
Please check the document version above.

Copyright

Other than for strictly personal use, it is not permitted to download, forward or distribute the text or part of it, without the consent of the author(s) and/or copyright holder(s), unless the work is under an open content license such as Creative Commons.

Takedown policy

Please contact us and provide details if you believe this document breaches copyrights.
We will remove access to the work immediately and investigate your claim.

A piece of wood with a green resin inlay, shaped like a head in profile. The wood grain is visible, and the resin is a vibrant green color. The shape is a stylized head in profile, facing right. The wood is light brown with dark, wavy grain patterns. The resin is a vibrant green color, filling a cavity in the wood. The overall shape is a head in profile, facing right.

ANDREEV BOUND STATES IN POTENTIALLY TOPOLOGICAL SETUPS

Hristo Barakov

ANDREEV BOUND STATES IN POTENTIALLY TOPOLOGICAL SETUPS

ANDREEV BOUND STATES IN POTENTIALLY TOPOLOGICAL SETUPS

Dissertation

for the purpose of obtaining the degree of doctor
at Delft University of Technology
by the authority of the Rector Magnificus, Prof.dr.ir. T.H.J.J. van der Hagen,
chair of the Board for Doctorates
to be defended publicly on
Monday 23 May 2022 at 17:30 o'clock

by

Hristo Sabev BARAKOV

Master of Science in Physics,
Université Grenoble Alpes, Grenoble, France,
born in Karlovo, Bulgaria.

This dissertation has been approved by the promotor

promotor: Prof. dr. Y. V. Nazarov

promotor: Prof. dr. Y. M. Blanter

Composition of the doctoral committee:

Rector Magnificus,

Prof. dr. Y. V. Nazarov

Prof. dr. Y. M. Blanter

chairperson

Delft University of Technology, promotor

Delft University of Technology, promotor

Independent members:

Prof. dr. A. Altland

Prof. dr. A. L. Yeyati

Prof. dr. ir. C. H. van der Wal

Prof. dr. J. M. Thijssen

Assoc. Prof. dr. V. Cheianov

Prof. dr. A. F. Otto

University of Cologne, Germany

Universidad Autónoma de Madrid, Spain

University of Groningen, Netherlands

Delft University of Technology

Leiden University, Netherlands

Delft University of Technology, reserve member



European Research Council
Established by the European Commission

Keywords: superconductivity, Andreev bound states, nanostructures, Random Matrix Theory, Quantum Circuit Theory

Printed by: Gildeprint

Front & Back: Top view of an epoxy olive wood table made by the author.

Copyright © 2022 by H. S. Barakov

Casimir PhD Series, Delft-Leiden 2022-12

ISBN 978-90-8593-523-0

An electronic version of this dissertation is available at
<http://repository.tudelft.nl/>.

To my family and friends

CONTENTS

Summary	ix
Samenvatting	xi
1 Introduction	1
1.1 Preface	2
1.2 Superconductivity	3
1.3 Quantum transport	5
1.4 Topology	7
1.5 Random Matrix Theory	10
1.6 Quantum Circuit theory	13
1.7 Structure of this thesis	15
2 Fine energy splitting of overlapping Andreev bound states in multiterminal superconducting nanostructures	21
3 Overlapping Andreev states in semiconducting nanowires: Competition of one-dimensional and three-dimensional propagation	33
3.1 introduction	34
3.2 The setup and model	37
3.3 Uniform nanowire	39
3.4 Scattering Approach	40
3.5 overview of the ABS spectrum	43
3.6 Strong 1D hybridization	44
3.7 Weak 1D hybridization: perturbation theory	46
3.8 Interference at $L \simeq \xi_w$	47
3.9 Upper ABS merging with the continuum	47
3.10 Ballistic junctions	50
3.11 Competition between 1D and 3D propagation	52
3.12 Conclusions	57
4 Supercurrent in the presence of direct transmission and a resonant localized state	63
4.1 Scope, style and structure of the chapter	64
4.2 Short summary of experimental observations	64
4.3 The motivation and essence of the model	65
4.4 Hamiltonians	68
4.4.1 The single dot	68
4.4.2 The leads	69
4.4.3 Tunnel coupling	69

4.5	Normal transport for many dots	69
4.6	Normal transport for two dots.	72
4.7	Normal transport examples	77
4.8	Superconducting transport	80
4.9	Numerical details.	84
4.10	Conclusions	87
5	Abundance of Weyl points in semiclassical multi-terminal superconducting nanostructures	93
5.1	Supplemental Material	101
5.2	Activity A: density and charge correlations of WP in a uniform parameter space.	101
5.3	Activity B: finding I_c in quantum circuit theory	103
5.3.1	The action, mean level spacing, and the velocity correlator	103
5.3.2	Semiclassics: saddle point	104
5.3.3	Semiclassics: correlations	106
5.3.4	Close points	107
5.3.5	Resulting relation.	109
5.4	Activity C: WP positions for ballistic cross	110
	Acknowledgements	119
	Curriculum Vitæ	121
	List of Publications	123

SUMMARY

Since the discovery of Josephson effect there has been a continuously growing interest in the fundamental physics and the applications of this effect. A variety of circuit designs has been developed for application ranging from medical sensors to quantum computing. The fundamental characteristics of Josephson junctions are generally encoded in the discrete spectrum of Andreev Bound States (ABS). These states lie in the energy gap of the spectrum of the bulk superconducting electrodes. While they are localized at the junction they can extend to the electrodes as well. This thesis deals with ABS in different configurations, set-ups of interest and specifically designed structures.

In Chapter 2 and 3, we examine a recently proposed three-terminal setup that encompasses two single-channel junctions that are formed by connecting three superconducting leads with a semi-conducting nanowire, a material combination that has been extensively used in a quest to reveal topologically protected Majorana states in superconducting nanostructures.

In Chapter 2, we concentrate on a situation where two single ABS have close energies which enables them to hybridize and form a superposition, the so-called Andreev molecule. The overlap between these two happens in the middle lead and the energy splitting must cease exponentially under the condition that the length of the lead is much bigger than the superconducting correlation length. We discovered that it is an interference phenomenon related to mesoscopic conductance fluctuations. Such fluctuations develop in the lead on the scale of ABS overlap that encompasses a large number of quantum channels. We quantify the energy splitting δE at the degeneracy point of two ABS which is substantially smaller than the superconducting gap, Δ . This, in turn, makes this energy splitting fine at the Δ scale, enabling interesting quantum manipulation protocols.

In Chapter 3 we examine the setup under more general conditions, so that the assumption of quick electron transfer from the nanowire to the lead is relaxed. The electrons can stay in the nanowire long enough to propagate through the junctions without escaping to the lead, if the contact between the nanowire and the superconducting lead is not perfect. The ABS may overlap in the nanowire rather than in the lead, in this situation the hybridization is substantially stronger. We investigate and analyze a number of regimes where either one-dimensional or three-dimensional propagation dominates, or they compete with each other. We present the spectra for different lengths, detailing the transition from a single-ABS in the regime of strong 1D hybridization to two almost independent ABS hybridized at the degeneracy points, in the regime of weak 1D hybridization. We present the details of merging the upper ABS with the continuous spectrum upon decreasing L . We study in detail the effect of quantum interference due to the phase accumulated during the electron passage between the junctions. We develop a perturbation theory for analytical treatment of hybridization. We address an interesting separate case of fully transparent junctions. We derive and exemplify a perturbation theory suitable for the competition regime demonstrating the interference of 1D and two 3D transmission amplitudes.

In Chapter 4, we turn to a different setup that still includes a nanowire yet involves only

two superconducting electrodes. Motivated by experimental observations, we formulate a model that combines the electron propagation in a quantum channel with an arbitrary transmission, and that through a localized state. The energy of the localized state is affected by the gate voltage and we expect a drastic modification of transport properties of the junction in a narrow interval of the gate voltages of the order of the energy broadening of the localized state and the superconducting energy gap. In normal state, we find that the model may describe both peak and dip in the transmission at resonant gate voltage. Spin splitting splits the positions of these peculiarities. Fano interference of the transmission amplitudes results in an asymmetric shape of the peaks/dips. In superconducting state, the spin splitting results in a complex dependence of the superconducting current on the superconducting phase. In several cases, this is manifested as a pair of $0 - \pi$ transitions in the narrow interval of gate voltages.

In contrast to previous chapters, where we concentrate on concrete setups, we consider in Chapter 5 a general multi-terminal semiclassical nanostructure. Recently, such structures have been predicted to host topological singularities – Weyl Points – in the spectrum of ABS. We address the gapless continuous spectrum at the finer level of discrete states to reveal the abundance of zero-energy Weyl points. We investigate their average density and their parametric correlations relating them to the universal parameter l_c governing the correlations in Random matrix ensemble. Next, we show how to compute the density and the correlations for any setups that can be treated with Quantum Circuit Theory. The problem required a creative combination of numerical and analytical methods.

SAMENVATTING

Sinds de ontdekking van het Josephson-effect is er een voortdurend groeiende belangstelling voor de fundamentele fysica en de toepassingen van dit effect. Er is een verscheidenheid aan circuitontwerpen ontwikkeld voor toepassingen, variërend van medische sensoren tot kwantumcomputers. De fundamentele kenmerken van Josephson-knooppunten zijn over het algemeen gecodeerd in het discrete spectrum van Andreev Bound States (ABS). Deze toestanden liggen in de energiekloof van het spectrum van de bulk supergeleidende elektroden. Hoewel ze op de kruising zijn gelokaliseerd, kunnen ze zich ook naar de elektroden uitstrekken.

Dit proefschrift behandelt ABS in verschillende configuraties, interessante opstellingen en specifiek ontworpen structuren.

In Hoofdstuk 2 en 3 onderzoeken we een recentelijk voorgestelde opstelling met drie terminals die twee enkelkanaals juncties omvat die worden gevormd door drie supergeleidende draden te verbinden met een halfgeleidende nanodraad, een materiaalcombinatie die op grote schaal is gebruikt in een zoektocht om te onthullen topologisch beschermde Majorana-staten in supergeleidende nanostructuren.

In hoofdstuk 2 concentreren we ons op een situatie waarin twee enkelvoudige ABS's nauwe energieën hebben die hen in staat stellen te hybridiseren en een superpositie te vormen, het zogenaamde Andreev-molecuul. De overlap tussen deze twee vindt plaats in de middelste leiding en de energiesplitsing moet exponentieel stoppen onder de voorwaarde dat de lengte van de leiding veel groter is dan de supergeleidende correlatielengte. We ontdekten dat het een interferentieverschijnsel is dat verband houdt met mesoscopische geleidingsfluctuaties. Dergelijke fluctuaties ontwikkelen zich in de hoofdrol op de schaal van ABS-overlap die een groot aantal kwantumkanalen omvat. We kwantificeren de energiesplitsing δE op het degeneratiepunt van twee ABS, dat aanzienlijk kleiner is dan de supergeleidende kloof, Δ . Dit zorgt er op zijn beurt voor dat deze energiesplitsing prima is op de Δ -schaal, wat interessante kwantummanipulatieprotocollen mogelijk maakt.

In Hoofdstuk 3 onderzoeken we de opstelling onder meer algemene omstandigheden, zodat de aanname van snelle elektronenoverdracht van de nanodraad naar de leiding versoepeld wordt. De elektronen kunnen lang genoeg in de nanodraad blijven om zich door de juncties voort te planten zonder naar de lead te ontsnappen, als het contact tussen de nanodraad en de supergeleidende lead niet perfect is. Het ABS kan in deze situatie overlappen in de nanodraad in plaats van de leiding, de hybridisatie is aanzienlijk sterker. We onderzoeken en analyseren een aantal regimes waar ofwel eendimensionale ofwel driedimensionale verspreiding domineert, of ze met elkaar concurreren. We presenteren de spectra voor verschillende lengtes en beschrijven de overgang van een enkel-ABS in het regime van sterke 1D-hybridisatie naar twee bijna onafhankelijke ABS gehybridiseerd op de degeneratiepunten, in het regime van zwakke 1D-hybridisatie. We presenteren de details van het samenvoegen van het bovenste ABS met het continue spectrum bij het verlagen van L . We bestuderen in detail het effect van kwantuminterferentie als gevolg van de fase die wordt geaccumuleerd tijdens de elektronenpassage tussen de juncties. We ontwikkelen

een storingstheorie voor de analytische behandeling van hybridisatie. We behandelen een interessant afzonderlijk geval van volledig transparante kruispunten. We leiden en illustreren een verstoringstheorie die geschikt is voor het concurrentieregime en die de interferentie van 1D- en twee 3D-transmissie-amplitudes aantoonst.

In Hoofdstuk 4 gaan we naar een andere opstelling die nog steeds een nanodraad bevat maar slechts twee supergeleidende elektroden omvat. Gemotiveerd door experimentele waarnemingen formuleren we een model dat de elektronenvoortplanting in een kwantumkanaal combineert met een willekeurige transmissie, en dat via een gelokaliseerde toestand. De energie van de gelokaliseerde toestand wordt beïnvloed door de poortspanning en we verwachten een drastische wijziging van de transporteigenschappen van de junctie in een smal interval van de poortspanningen in de orde van de energieverbreiding van de gelokaliseerde toestand en de supergeleidende energiekloof. In normale toestand vinden we dat het model zowel piek als dip in de transmissie bij resonantiepoortspanning kan beschrijven. Spinsplitsing splitst de posities van deze eigenaardigheden. Fano-interferentie van de transmissieamplitudes resulteert in een asymmetrische vorm van de pieken/dips. In supergeleidende toestand resulteert de spinsplitsing in een complexe afhankelijkheid van de supergeleidende stroom op de supergeleidende fase. In verschillende gevallen manifesteert dit zich als een paar $0 - \pi$ overgangen in het smalle interval van poortspanningen.

In tegenstelling tot voorgaande hoofdstukken, waar we ons concentreren op concrete opstellingen, beschouwen we in Hoofdstuk 5 een algemene multi-terminale semiklassieke nanostructuur. Onlangs is voorspeld dat dergelijke structuren topologische singulariteiten - Weyl-punten - in het spectrum van ABS bevatten. We behandelen het gapless continuospectrum op het fijnere niveau van discrete toestanden om de overvloed aan nul-energie Weyl-punten te onthullen. We onderzoeken hun gemiddelde dichtheid en hun parametrische correlaties die deze relateren aan de universele parameter l_c die de correlaties in het Random matrix ensemble bepaalt. Vervolgens laten we zien hoe we de dichtheid en de correlaties kunnen berekenen voor alle opstellingen die kunnen worden behandeld met Quantum Circuit Theory. Het probleem vereiste een creatieve combinatie van numerieke en analytische methoden.

1

INTRODUCTION

An abnormal reaction to an abnormal situation is normal behaviour.

Victor Frankl, Man's Search for Meaning

1.1. PREFACE

This Section represents a recollection of memories of the candidate and how I became interested in the subjects of this thesis. When I look back on my scientific journey, it has become evident how I ended up interested in the subjects of this thesis. My first real life experience with research started with an internship on experimental techniques of Nuclear-Magnetic Resonance (NMR) of high temperature and nematic order superconductors. I admit knowing a few of those words but none of the concepts at that time. Nevertheless, I was immediately fascinated by two observations. The first being, the discrepancy in size of the apparatus used, compared to the investigated sample. The magnets together with the cryogenic set-up were as big as a normal room, while the sample was at most the size of a small human nail. Second, superconductivity seemed to be the bridge between touchable classical objects and fantasy quantum mechanical phenomena. During my internship, I got into first contact with a variety of condensed matter physics topics such as simple calculation of $1/2$ spin precession, concepts of statistical physics, superconducting magnetic coils in cryogenic set-ups, resonant circuit and high-frequency measurements.

But first and foremost were the concepts of superfluidity and superconductivity, both discovered by the Dutch scientist Heike Kamerlingh Onnes. First in 1908 liquefying helium with a boiling temperature at 4.2 K and thereby pioneering low temperature research. In 1911, when performing resistance measurements on mercury, he observed that the resistance disappears at around 4. K [13]. The first microscopic theory was provided John Bardeen, Leon Cooper, and John Robert Schrieffer (BCS) [6, 7] and it was described as a phonon mediated interaction that led to a formation of cooper pairs. Huge progress has been made since and although the theory provided some explanation, satisfactory theories are still missing for high temperature [37], nematic order [15] and topological [28] superconductors.

Expulsion of magnetic fields and indefinitely persistent currents have led to a plethora of technological applications such as Maglev trains that levitate using superconducting electromagnets. In addition, high-energy particle accelerator laboratories (CERN), single particle (photon) superconducting detectors and fast digital circuits (quantum candidates for quantum computers). An intriguing proposition was made by Brian Josephson in 1962 [19], who predicted theoretically that pairs of electrons could tunnel through a non-superconducting barrier, sandwiched between two superconductors. In the considered case, there exists a discrete bound state, called Andreev Bound State (ABS), that is formed in the junction whose energy depends on the 2π -periodic phase difference between the two superconductors.

This last decade has seen an unprecedented interest in topological concepts applied to condensed matter systems. This spanned the whole field of topological band theory of solids and gave rise to a plethora of examples of topological realizations such as topological superconductors, topological insulators and topological semi-metals. Although from a theoretical point of view these were fascinating, their experimental realization is notoriously difficult. Furthermore solids are limited to the 3 dimensional space while topological non-Abelian quantities are of higher dimension ($d \geq 5$). The latter ones excite the scientific community as a possible candidates for non-abelian topological quantum computing. An analogy between the band structure of solids and Andreev bound states was established which opened up the possibility to model and simulate higher dimensional band structures using conventional materials in multi-terminal superconducting nanostructures.

In the remainder of this chapter, we outline the general framework of this thesis by

providing concise exposition of the used concepts. We start by reminding BCS theory of superconductivity and scattering formalism in order to set up the ground for superconducting heterostructures and describe the discrete ABS spectrum. Finally, we dwell into Random Matrix Theory and Quantum Circuit Theory with the goal to describe statistics of singularities in nanostructures containing multiple channels.

1.2. SUPERCONDUCTIVITY

Superconductivity is an ordered electronic state caused by an indirect electron-electron interaction. Its origin is due to a direct electron-phonon interaction described by

$$\mathcal{H}_{\text{el-ph}} = \sum_{kq} D_{kq} c_{k+q}^\dagger c_k (a_q - a_{-q}^\dagger), \quad (1.1)$$

where c^\dagger, c are electron creation, annihilation operators and a^\dagger, a are phonon creation and annihilation operators, with k being the electron momenta and q the momenta of phonons [22]. The phonon induced interaction is attractive in an energy shell of the order of Debye energy $\hbar\omega_D$ around the Fermi level. An electron polarizes the lattice while another one interacts with the polarization.

It has been derived by Cooper, that this interaction will lead to the formation of bound electron pairs, today called Cooper pairs [12]. His model provided the hint that the Fermi sea (the free electron gas) is unstable whenever small interactive interaction is present among electrons. In the language of second quantization, Cooper pairs can be represented by a creation operator $Z_k^\dagger = c_{k\uparrow}^\dagger c_{-k,\downarrow}^\dagger$ with total spin equal to zero and total momentum equal to zero, where c^\dagger and c are fermionic creation and annihilation operators with spin and momenta.

In 1957, John Bardeen, Leon Cooper, and John Robert Schrieffer proposed a microscopic theory of superconductivity which is known as BCS [6, 7]. The BCS Hamiltonian is

$$\mathcal{H}_{\text{BCS}} = \sum_k \epsilon_k \left(c_{k\uparrow}^\dagger c_{k\uparrow} + c_{-k\uparrow}^\dagger c_{-k\uparrow} \right) + \sum_{kk'} U_{kk'} Z_k^\dagger Z_{k'}, \quad (1.2)$$

where $\epsilon_k = E_k - \mu = (\hbar^2 k^2 / 2m) - \mu$ is the single particle energy measured from Fermi level [17]. They proposed a variational ansatz for the superconducting ground state

$$|\Psi_{\text{BCS}}\rangle = \prod_k (u_k + v_k Z_k^\dagger) |0\rangle \quad (1.3)$$

with the normalization condition $u_k^2 + v_k^2 = 1$, $|0\rangle$ being the vacuum state and v_k, u_k represents the probability amplitude that a state is occupied/unoccupied. In order to determine u_k and v_k , one minimizes $W_S = \langle \Psi_{\text{BCS}} | \mathcal{H}_{\text{BCS}} | \Psi_{\text{BCS}} \rangle$ with respect to u_k and v_k which results into the variational condition

$$2\epsilon_k u_k v_k - \Delta_k (u_k^2 - v_k^2) = 0 \quad (1.4)$$

with the gap parameters being $\Delta_k = -\sum_{k'} U_{kk'} u_{k'} v_{k'}$. Combining self-consistency together with the normalization condition, one finds

$$u_k^2 = \frac{1}{2} \left[1 + \frac{\epsilon_k}{\sqrt{\epsilon_k^2 + \Delta_k^2}} \right] \quad v_k^2 = \frac{1}{2} \left[1 - \frac{\epsilon_k}{\sqrt{\epsilon_k^2 + \Delta_k^2}} \right]. \quad (1.5)$$

Ultimately, the variational condition leads to a self consistency equation

$$\Delta_k = -\frac{1}{2} \sum_{k'} U_{kk'} \frac{\Delta_{k'}}{\sqrt{\epsilon_{k'}^2 + \Delta_{k'}^2}} \quad (1.6)$$

Assuming that $U_{kk'} = -U_0/V$ for $|\epsilon_k|, |\epsilon_{k'}| < \hbar\omega_D$ and positive U_0 , it follows also that $\Delta_k = \Delta_0$ if $|\epsilon_k| < \hbar\omega_D$. V is the normalization volume the usual discrete sum can be replace with integration which lead to

$$1 = \frac{1}{2} U_0 n_0 \int_{-\hbar\omega_D}^{\hbar\omega_D} \frac{d\epsilon}{\sqrt{\epsilon^2 + \Delta_0^2}} \quad (1.7)$$

In the weak coupling limit, $U_0 n_0 \ll 1$, $\Delta_0 = 2\hbar\omega_D \exp(-1/U_0 n_0)$, n_0 is the density of states at the Fermi level. The difficulty of the BCS Hamiltonian comes from the product of four operators, therefore we would like to simplify it in line with mean field theory. We rewrite Cooper pair operators $Z_k = c_{-k\downarrow} c_{k\uparrow}$ as $Z_k = a_k + (Z_k - a_k)$, where $a_k = \langle Z_k \rangle$ is the average value of the fluctuation operator. In the mean field theory doctrine, neglecting presumably small fluctuations of second order, we end up with the mean field hamiltonian

$$\mathcal{H}_{\text{MF}} = \sum_{k\sigma} \epsilon_k c_{k\sigma}^\dagger c_{k\sigma} - \sum_k \left[\Delta_k c_{k\uparrow}^\dagger c_{-k\downarrow}^\dagger + \Delta_k^* c_{-k\downarrow} c_{k\uparrow} \right]. \quad (1.8)$$

Up until now we have been describing the ground state of superconductors, for a description of the excitations Bogoliobov proposed a canonical transformation of operators that diagonalizes the BCS hamiltonian [9]

$$\begin{pmatrix} \gamma_{k\uparrow} \\ \gamma_{-k\downarrow}^\dagger \end{pmatrix} = \begin{pmatrix} u_k & -v_k \\ v_k & u_k \end{pmatrix} \begin{pmatrix} c_{k\uparrow} \\ c_{-k\downarrow}^\dagger \end{pmatrix}, \quad \begin{pmatrix} \gamma_{k\uparrow}^\dagger \\ \gamma_{-k\downarrow} \end{pmatrix} = \begin{pmatrix} u_k & -v_k \\ v_k & u_k \end{pmatrix} \begin{pmatrix} c_{k\uparrow}^\dagger \\ c_{-k\downarrow} \end{pmatrix}, \quad (1.9)$$

in such a way the hamiltonian becomes

$$\mathcal{H}_B = \sum_k \omega_k [\gamma_{k\uparrow}^\dagger \gamma_{k\uparrow} + \gamma_{-k\downarrow}^\dagger \gamma_{-k\downarrow}] + W_S \quad (1.10)$$

with $\omega_k = \sqrt{\epsilon_k^2 + \Delta_k^2}$. The original mean field hamiltonian can be expressed as

$$\mathcal{H}_{\text{MF}} = \frac{1}{2} \begin{pmatrix} c^\dagger & c \end{pmatrix} \begin{pmatrix} h & \Delta \\ -\Delta^* & -h^T \end{pmatrix} \begin{pmatrix} c \\ c^\dagger \end{pmatrix}, \quad (1.11)$$

where (c^\dagger, c) is a vector of operators. The matrix elements have the following properties $h_{\alpha\beta} = h_{\beta,\alpha}^*$, $\Delta_{\alpha\beta} = -\Delta_{\beta\alpha}$. This form will be of great importance and convenience in next section where we discuss transport in superconducting heterostructures.

1.3. QUANTUM TRANSPORT

Quantum transport, both in normal and superconducting structures, can be conveniently described in terms of scattering formalism. In this section we are going to give a brief reminder of the method and apply it to a two terminal Josephson junction.

The number of types of nanostructures produced has expanded tremendously. There is huge variety of fabrication techniques that combine and shape different materials, such as superconductors, semi-conductors and metals, into a plethora of complicated heterostructures [16]. Although, by design all structures of a batch are made the same and fabrication precision has improved tremendously, no two are identical due to random disorder (impurities). Under the condition that there are no inelastic processes (low temperatures and low voltages), scattering approach allows one to simplify the problem by absorbing all the complexity of the scatterer into a small set of free parameters, all wrapped in a scattering matrix.

SCATTERING FORMALISM

A nanostructure is part of a controllable electric circuit, and as such is often connected via waveguides to macroscopic pads called reservoirs. They are the source of thermalized electrons at fixed voltage (chemical potential). Waveguides represent confined electrons in a tube, where the transverse motion is quantized while the longitudinal is that of a plane wave. They are also called quantum channels, where electron's motion is one dimensional. A scattering matrix S linearly relates the incoming $c_{\beta m}^{\text{inc}}$ to the outgoing $c_{\alpha n}^{\text{out}}$ wave amplitudes

$$c_{\alpha n}^{\text{out}} = \sum_{\beta m} S_{\alpha n, \beta m} c_{\beta m}^{\text{inc}}, \quad (1.12)$$

where α, β label different terminals and m, n label transport channels. The matrix can be easily understood with a simple picture where electrons enter from one terminal are either reflected back to the same reservoir (possibly changing the transport channel) $S_{\alpha\alpha}$ or are transmitted to any of the other terminals from terminal β to terminal α . The total number of particles being conserved in the system, it follows that S is unitary and the total probability sums to 1. If time-reversal symmetry is present the scattering matrix is symmetric $S^T = S$. For long nanostructures the scattering matrix is energy dependent while for short ones the energy dependence can be neglected.

LANDAUER FORMULA

Transport properties are described by a set of transmission eigenvalues derived from this scattering matrix. In a multi-terminal set-up, the current that flows in terminal α has two contributions, the first one being the particles that are originating from the terminal itself and are reflected back which are distributed according Fermi-Dirac distribution at zero temperature $f_\alpha(E)$ and the second one being the particles that are transmitted through the scattering region coming from all the rest β channels, with distribution $f_\beta(E)$. The current in terminal α is thus

$$I_\alpha = 2se \int \frac{dE}{2\pi} P_{\alpha\beta}(E) (f_\beta(E) - f_\alpha(E)). \quad (1.13)$$

with $P_{\alpha\beta}$ being the probability to transition from terminal α to terminal β . This is Landauer formula in scattering formalism [24]. Assuming energy independent transmission

$P_{\alpha\beta}(E) = P_{\alpha\beta}$ and small applied voltages, the current simplifies to

$$I_\alpha = 2s e \sum_\beta P_{\alpha\beta} e(V_\beta - V_\alpha) = G_Q P_{\alpha\beta} (V_\beta - V_\alpha) \quad (1.14)$$

where $2s$ incorporates spin and the conductance quantum is $G_Q = e^2/\pi$. Due to the unitarity of the scattering matrix S , the current of all terminals sums up to zero.

ANDREEV BOUND STATES

In the next subsection, we are going to look at the formation of a discrete level called Andreev Bound State in a short nanostructure sandwiched between two superconducting terminals with the same gap parameter Δ but different superconducting phases ϕ_L and ϕ_R . As we have already discussed short junctions are described by energy-independent scattering matrices, thus it is irrelevant whether the middle structure is a metal or an insulator as scattering is described with a scattering matrix in the normal state. Let us consider the scattering processes for a single channel in the normal region. The amplitudes of the incoming and the outgoing waves are related via:

$$\begin{pmatrix} c_e^{out} \\ c_h^{out} \end{pmatrix} = \begin{pmatrix} s & 0 \\ 0 & s^* \end{pmatrix} \begin{pmatrix} c_e^{inc} \\ c_h^{inc} \end{pmatrix}, \quad (1.15)$$

where the two components of the amplitude vectors correspond to the left and right side of the nanostructure, respectively. The nanostructure does not convert holes into electrons and vice versa, that is why it is block-diagonal. In more details the amplitudes of ingoing/outgoing hole/electron has additional structure corresponding to left and right lead

$$c_e^{out} = \begin{pmatrix} c_{Le}^{out} \\ c_{Re}^{out} \end{pmatrix} \quad c_h^{out} = \begin{pmatrix} c_{Lh}^{out} \\ c_{Rh}^{out} \end{pmatrix} \quad c_e^{inc} = \begin{pmatrix} c_{Le}^{inc} \\ c_{Re}^{inc} \end{pmatrix} \quad c_h^{inc} = \begin{pmatrix} c_{Lh}^{inc} \\ c_{Rh}^{inc} \end{pmatrix}. \quad (1.16)$$

In order to describe what happens at the interface between the nanostructure and the superconductor one needs a more involved treatment, because the scattering matrix between normal and superconducting interface is energy-dependent. From the previous section (give reference to formula) we know that the excitations have the corresponding energy

$$E = \sqrt{\epsilon^2 + \Delta^2} \quad \epsilon = \hbar v_F (k - k_F) \quad (1.17)$$

, where the spectrum has been linearized close to the Fermi surface. For energies above the gap $E > \Delta$, quasiparticles propagate freely in the form of plane waves, while for energies below the gap $E < \Delta$ quasiparticles decay exponentially away from the interface with the form of an evanescent wave function. In the normal part of the structure, electrons and holes are decoupled. Whenever an electron in the sub-gap mode tries to enter the superconductor, it will be reflected as a hole and acquires a phase shift r_A

$$r_A = e^\chi = e^{-i\phi} \left(\frac{E}{\Delta} - i \frac{\sqrt{\Delta^2 - E^2}}{\Delta} \right). \quad (1.18)$$

Electrons in the gap are Andreev reflected [4] back as holes at one interface and the holes are then reflected back as electrons on the other interface. Those consecutive processes do not allow electrons and holes to escape the nanostructure and lead to a finite motion,

thus giving rise to a bound state of quasiparticles, called Andreev Bound States. Andreev reflection leads to complementary relation between incoming and outgoing waves

$$\begin{pmatrix} c_e^{inc} \\ c_h^{inc} \end{pmatrix} = \begin{pmatrix} 0 & s_{eh} \\ s_{he} & 0 \end{pmatrix} \begin{pmatrix} c_e^{out} \\ c_h^{out} \end{pmatrix} \quad (1.19)$$

with

$$s_{eh} = \begin{pmatrix} e^{i\chi_L^+} & 0 \\ 0 & e^{i\chi_R^+} \end{pmatrix}, \quad s_{he} = \begin{pmatrix} e^{i\chi_L^-} & 0 \\ 0 & e^{i\chi_R^-} \end{pmatrix}, \quad (1.20)$$

where $\chi_{L,R}^\pm = \pm\phi_{L,R} - \arccos(E/\Delta)$ and $\phi_{L,R}$ being the left and right superconducting phases. Combining Eq.1.15 and Eq.1.19, we obtain the energy of the bound state

$$E = \Delta \sqrt{1 - T \sin^2(\phi/2)} \quad (1.21)$$

with ϕ being the phase difference and T the transmission.

JOSEPHSON JUNCTION

Often Josephson junctions host multiple channels thus the energy will be the sum over every channel $E(\phi) = -\sum_p E_p(\phi) = \Delta \sum_p \sqrt{1 - T_p \sin^2(\phi/2)}$. The power dissipated is proportional to the product of current times the voltage but can also be evaluated as $dE/dt = \frac{\partial E}{\partial \phi} \frac{d\phi}{dt}$ and knowing that the phase derivative is $\dot{\phi} = 2eV/\hbar$, we deduce that the current in the junction is given by

$$I(\phi) = -\frac{2e}{\hbar} \sum_p \frac{\partial E_p}{\partial \phi} = \frac{e\Delta}{2\hbar} \sum_p \frac{T_p \sin(\phi)}{\sqrt{1 - T_p \sin^2(\phi/2)}}. \quad (1.22)$$

Until now we have considered a simplified case where the scattering matrix is energy-independent and the microscopic details of the scattering matrix have not been fully illustrated. In Chapters 2 and 3, we discuss a microscopic way of determining the reflection and transmission coefficients in a more complicated structure by finding the explicit wave functions in each region and performing wave-matching on the different interfaces.

Furthermore, all designs and concrete configurations are encoded in the transmission eigenvalues distributions. If transmission or equivalently the scattering matrix depends on energy, then the total energy is not only the sum of Andreev state energies but has additional contribution from the continuous spectrum in the leads and has to be computed most thoroughly which we have done in Chapter 4.

1.4. TOPOLOGY

In this section we discuss a simple illustrative model Hamiltonian and relate it to a newly proposed system for non-trivial topological realizations. In the last decade, topological concepts have played a prominent role in the development and deeper understanding of condensed matter physics [25].

The field gave rise to a plethora of examples of realizations of otherwise abstract topological concepts such as topological insulators and topological superconductors [26] and topological

semi-metals [36, 5]. The interest towards topological matter originates from the feature of topological protection. Topologically protected quantities are robust under external non-symmetry-breaking perturbations of the system. As an example, topological insulators are characterized with nonconducting bulk but with conducting edges on the surface where the bands cross. Those edge states are also protected against localization [20].

The pinnacle of this research axis was the classification of gapped topological phases (characteristic classes) which allowed to put every material in a class according to three characteristics: (i) the symmetry: time-reversal, superconducting, inversion (ii) the dimension of the parameter space (base space) and (iii) the dimension of the vector bundle [21].

WEYL HAMILTONIAN

We turn our attention to the illustrative example of the Weyl Hamiltonian[32] that has special properties of the spectrum [18]. It hosts a topologically protected point-like band crossings, present in a 3d parameter space. Crossings can occur in any three dimensional parametric space and such a situation arises in the 3d 2π - periodic band structures of crystalline solids. Such solids have been named Weyl semimetals and were experimentally realized in tantalum arsenide (TaAs)[34].

The most generic two band crossing in 3d with linear dispersion without any symmetry can be modelled with the following Hamiltonian that is valid in the vicinity of a singularity point at \vec{d}_0

$$\mathcal{H}_{\text{Weyl}} = \vec{d} \cdot \vec{\sigma}, \quad (1.23)$$

where \vec{d} are linear deviations from the singularity point and $\vec{\sigma}$ is a vector of Pauli matrices in the space of the two crossing bands. It is important to note that the matrix is not only Hermitian but it is also proportional to an unitary matrix $\mathcal{H}^2 = |d|^2 I$, resulting into the eigenvalues $E_{\pm} = \pm|d|$. Topological protection is usually characterized by a topological invariant that labels different configurations. One usually defines a parameter space gauge potential, called the Berry connection [30]

$$\vec{A}_n = i \langle n | \nabla_{\vec{d}} | n \rangle, \quad (1.24)$$

where $|n\rangle$ is the wavefunction of the n 'th band. Here we restrict the discussion to the Abelian case, where there is no band degeneracy except at the singularity point. The non-Abelian case of the connection is considered in [33] and the outstanding illustration of the relations between Abelian, non-Abelian, first and second Chern numbers, Weyl and Yong monopoles is provided in [14]. There is also an Abelian gauge field associated with this gauge potential that is known as the Berry curvature [30]

$$\vec{B}_n(\vec{d}) = \nabla_{\vec{d}} \times \vec{A}_n. \quad (1.25)$$

In the vicinity of a Weyl point the Berry curvature emulates the magnetic field generated by a magnetic monopole $\vec{B}_n(\vec{d}) = \pm \frac{1}{2} \frac{\vec{d}}{d^3}$. Thus Weyl points can be viewed as the sources or drains for the Berry curvature. We can characterize the Weyl singularity with a topological index called the first Chern number

$$N_1 = \oint_S \vec{B}_n(\vec{d}) \cdot d\vec{S}, \quad (1.26)$$

where S is a closed surface enclosing the singularity. N_1 can be $+1$ or -1 depending on the chirality of the charge (each one corresponding to the two bands). For the crossing of two bands these charges are opposite.

Another perspective on the subjects is as follows: outside of the degeneracy $\vec{d} \neq \vec{0}$, one can restrict the Hamiltonian to a 2d smooth subspace of the 3d parameter space, where the Hamiltonian is gapped. Consequently, one obtains locally well-defined functions that may have nontrivial Chern number. Thus, this gapless phase can be described as the transition between two gapped phases—two families of hamiltonians that are topologically different. In the next subsection we are going to apply those concepts to a newly proposed system for topological realizations, namely to a multi-terminal superconducting nanostructure.

TOPOLOGY IN SUPERCONDUCTING HETEROSTRUCTURES

The essential characterization of topological materials starts with the properties of the band structure. Multiterminal superconducting heterostructures have 2π periodic parameters, which are the number of independent phase differences. In an n terminal case, there are $n - 1$ controllable and independent phase differences. The equivalency between the BZ in solids and superconducting phase differences leads to the possibility to simulate band structures with the aid of multi-terminal heterostructures, with the Andreev states being the discrete levels equivalent of bands.

The advantage of this system is that the dimensionality is only fixed by the number of terminals, while in solids it is 3 or less. On top, topological materials are notoriously difficult to synthesize chemically while heterostructures do not require any topological components. Thus there are two ways to realize topological materials. First by experimentally manufacturing compounds [11, 35] where topological properties emerge due to a nontrivial bandstructure or, second make nanostructures, where the interplay between different materials gives rise to topological properties [27]. The latter opens up the possibility to simulate gapless and gapped topological materials of superconducting classes (C and D [21, 2]) with multi-terminal heterostructures.

In Ref.[27], the authors present an example of a 4 terminal structure that hosts Weyl singularities. Four superconducting terminals are connected to a short normal scattering region, described by an energy independent scattering matrix, containing scattering matrices for electrons s_e and holes s_h . Andreev bound states are obtained from $\det(e^{2i\chi} - A) = 0$, with $\chi = \arccos(E/\Delta)$ and $A = s_e^* e^{i\phi} s_e e^{-i\phi}$, with $e^{-i\phi}$ being the matrix of phases for the terminals. Two levels can cross at zero energy at a given ϕ_0 , corresponding to an eigenvalue -1 of A . Near the crossing, one can write an effective low-energy Hamiltonian Eq. 1.23 that is linearly proportional to the deviations from the singularity. The topological charge of the singularity is conveniently evaluated from $\text{sign}(\det(h_j^i))$, with the matrix elements given by

$$h_x^i = \frac{i}{2} (\langle \Psi_0^+ | V_i | \Psi_0^- \rangle + \langle \Psi_0^- | V_i | \Psi_0^+ \rangle) \quad (1.27)$$

$$h_y^i = \frac{1}{2} (\langle \Psi_0^+ | V_i | \Psi_0^- \rangle - \langle \Psi_0^- | V_i | \Psi_0^+ \rangle) \quad (1.28)$$

$$h_z^i = \frac{i}{2} (\langle \Psi_0^+ | V_i | \Psi_0^+ \rangle - \langle \Psi_0^- | V_i | \Psi_0^- \rangle), \quad (1.29)$$

where Ψ_0^\pm correspond to the wavefunctions of the levels and the anti-Hermitian operator $V_i = \partial_{\phi_i} A(\phi)$. The control over the phases allows to move a surface in parameter space of phases, whenever the phases cross the singularity, the Chern number jumps and this is observed in the average current

$$I_\alpha = G^{\alpha\beta} V_\beta \quad \text{with} \quad G_{\alpha\beta} = \frac{-2e^2}{\pi\hbar} C^{\alpha\beta}. \quad (1.30)$$

1.5. RANDOM MATRIX THEORY

A convenient description of chaotic and disordered systems can be achieved using Random Matrix Theory (RMT). As the name suggests, the theory deals with matrices whose entries are randomly distributed variables. The limit of interest is that of large matrix dimension $N \gg 1$. In quantum transport, two types of matrices are of significance. The first type is a Hermitian matrix which may represent a physical Hamiltonian, the matrix eigenvalues corresponding to energy levels. The second type is a unitary matrix that may represent a scattering matrix of a nanostructure.

Let us start with Hermitian matrices, for which it is natural to assume that the elements are independently distributed random variables with the same variance. The statistics are usually considered for matrices of certain symmetry ensemble. The ensemble are labelled with integer β . The matrix is diagonalizable by a unitary transformation U of a certain class, depending on the symmetry of the matrix: (i) if time-reversal and spin-rotation symmetries are present, then the matrix is real and U is orthogonal ($\beta = 1$), (ii) if time-reversibility is absent, then the matrix is general Hermitian and U is unitary ($\beta = 2$), (iii) if time-reversibility is present but spin-rotation is absent then the matrix is a real quaternion and U is symplectic ($\beta = 4$). The ensembles are named after the unitary transformations accordingly: (i) Gaussian Orthogonal Ensemble GOE, (ii) Gaussian Unitary Ensemble GUE, (iii) Gaussian Symplectic Ensemble GSE.

The probability density of a matrix H is given by

$$P(H) \propto \exp\left(-\frac{\beta}{2\lambda^2} \text{tr} H^2\right), \quad (1.31)$$

where λ^2 is the variance of a matrix element. The average density of eigenvalues $\langle \nu(E) \rangle = \langle \sum_n \delta(E_n - E) \rangle$ in the limit of $N \gg 1$ reads:

$$\langle \nu(E) \rangle = \frac{\sqrt{N}}{\pi\lambda} \sqrt{1 - \left(\frac{E}{2\sqrt{N}\lambda}\right)^2} \quad (1.32)$$

provided $|E| < 2\sqrt{N}\lambda$ and is zero otherwise. The eigenvalues are thus concentrated within an interval $|E| < 2\sqrt{N}\lambda$. It is convenient to concentrate on the range of eigenvalues close to the centre of this band $E \ll 2\sqrt{N}\lambda$ where the average density of eigenvalues is approximately constant. The mean level spacing at the centre of the band is thus $\delta_s = \pi\lambda/\sqrt{N}$.

The most spectacular result of RMT is the joint distribution of eigenvalues $P(\{E_n\})$ [23]

$$P(\{E_n\}) \propto \exp\left(-\beta N \sum_n \left(\frac{E_n}{\lambda}\right)^2 + \frac{\beta}{2} \sum_{m>n} \ln\left(\frac{E_m - E_n}{\lambda}\right)^2\right). \quad (1.33)$$

We do not give the derivation here but instead provide short description of it. One needs to transform the distribution of matrix elements $P(H)$ to the distribution of eigenvalues and eigenvectors $P(\{E_n\}, \{v_n\})$. The transformation from $P(H)$ to $P(\{E_n\}, \{v_n\})$ is associated with a Jacobian, and after integrating out the eigenvectors distribution one finds that the Jacobian depends only on the eigenvalues $J(E_n) = \prod_{i<j} |E_i - E_j|^\beta$, and in this sense the repulsion of the eigenvalues is seen as a geometrical.

We come back now to the physical analogy of Eq. 1.33, where we can identify $\{E_n\}$ as the positions of classical charges in one dimension. These charges repel each other according to logarithmic law (like Coulomb interaction in two dimensions) and are constrained by a quadratic potential. This is called a Coulomb gas. The index β plays the role of inverse temperature: the higher the temperature, the easier it is for the charges to overcome the level repulsion. In the limit of $\beta \rightarrow \infty$ the spectrum is completely ordered, the charges are separated by the same spacing, that is a slow function of energy. Finite β permit fluctuations yet the spectrum possess a property called rigidity: the variance of number of levels in a wide interval does not depend on the number of levels in the interval and is of the order of $1/\beta$.

Whenever there is an external applied perturbation to the system $H(x) = H_0 + XH_1$, eigenenergies wiggle in parametric space and this phenomena can be quantified with random level-uncorrelated velocities $v_i = \partial_X E_i(X)$. The variance of velocity of the same level is $v^2 = \langle (\partial_X E_i(X))^2 \rangle$ and does not depend on the level. The levels propagate with these random velocities along X till they began to feel each other repulsion. This will happen when the change of the distance between the levels becomes of the order of the mean level spacing δ_s . This sets a scale in the parametric space $x_c = \delta_s/v$ that defines correlation length of these fluctuations. An important result of RMT is that the statistics of level positions and their velocities are universal [29] after rescaling.

FOKKER-PLANCK EQUATION

We describe the level motion under external perturbation X following the particles analogy we can look at parametric statistics of system of electric charges representing the eigenvalues, with a parabolic confining potential, logarithmic repulsion, and the effective temperature β^{-1} . We introduce the fictitious time τ and look at the evolution of the positions of all charges. The fictitious time is related to the perturbation parameter as $\tau = X^2$ [8].

Since they are at finite temperature, they now perform random Brownian motion. The joint distribution function of the positions of all the charges (the distribution function of all eigenvalues), $P(\{E_n\}, \tau)$, obeys the Fokker–Planck equation:

$$\frac{\partial}{\partial \tau} P = \sum_i \frac{\partial}{\partial E_i} \frac{\beta v^2}{2} \left(P \frac{\partial W}{\partial E_i} + \beta^{-1} \frac{\partial P}{\partial E_i} \right), \quad (1.34)$$

where the potential is $W = -\sum_{i < j} \log(E_i - E_j) + \sum_i E_i$. On the right-hand side, the first term (second derivative) represents “diffusion,” whereas the other two are responsible for the “drift” in the effective potential – external parabolic confinement and logarithmic interaction potential created by all eigenvalues.

Due to the logarithmic repulsion, the eigenvalues cannot come close to each other; then we have a situation of avoided crossing. Thus the levels never cross in one dimension. As we will see the situation is different in three-dimensional parameter space considered in Chapter 5.

SUPERCONDUCTING CLASSES

We conclude this section with the discussion of superconducting matrix classes. As we have already discussed the symmetries of the Hamiltonians strongly indicate the way the distribution of eigenvalues will be determined. The interest of this thesis lies in superconducting heterostructures, we present the classes of random matrices that are of interest. Hamiltonians which are BdG symmetric have mirrored spectrum $H = \text{diag}(\omega, -\omega)$, $\omega = (\omega_1, \dots, \omega_N)$. The distribution is given by:

$$P(\{\omega\}) = \prod_{i < j} |\omega_i^2 - \omega_j^2|^\beta \prod_k |\omega_k|^\alpha e^{-\omega_k^2/v^2}. \quad (1.35)$$

We observe that there are two coefficients α and β . We do not discuss the details but only mention that there is the possibility of repulsion not only between different eigenvalues but there is also repulsion from the zeroth eigenvalue. For more information, please see [2].

SCATTERING MATRICES

If we would like to describe transport properties, we need to deal with scattering matrices. As we already mentioned, scattering matrices are unitary and they can belong to the following classes: (i) they are either symmetric (circular orthogonal), not symmetric (circular unitary) or quaternionic (circular symplectic). We assume that these random matrices are distributed uniformly: the probability of finding a matrix is always the same. These ensembles are similar to the corresponding Gaussian ensembles GOE, GUE, and GSE; in particular, they are characterized by the same “inverse temperature” $\beta = 1, 2, 4$.

The same repulsion occurs for unitary matrix of a greater size $2N \times 2N$ which has eigenvalues $\exp(i\phi_1), \dots, \exp(i\phi_{2N})$. The joint distribution function of these eigenvalues has the form, up to a normalizing constant factor, given by

$$P(\{\phi_n\}) \propto \prod_{n < m} |\exp(i\phi_n) - \exp(i\phi_m)|^\beta \quad (1.36)$$

with the phase shifts $\{\phi_n\}$ being real numbers. Similarly to Gaussian ensembles, the expression has an interpretation in terms of classical charges on a ring of unit radius. Their positions are characterized by the polar angles ϕ_m . These charges repel logarithmically the effective temperature is β^{-1} .

A member of this circular ensemble eventually gives the scattering matrix of a quantum chaotic cavity [8] where electrons are transmitted ballistically. We connect the cavity to two leads. If there are N_1 channels going to the right lead and N_2 channels going to the left lead the total dimension of the scattering matrix is $N_1 + N_2$. One can obtain the distribution for a set of transmission eigenvalues T_n – the eigenvalues of the matrix $t^\dagger t$, where t is a transmission block of the scattering matrix with size $N_1 \times N_2$:

$$P(\{T_n\}) = \prod_{i < j} |T_i - T_j|^\beta \prod_k T_k^{-1 + \beta/2 + (\beta/2)|N_1 - N_2|}. \quad (1.37)$$

One can make analogy of with the distribution of eigenvalues given by Eq. 1.33. The first product corresponds to the repulsion of all the eigenvalues while the second product corresponds to a confinement potential that restricts the transmissions to the interval $[0, 1]$.

However such a quantum cavity is only a single design of a variety of possible nanostructure designs that can involve ballistic, diffusive and tunnelling transmissions. The description of a given design can be achieved by combining RMT with Quantum Circuit Theory (QCT) in the next section.

1.6. QUANTUM CIRCUIT THEORY

The theoretical predictions of weak localization [1] and universal conductance fluctuations [3] along with experimental discoveries in this direction [31] have laid a basis of modern understanding of quantum transport and have stimulated a considerable interest to the topic. The quantum conductance $G_Q = e^2/\pi$ is the universal value that sets an important division between classical conductors ($G \gg G_Q$) where interference effects are small and quantum ones ($G \simeq G_Q$) where the transport is essentially quantum. One can describe nanostructures in the framework of a simple finite-element approach usually termed "circuit theory". Quantum circuit theory is a semi-classical method, this means that it is assumed that the conductance of the structure is much bigger than the quantum conductance $1 \ll G/G_Q \propto N_{ch}$.

In this framework, a nanostructure is subdivided into connectors and nodes. This is similar to the finite element presentation of a classical conducting medium. There the structure is subdivided into nodes where voltage is constant and connectors where voltage drops. There are terminals with fixed voltage connected to the structure. Kirchoff laws are equivalent to current conservation in the nodes and determine voltages in every node and currents in each connector in terms of the terminal voltages.

Quantum circuit theory has a similar structure. Matrix voltage G is introduced in every node and terminal. The matrix G is related to electron Green's functions and satisfies $G^2 = 1$ and $\text{Tr}(G) = 0$. In distinction from classical circuits, connectors can be of very different types: tunnel junction, ballistic contact and diffusive wire and are generally characterized by a set of transmission coefficients T_p . To make connection to RMT described in the previous section, each node can be presented as random unitary matrix of a respective ensemble and each connector can be presented as a block diagonal scattering matrix, where blocks correspond to quantum channels with transmission coefficients T_p .

Like in classical circuits, one is generally interested in the matrix voltage in the nodes as a function of the matrix voltages in the reservoirs. The goal is to find the corresponding matrix currents flowing in each connector as function of the fixed matrix voltages in the

terminals. For that the equivalent of Kirchoffs law can be applied $\sum I = 0$, where the sum is over all connectors. This translates to conservation of matrix currents in each node. The matrix current will be expressed via two matrix voltages at the end of a connector $I = F(G_1, G_2)$ (see Eq. 1.40). The voltages at the nodes are determined from the current conservation in each node and they determine the currents to and from the terminals.

One can formulate a variational principle introducing an action for the whole circuit, that depends on matrix voltages in all nodes and reservoirs. The actual G in the nodes are obtained from the minimization of this action. and which can be represented by the sum of all connectors

$$S = \sum_c S_c(G_{c1}, G_{c2}), \quad (1.38)$$

where the summation is over connectors and c_1, c_2 denote the ends of a connector which can be a node or a terminal. The equations for actual matrix voltages of the nodes are obtained from the condition that this action has a minimum $\delta S = 0$ with respect to variations of G in the nodes. This sum also includes the connectors representing leakage currents. Leakage currents describe the effect of the finite volume of the nodes and are of significance for long nanostructures. They cannot be modelled by real parts in the nanostructures but are rather due to fictitious reservoirs and fictitious nodes and connectors which lead to loss of coherence. However, the practical advantage is overwhelming, since currents from the fictitious terminals enter the current balance in precisely the same fashion as from the real ones and can be treated in the same manner. See [24]

A connector positioned between the terminals/nodes i, j can be described with an action $S_{i,j}$ that is a function of G_i and G_j

$$S_c = \frac{1}{2} \sum_p \text{Tr} \left(\log \left(1 + \frac{T_p}{4} (G_1 G_2 + G_2 G_1 - 2) \right) \right), \quad (1.39)$$

where T_p is the transmission eigenvalue of that connector. The current through a connector c which connects nodes c_1 and c_2

$$I_c = G_Q \sum_p \frac{T_p (G_1 G_2 - G_2 G_1)}{2 + (T_p/2)(G_1 G_2 + G_2 G_1 + 2)}. \quad (1.40)$$

Various choices of matrices G give various quantum circuit theories [24]. In a theory describing superconducting heterostructure, terminals and nodes are represented with energy dependent Green's functions $G_i(\epsilon)$ that are 2×2 matrices in Nambu space. In imaginary time technique these matrices can be represented with real unit vectors. In the superconducting leads these vectors are $g_i = (\epsilon, \Delta \sin(\phi), \Delta \cos(\phi)) / \sqrt{\epsilon^2 + \Delta^2}$, where Δ is the superconducting gap and ϕ is the corresponding superconducting phase.

The action for each connector can also be written as a function of a parameter ϕ , which is the angle between two vectors at the ends of the connector that is $\arccos(g_i \cdot g_j)$. The actions for some simple type of connectors are:

$$S = -\frac{G_T}{2} \sin^2(\phi/2) \quad (1.41)$$

for tunnelling junction,

$$S = \frac{G_D}{8} \phi^2, \quad (1.42)$$

for diffusive junction and

$$S = -G_B \ln \cos(\phi/2), \quad (1.43)$$

for ballistic junction, where G_B, G_D, G_T are conductances in units of G_Q . The quantum circuit theory we have outlined so far is valid in the limit $G \gg G_Q$.

For a common conductor this corresponds to a classical Ohm's law expression. The quantum effects are manifested as G_Q corrections: weak-localization and universal conductance fluctuations [1, 3] that are deviations of the order of $G_Q \ll G$. It turns out that the quantum circuit theory can be used to compute G_Q corrections as well. This is described in [10] which treats G_Q corrections to multi-component Green's functions of arbitrary matrix structure. The action describing G_Q corrections takes a form of a log of determinant of a matrix. This matrix is made from the response functions: the derivatives of matrix voltages in the nodes with respect to matrix self-energy parts also defined in the nodes. The determinant is just that of a finite matrix, this facilitates the computation of G_Q corrections for nanostructures of arbitrary design.

We use this G_Q correction extension in Chapter 5, where we quantify the universal parametric correlations in the space of the superconducting phases characterising the terminals in a multi-terminal superconducting nanostructure. To describe the parametric correlations between two points B and W in this space, the Green's functions will be of a double dimension corresponding to these two points G_B and G_W . The relevant response functions correspond to non-diagonal entries $\delta G_{BW} \propto G_B G_W$. One computes the G_Q correction action \mathcal{S}_{G_Q} that depends on parameter sets W and B . The quantities of interest are obtained by differentiating this action with respect to the parameters in the limit $B \rightarrow W$.

1.7. STRUCTURE OF THIS THESIS

CHAPTER 2

In this Chapter, we evaluate the energy splitting of degenerate Andreev bound states, that overlap in a superconducting lead, and find that the splitting is reduced in comparison with their energy by a small factor $\sqrt{RG_Q}$, RG_Q being the dimensionless resistance of the overlap region in the normal state. This permits quantum manipulation of the quasiparticles in these states. We provide a simple scheme of such manipulation. This analysis was inspired by the recent proposals of experiments with single Andreev bound states that make relevant a detailed analysis of these states in multi-terminal superconducting nanostructures.

CHAPTER 3

In this Chapter, we study the Andreev Bound State (ABS) in a device consisting of a semiconducting nanowire covered with three superconducting leads. The ABS are formed at two junctions where the wire is not covered. They overlap in the wire where the electron propagation is 1D, and in one of the leads where the propagation is 3D. We identify a number of regimes where these two overlaps either dominate or compete, depending on the junction separation L as compared to the correlation lengths ξ_w , ξ_s in the wire and in the lead, respectively. We utilize a simple model of 1D electron spectrum in the nanowire and

take into account the quality of the contact between the nanowire and the superconducting lead.

CHAPTER 4

In this Chapter, we formulate and investigate a model of a superconducting junction that combines the electron propagation in a quantum channel with an arbitrary transmission, and that through a localized state. Interesting situation occurs if the energy of the localized state is close to Fermi level, that is, the state is in resonant tunnelling regime. Since this energy is affected by the gate voltage, we expect a drastic modification of transport properties of the junction in a narrow interval of the gate voltages where the energy distance to Fermi level is of the order of Γ, Δ , Γ being the energy broadening of the localized state, Δ being the superconducting energy gap.

We consider the model neglecting the interaction in the localized state, as well as accounting for the interaction in a simplistic mean-field approach where it manifests itself as a spin-splitting. This spin splitting is also contributed by external magnetic field. We also take into account the spin-orbit interaction that can be significant in realistic experimental circumstances.

CHAPTER 5

In this Chapter, we show that the quasi-continuous gapless spectrum of Andreev bound states in multi-terminal semi-classical superconducting nanostructures exhibits a big number of topological singularities. We concentrate on Weyl points in a 4-terminal nanostructure, compute their density and correlations in 3D parameter space for a universal RMT model as well as for the concrete nanostructures described by the quantum circuit theory. We mention the opportunities for experimental observation of the effect in a quasi-continuous spectrum.

BIBLIOGRAPHY

- [1] E. Abrahams et al. “Scaling Theory of Localization: Absence of Quantum Diffusion in Two Dimensions”. In: *Phys. Rev. Lett.* 42.10 (Mar. 1979), pp. 673–676. ISSN: 1079-7114. DOI: [10.1103/PhysRevLett.42.673](https://doi.org/10.1103/PhysRevLett.42.673).
- [2] Alexander Altland and Martin R. Zirnbauer. “Nonstandard symmetry classes in mesoscopic normal-superconducting hybrid structures”. In: *Phys. Rev. B* 55.2 (Jan. 1997), pp. 1142–1161. ISSN: 2469-9969. DOI: [10.1103/PhysRevB.55.1142](https://doi.org/10.1103/PhysRevB.55.1142).
- [3] B. L. Altshuler. “Fluctuations in the extrinsic conductivity of disordered conductors”. In: *JETP Lett.* 41.12 (June 1985), pp. 530–533.
- [4] A. F. Andreev. “The Thermal Conductivity of the Intermediate State in Superconductors”. In: *Soviet Physics-JETP* 19 (Nov. 1964), pp. 1228–1232.
- [5] N. P. Armitage, E. J. Mele, and Ashvin Vishwanath. “Weyl and Dirac semimetals in three-dimensional solids”. In: *Rev. Mod. Phys.* 90.1 (Jan. 2018), p. 015001. ISSN: 1539-0756. DOI: [10.1103/RevModPhys.90.015001](https://doi.org/10.1103/RevModPhys.90.015001).
- [6] J. Bardeen, L. N. Cooper, and J. R. Schrieffer. “Microscopic Theory of Superconductivity”. In: *Phys. Rev.* 106.1 (Apr. 1957), pp. 162–164. ISSN: 1536-6065. DOI: [10.1103/PhysRev.106.162](https://doi.org/10.1103/PhysRev.106.162).
- [7] J. Bardeen, L. N. Cooper, and J. R. Schrieffer. “Theory of Superconductivity”. In: *Phys. Rev.* 108.5 (Dec. 1957), pp. 1175–1204. ISSN: 1536-6065. DOI: [10.1103/PhysRev.108.1175](https://doi.org/10.1103/PhysRev.108.1175).
- [8] C. W. J. Beenakker. “Random-matrix theory of quantum transport”. In: *Rev. Mod. Phys.* 69.3 (July 1997), pp. 731–808. ISSN: 1539-0756. DOI: [10.1103/RevModPhys.69.731](https://doi.org/10.1103/RevModPhys.69.731).
- [9] N. N. Bogoljubov. “On a new method in the theory of superconductivity”. In: *Nuovo Cim.* 7.6 (Mar. 1958), pp. 794–805. ISSN: 1827-6121. DOI: [10.1007/BF02745585](https://doi.org/10.1007/BF02745585).
- [10] G. Campagnano and Yu. V. Nazarov. “ G_Q corrections in the circuit theory of quantum transport”. In: *Phys. Rev. B* 74.12 (Sept. 2006), p. 125307. ISSN: 2469-9969. DOI: [10.1103/PhysRevB.74.125307](https://doi.org/10.1103/PhysRevB.74.125307).
- [11] Y. L. Chen et al. “Experimental Realization of a Three-Dimensional Topological Insulator, Bi₂Te₃”. In: *Science* (July 2009). URL: https://www.science.org/doi/10.1126/science.1173034?url_ver=Z39.88-2003%ED%94%AF_id=ori:rid:crossref.org%ED%94%AF_dat=cr_pub%20%200pubmed.
- [12] Leon N. Cooper. “Bound Electron Pairs in a Degenerate Fermi Gas”. In: *Phys. Rev.* 104.4 (Nov. 1956), pp. 1189–1190. ISSN: 1536-6065. DOI: [10.1103/PhysRev.104.1189](https://doi.org/10.1103/PhysRev.104.1189).

- [13] Dirk van Delft and Peter Kes. “The discovery of superconductivity”. In: *Phys. Today* 63.9 (Sept. 2010), p. 38. ISSN: 0031-9228. DOI: [10.1063/1.3490499](https://doi.org/10.1063/1.3490499).
- [14] Eugene Demler and Shou-Cheng Zhang. “Non-Abelian Holonomy of BCS and SDW Quasiparticles”. In: *Ann. Phys.* 271.1 (Jan. 1999), pp. 83–119. ISSN: 0003-4916. DOI: [10.1006/aphy.1998.5866](https://doi.org/10.1006/aphy.1998.5866).
- [15] R. M. Fernandes, A. V. Chubukov, and J. Schmalian. “What drives nematic order in iron-based superconductors? - Nature Physics”. In: *Nat. Phys.* 10 (Feb. 2014), pp. 97–104. ISSN: 1745-2481. DOI: [10.1038/nphys2877](https://doi.org/10.1038/nphys2877).
- [16] Byron D. Gates et al. “New Approaches to Nanofabrication: Molding, Printing, and Other Techniques”. In: *Chem. Rev.* 105.4 (Apr. 2005), pp. 1171–1196. ISSN: 0009-2665. DOI: [10.1021/cr030076o](https://doi.org/10.1021/cr030076o).
- [17] Giuseppe Grosso and Giuseppe Pastori Parravicini. *Solid State Physics*. Elsevier, Academic Press, 2014. ISBN: 978-0-12-385030-0. DOI: [10.1016/C2010-0-66724-1](https://doi.org/10.1016/C2010-0-66724-1).
- [18] Shuang Jia, Su-Yang Xu, and M. Zahid Hasan. “Weyl semimetals, Fermi arcs and chiral anomalies - Nature Materials”. In: *Nat. Mater.* 15 (Nov. 2016), pp. 1140–1144. ISSN: 1476-4660. DOI: [10.1038/nmat4787](https://doi.org/10.1038/nmat4787).
- [19] B. D. Josephson. “Possible new effects in superconductive tunnelling”. In: *Physics Letters* 1.7 (July 1962), pp. 251–253. ISSN: 0031-9163. DOI: [10.1016/0031-9163\(62\)91369-0](https://doi.org/10.1016/0031-9163(62)91369-0).
- [20] C. L. Kane and E. J. Mele. “ Z_2 Topological Order and the Quantum Spin Hall Effect”. In: *Phys. Rev. Lett.* 95.14 (Sept. 2005), p. 146802. ISSN: 1079-7114. DOI: [10.1103/PhysRevLett.95.146802](https://doi.org/10.1103/PhysRevLett.95.146802).
- [21] Alexei Kitaev. “Periodic table for topological insulators and superconductors”. In: *AIP Conf. Proc.* 1134.1 (May 2009), pp. 22–30. ISSN: 0094-243X. DOI: [10.1063/1.3149495](https://doi.org/10.1063/1.3149495).
- [22] Charles Kittel. *Introduction to Solid State Physics, 8th Edition*. Hoboken, NJ, USA: Wiley, Nov. 2004. ISBN: 978-0-471-41526-8. URL: <https://www.wiley.com/en-us/Introduction+to+Solid+State+Physics%2C+8th+Edition-p-9780471415268>.
- [23] M.L. Mehta. *Random matrices*. Amsterdam: Elsevier/Academic Press, 2004.
- [24] Yuli V. Nazarov and Yaroslav M. Blanter. *Quantum Transport: Introduction to Nanoscience*. Cambridge, England, UK: Cambridge University Press, May 2009. ISBN: 978-0-52183246-5. DOI: [10.1017/CBO9780511626906](https://doi.org/10.1017/CBO9780511626906).
- [25] Xiao-Liang Qi, Taylor L. Hughes, and Shou-Cheng Zhang. “Topological field theory of time-reversal invariant insulators”. In: *Phys. Rev. B* 78.19 (Nov. 2008), p. 195424. ISSN: 2469-9969. DOI: [10.1103/PhysRevB.78.195424](https://doi.org/10.1103/PhysRevB.78.195424).
- [26] Xiao-Liang Qi and Shou-Cheng Zhang. “Topological insulators and superconductors”. In: *Rev. Mod. Phys.* 83.4 (Oct. 2011), pp. 1057–1110. ISSN: 1539-0756. DOI: [10.1103/RevModPhys.83.1057](https://doi.org/10.1103/RevModPhys.83.1057).

- [27] Roman-Pascal Riwar et al. “Multi-terminal Josephson junctions as topological matter - Nature Communications”. In: *Nat. Commun.* 7.11167 (Apr. 2016), pp. 1–5. ISSN: 2041-1723. DOI: [10.1038/ncomms11167](https://doi.org/10.1038/ncomms11167).
- [28] Masatoshi Sato and Yoichi Ando. “Topological superconductors: a review”. In: *Rep. Prog. Phys.* 80.7 (May 2017), p. 076501. ISSN: 0034-4885. DOI: [10.1088/1361-6633/aa6ac7](https://doi.org/10.1088/1361-6633/aa6ac7).
- [29] B. D. Simons and Boris L. Altshuler. “Universal velocity correlations in disordered and chaotic systems”. In: *Phys. Rev. Lett.* 70.26 (June 1993), pp. 4063–4066. ISSN: 1079-7114. DOI: [10.1103/PhysRevLett.70.4063](https://doi.org/10.1103/PhysRevLett.70.4063).
- [30] Berry Michael Victor. “Quantal phase factors accompanying adiabatic changes”. In: *Proc. R. Soc. Lond. A.* 392.1802 (Mar. 1984), pp. 45–57. DOI: [10.1098/rspa.1984.0023](https://doi.org/10.1098/rspa.1984.0023).
- [31] S. Washburn and R. A. Webb. “Quantum transport in small disordered samples from the diffusive to the ballistic regime”. In: *Rep. Prog. Phys.* 55.8 (Aug. 1992), pp. 1311–1383. ISSN: 0034-4885. DOI: [10.1088/0034-4885/55/8/004](https://doi.org/10.1088/0034-4885/55/8/004).
- [32] Hermann Weyl. “Elektron und Gravitation. I”. In: *Z. Phys.* 56.5 (May 1929), pp. 330–352. DOI: [10.1007/BF01339504](https://doi.org/10.1007/BF01339504).
- [33] Frank Wilczek and A. Zee. “Appearance of Gauge Structure in Simple Dynamical Systems”. In: *Phys. Rev. Lett.* 52.24 (June 1984), pp. 2111–2114. ISSN: 1079-7114. DOI: [10.1103/PhysRevLett.52.2111](https://doi.org/10.1103/PhysRevLett.52.2111).
- [34] Su-Yang Xu et al. “Discovery of a Weyl fermion semimetal and topological Fermi arcs”. In: *Science* (Aug. 2015). URL: <https://www.science.org/doi/10.1126/science.aaa9297>.
- [35] Su-Yang Xu et al. “Discovery of Lorentz-violating type II Weyl fermions in LaAlGe”. In: *Sci. Adv.* (June 2017). URL: <https://www.science.org/doi/10.1126/sciadv.1603266>.
- [36] Binghai Yan and Claudia Felser. “Topological Materials: Weyl Semimetals”. In: *Annu. Rev. Condens. Matter Phys.* 8.1 (Mar. 2017), pp. 337–354. ISSN: 1947-5454. DOI: [10.1146/annurev-conmatphys-031016-025458](https://doi.org/10.1146/annurev-conmatphys-031016-025458).
- [37] Xingjiang Zhou et al. “High-temperature superconductivity - Nature Reviews Physics”. In: *Nat. Rev. Phys.* 3 (July 2021), pp. 462–465. ISSN: 2522-5820. DOI: [10.1038/s42254-021-00324-3](https://doi.org/10.1038/s42254-021-00324-3).

2

FINE ENERGY SPLITTING OF OVERLAPPING ANDREEV BOUND STATES IN MULTITERMINAL SUPERCONDUCTING NANOSTRUCTURES

*It is better to be a warrior in a garden
than a gardener in war.*

Chinese proverb

This chapter has been published as Fine energy splitting of overlapping Andreev bound states in multiterminal superconducting nanostructures [25] and the data is available on <https://zenodo.org/record/4073382#.YfuORy8w1Zh>.

The superconducting nanodevices are in focus of modern experimental research, in particular because they are a promising platform for various qubit realizations, e.g. Josephson-based qubits of several kinds [31, 20, 44, 28, 9] or Majorana bound states [24, 27, 33, 3, 30]. These structures, containing superconductor-semiconductor or superconductor-insulator junctions, host Andreev bound states (ABS), which can also be used as a qubit [15, 23]. Andreev reflection between normal metal and superconductor was first discussed in Ref. [1], and has been a subject of intense theoretical and experimental research [10, 39, 40, 8, 17, 14, 26, 11, 12, 43] that spans far beyond quantum information topics. The variety of ABS in various nanostructures is so rich as to mimic almost any quantum state known in physics.

It is known and commonly used that the ABS forming in nanostructures are defined by the properties of the nanostructure, not depending on the details of electron scattering in the adjacent superconducting leads, which is a consequence of Anderson's theorem [5]. For short nanostructures between two leads, each transport channel with transmission T gives an ABS at the energy [7] $E = \pm \Delta \sqrt{1 - T \sin^2[(\phi_1 - \phi_2)/2]}$, Δ being the superconducting gap in the leads, $\phi_{1,2}$ being the superconducting phases of the leads. ABS extend to the leads at distances of the order of the correlation length ξ_0 , this is much larger than the nanostructure size. ABS can be realized in semiconducting-nanowire-superconducting structures, the technology of those has advanced strongly owing to the applications in the field of Majorana bound states [30, 2, 46, 19, 21], and can be characterized experimentally [46, 19]. There is much recent progress in multi-terminal devices [36, 34, 18] that has been partially inspired by theoretical predictions of Weyl points and quantized transconductance [37].

Very recent experimental and theoretical developments concern so-called Andreev molecules in various layouts [41, 35, 38, 29]. The term "molecule" refers to the situation where two single ABS have close energies, this enables their hybridization and formation of the superpositions. Refs. [41, 38] discuss ABS in quantum dots, where ABS overlap through the tunnel barrier separating the dots. Ref. [29] considers the hybridization of two Andreev quasi-states at two superconductor/ferromagnet interfaces that overlap in the superconductor. An interesting alternative has been put forward in Ref. [35]. The proposed three-terminal setup encompasses two single-channel junctions that connect three superconducting leads, see Fig. 2.1 (a). Two single ABS may overlap and hybridize in the middle lead. The overlap and the corresponding energy splitting must cease exponentially as $\exp\{-L/\xi_0\}$, provided the separation of the junctions $L \gg \xi_0$. The authors of Ref. [35] indicate that Andreev molecules have potential applications in quantum information, metrology, sensing, and molecular simulation.

In this Chapter we have evaluated the energy splitting of overlapping ABS. We have found that it is an interference effect similar to mesoscopic fluctuations of conductance [13]. Such fluctuations develop in the lead on the scale of ABS overlap that encompasses a large number of quantum channels. Importantly, this makes this energy splitting fine at the scale of Δ .

We have estimated the typical energy splitting $\delta_D \sim \Delta/\sqrt{N}$, N being the number of channels, that can be estimated as the inverse of the normal dimensionless resistance of the overlap region, $N \approx (RG_Q)^{-1}$, $G_Q \equiv e^2/(\pi\hbar)$ being conductance quantum. Therefore δ_D remains fine at the energy scale of Δ . This big difference in energy scales is known to

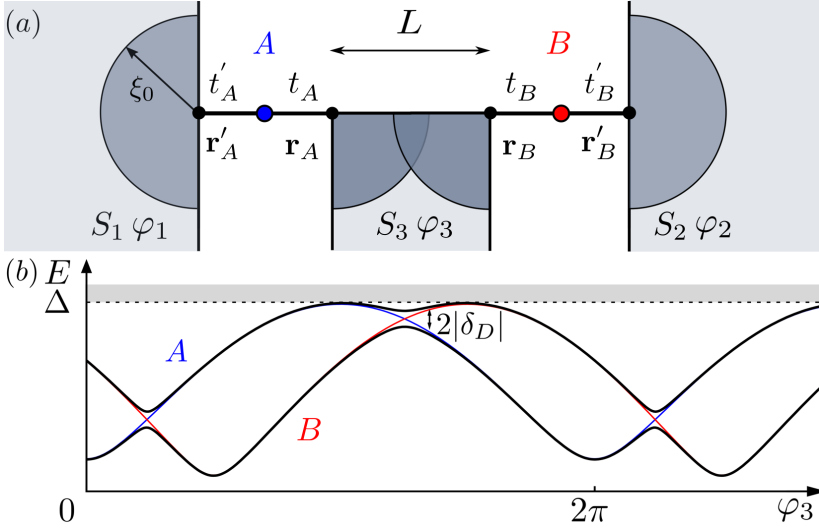


Figure 2.1: (a) The "Andreev molecule" setup. Two ABS are formed in the two single-channel junctions, A and B, that are separated by L and connect three superconducting leads $S_{1,2,3}$ with the same Δ . The ABS wave functions spread over the scale of ξ_0 , overlapping in S_3 . (b) The energy spectrum of ABSs versus φ_3 ($\varphi_1 = \pi$, $\varphi_2 = 3\pi/2$, the junction transmission coefficients being $T_A = 0.95$, $T_B = 0.98$), manifests avoided crossings at the degeneracy points. We show that the energy splitting at the crossings is fine even for a significant overlap, $\delta_D \propto \Delta\sqrt{RG_Q}$, where R being normal resistance of the overlap region.

facilitate various quantum manipulation schemes, simplest example of which we provide. We have derived concrete expressions for $\langle |\delta_D|^2 \rangle$, relating it to semiclassical propagation of an electron between the junctions, and employed it for an experimentally relevant setup. Observation of energy splitting gives an interesting and unusual way to see and explore mesoscopic fluctuations.

Let us first describe the setup under consideration (Fig. 2.1) in general terms specifying the details later. The setup consists of three superconducting leads, connected by two single-channel junctions, and there is an ABS formed in each junction. If one neglects their hybridization, their energies are $E_{A(B)} = \Delta\sqrt{1 - T_{A(B)} \sin^2[(\varphi_{1(2)} - \varphi_3)/2]}$. We plot the energies in Fig. 2.1 (b) for $\varphi_1 - \varphi_2 = \pi/2$ and $T_A = 0.95$, $T_B = 0.98$; the degeneracy at $E_A = E_B$ is avoided. The separation between the junctions is $L \gg \lambda_F$, λ_F being the Fermi wave length. This implies that the electron transport in the region covered by the ABS wave functions, occurs in a big number of transport channels. The exact number depends on the geometry of the device, material and morphology of the leads, and the detailed characteristics of electron transport, that can be ballistic, diffusive, or intermediate between the two. At the level of an estimate, all these details can be incorporated into the effective resistance R of the region spanned by the ABS wave functions, so that $N \sim (RG_Q)^{-1}$. The wave functions of the ABS overlap as shown in Fig. 2.1 (a) and hybridize. The hybridization is big near each avoided crossing and can be described with an off-diagonal matrix element δ_D , which is a complex number.

Let us estimate the energy splitting $2|\delta_D|$ near an avoided crossing. The energies of the states are $E_{A,B} \sim \Delta$. These states are formed by electrons coming in and out of a junction to/from the adjacent leads and returning as holes to the same junction. The electron wave function is distributed among N transport channels involved. The contributions of different channels to Andreev scattering amplitude come with the same sign and phase, this is precisely the reason for the energy of ABS not to depend on the details of the scattering in the leads. This implies that the contribution of each channel to the ABS energy can be estimated as Δ/N . As to δ_D , it is determined by the electron and hole propagation from the junction A to the junction B . Since these points are distinct and separated by $L \gg \lambda_F$ one expects the contributions of different channels to come with the different and generally random complex amplitudes. These random amplitudes may be related to mesoscopic fluctuations of electron propagation between the junctions A and B . Averaging over these random amplitudes leads to vanishing $\langle \delta_D \rangle = 0$. The average $\langle |\delta_D|^2 \rangle$ is contributed by independent contributions of N channels and therefore the energy splitting can be estimated as $|\delta_D| \sim \Delta/\sqrt{N} \sim \Delta\sqrt{RG_Q}$.

The junctions between the superconducting leads may have various characteristics, such as disorder, shape, material. It is known however [6] that the only characteristic relevant for ABS is the transmission of these junctions. Therefore we are free to choose any microscopic model so we opt for a convenient resonant impurity model [16, 47], that involves a localized state of energy E_{imp} with the tunnel couplings t and t' to the leads. We label with A and B these characteristics in the corresponding junctions, see Fig. 2.1 (a). The width of the resonant level is given by $\Gamma = 2\pi\nu(|t|^2 + |t'|^2)$, ν being the density of states assumed equal in all leads. To model weak energy dependence of the scattering we set $\Gamma \gg \Delta$, so the transmission coefficient of the junction A is

$$T_A = \frac{4\pi^2\nu^2|t_A|^2|t'_A|^2}{(\Gamma_A/2)^2 + E_{\text{imp},A}^2}, \quad (2.1)$$

and similar for the junction B .

To find the ABS energies we derive a Dyson equation for the Green's function $G_{ij}(E)$ defined at the resonant impurities $i, j = \{A, B\}$: $G(E) = ([G^0]^{-1} - \Sigma)^{-1}$, where the blocks are the matrices in the Nambu space $G_{AA,BB}^0 = (E - E_{\text{imp},A,B}\sigma_z)^{-1}$, and the self-energy part Σ describes the tunneling. The diagonal blocks are $\Sigma_{AA} = \mathcal{T}'_A G(\mathbf{r}'_A, \mathbf{r}'_A) \mathcal{T}_A'^* + \mathcal{T}_A G(\mathbf{r}_A, \mathbf{r}_A) \mathcal{T}_A^*$, where $\mathcal{T}_j = (t_j^*(\sigma_z + \sigma_0) + t_j(\sigma_z - \sigma_0))/2$, $j = \{A, B\}$, and $G(\mathbf{r}, \mathbf{r}')$ is a superconducting Green's function in the corresponding leads upon neglecting the tunneling, Σ_{BB} is similar. The Green's function in close points does not depend on the details of the scattering in the lead, this is a consequence of Anderson's theorem [5]. The non-diagonal blocks Σ_{AB} and Σ_{BA} are $\Sigma_{AB} = \mathcal{T}_A G(\mathbf{r}_A, \mathbf{r}_B) \mathcal{T}_B^*$ and $\Sigma_{BA} = \mathcal{T}_B G(\mathbf{r}_B, \mathbf{r}_A) \mathcal{T}_A^*$. We see that the diagonal blocks contain Green's functions in coinciding points, while non-diagonal ones contain Green's functions in two points separated by $L \gg \lambda_F$. Since Green's functions are associated with propagation amplitudes $G(\mathbf{r}_A, \mathbf{r}_B) \ll G(\mathbf{r}_A, \mathbf{r}_A), G(\mathbf{r}_B, \mathbf{r}_B)$. Thus $\Sigma_{AB}, \Sigma_{BA} \ll \Sigma_{AA}, \Sigma_{BB}$, and can be handled by means of the degenerate perturbation theory. This already implies $|\delta_D| \ll \Delta$.

The energies of ABS correspond to the poles of $G(E)$ [4], so we need to find zero eigenvalues of $G^{-1}(E)$. We find zero eigenvalues in each diagonal block and project $G^{-1}(E)$ onto the corresponding eigenvectors $|A\rangle$ and $|B\rangle$. We work near the crossing point E_0

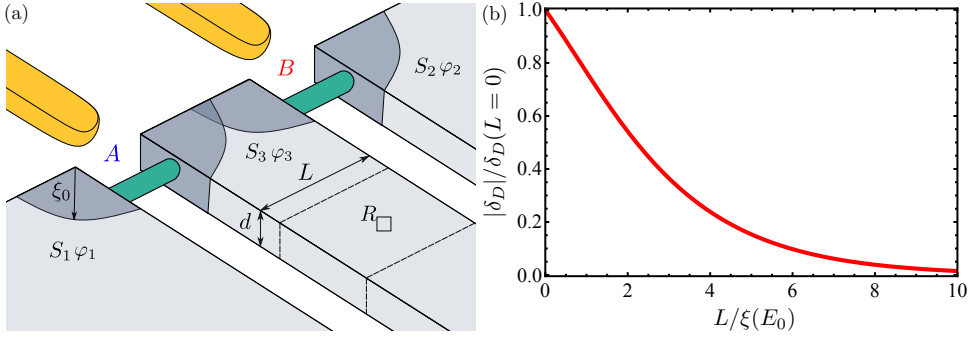


Figure 2.2: (a) The concrete setup under consideration comprises three superconducting leads covering a single-channel semiconducting nanowire. Two hybridizing ABSs are forming at the junctions A, B . The gates (yellow) affect the potential in the wire and might be used to tune the transmission of the junctions. The middle lead is a film of thickness d and width L and is characterized by the resistance per square R_{\square} . The ABS wave functions overlap strongly provided $L \lesssim \xi_0$. (b) Dependence of the energy splitting $|\delta_D|/|\delta_D(L=0)|$ on L . The splitting vanishes exponentially upon increasing L .

where the unperturbed ABS energies are almost degenerate $E_A \approx E_B \approx E_0$. Expanding up to linear order near the crossing point and transforming $G^{-1}(E)$ we find that ABS energies are obtained from the effective Hamiltonian describing the level repulsion, $H_{\text{eff}} = \begin{pmatrix} E_A & \delta_D \\ \delta_D^* & E_B \end{pmatrix}$, where

$$\delta_D = -\frac{\langle A|\Sigma_{AB}|B\rangle\sqrt{\Delta^2 - E_0^2}}{\sqrt{\Gamma_A\Gamma_B}} \propto G(\mathbf{r}_A, \mathbf{r}_B). \quad (2.2)$$

The Green's function $G(\mathbf{r}_A, \mathbf{r}_B)$ changes much on a scale of λ_F upon changing the position of \mathbf{r}_B . This is the origin of mesoscopic fluctuations in electron transport [32]. The components of $G(\mathbf{r}_A, \mathbf{r}_B)$ can be regarded as random values with zero averages. The informative quantities are the products of these components averaged over \mathbf{r}_B at the scale exceeding λ_F . These averaged products can be expressed with a normal-state quasiclassical propagator [22] $\mathcal{P}(\mathbf{r}_A, \mathbf{r}_B, t)$, that gives the probability to find an electron at \mathbf{r}_B at the time moment t provided it was at \mathbf{r}_A at $t=0$ (Greek letters denote Nambu indices):

$$\begin{aligned} \langle G(\mathbf{r}_A, \mathbf{r}_B)^{\alpha\gamma*} G(\mathbf{r}_A, \mathbf{r}_B)^{\beta\nu} \rangle &= \\ &= \frac{\pi v}{2(\Delta^2 - E^2)} \int dt \mathcal{P}(\mathbf{r}_A, \mathbf{r}_B, t) e^{-2\sqrt{\Delta^2 - E^2}|t|} \\ &\times [\delta_{\alpha\gamma} \delta_{\beta\nu} \delta_{\alpha\beta} (2\Delta^2 - E^2) \\ &+ \Delta E ((1 - \delta_{\alpha\gamma}) \delta_{\beta\nu} e^{-i\epsilon_{\alpha\gamma}\varphi_3} - \delta_{\alpha\gamma} (1 - \delta_{\beta\nu}) e^{i\epsilon_{\beta\nu}\varphi_3}) \\ &+ \Delta^2 (\delta_{\alpha\beta} \delta_{\gamma\nu} (1 - \delta_{\alpha\gamma}) - \delta_{\alpha\gamma} \delta_{\beta\nu} (1 - \delta_{\alpha\beta}) \\ &+ \delta_{\alpha\nu} \delta_{\gamma\beta} (1 - \delta_{\alpha\gamma}) e^{-i2\epsilon_{\alpha\gamma}\varphi_3}]. \end{aligned} \quad (2.3)$$

(Here we have corrected an unfortunate mistake in the coefficient in Eq. 3 of Ref. [25]) Let us reproduce the main estimation of this Chapter, $|\delta_D| \propto 1/\sqrt{RG_Q}$, with this method. Combining Eqs. 2.2 and 2.3 we estimate $(|\delta_D|/\Delta)^2 \propto v^{-1} \int dt \mathcal{P}(t) e^{-\Delta|t|}$. In the course

of its propagation, an electron covers the region whose spatial dimensions are defined by the dwell time $t_{\text{dw}} \simeq \Delta^{-1}$. The $\mathcal{P}(t_{\text{dw}})$ is estimated as inverse volume V of the region. With this we can estimate $(|\delta_D|/\Delta)^2 \sim t_{\text{dw}}\delta_s$, $\delta_s = (\nu V)^{-1}$. If we now compare this with the Thouless estimation [42] of the conductance of such region, $G_{\text{Th}} \simeq G_Q(\delta_s t_{\text{dw}})^{-1}$, we reproduce $(|\delta_D|/\Delta)^2 \propto R_{\text{Th}}G_Q$.

Let us specify the concrete setup. It comprises the semiconducting nanowire covered by three superconducting leads, see Fig. 2.2 (a); such devices have been recently fabricated [35]. The middle lead is a film of thickness d and width L . If $L \lesssim \xi_0$, the ABS wave functions overlap strongly. We assume diffusive transport in the lead, which is characterized by the resistance per square R_\square . We also assume that the interface between the nanowire and the metal is sufficiently transparent, so that the electrons escape the nanowire to metal at the distances $\ll \xi_0$.

The semiclassical propagator in the film obeys diffusion equation

$$\left(\frac{\partial}{\partial t} - D\nabla^2\right)\mathcal{P}(\mathbf{r}, t) = \frac{1}{d}\delta(t)\delta(\mathbf{r} - \mathbf{r}_A). \quad (2.4)$$

This diffusion equation is subject to boundary conditions of zero probability flow across all boundaries. One satisfies these boundary conditions introducing infinite number of imaginary sources, spaced with $2L$. The propagator we obtain is

$$\mathcal{P}(\mathbf{r}_A, \mathbf{r}_B, t) = \frac{1}{dL}\sqrt{\frac{1}{\pi D|t|}} \sum_{n=-\infty}^{\infty} (-1)^n e^{-D\frac{\pi^2}{L^2}n^2|t|}. \quad (2.5)$$

With this we compute $|\delta_D|^2$ using Eqs. 2.2 and 2.3 to obtain

$$\frac{|\delta_D|^2}{\Delta^2} = \frac{\pi}{2}MG_QR_{\text{eff}}F\left(\frac{L}{\xi(E_0)}\right), \quad R_{\text{eff}} = R_\square \frac{\xi(E_0)}{2\pi L}, \quad (2.6)$$

with R_{eff} being the effective resistance of the part of the lead covered by ABS wave functions, the dimensionless $F(z) = 4z/\pi \sum_{n=0}^{\infty} K_0((2n+1)z)$, K_0 being modified Bessel function of the second kind, $F(0) = 1$, incorporates information of the decay of ABS wave functions at the scale of $\xi(E) = \xi_0(1 - E^2/\Delta^2)^{-1/4}$, that is the energy-dependent correlation length. The prefactor $M \simeq 1$ incorporates information about transmissions of the junctions

$$M = 2|t_A|^2|t_B|^2[2\cos(\chi_A - \chi_B)E^2 + (2 + \cos(\chi_A + \chi_B) - \cos(\chi_A - \chi_B))\Delta^2 \quad (2.7)$$

$$- 2E\Delta(\cos\chi_A + \cos\chi_B)]/[\Delta^2(|t_A|^2 + |t'_A|^2)(|t_B|^2 + |t'_B|^2)] \quad (2.8)$$

, where χ_A and χ_B are the phases of the eigenvectors $|A\rangle$ and $|B\rangle$, respectively, with $e^{i\chi_A} = [|t'_A|^2 e^{i\varphi_1} + |t_A|^2 \Delta / (E[|t_A|^2 + |t'_A|^2])]$ and analogously for χ_B . Here, φ_1 and φ_2 denote phase differences with respect to φ_3 and we set $E_{\text{imp},A,B} = 0$. $M \rightarrow 1$, in the limit $E_0 \rightarrow 0$, this requires $T_{A,B} \rightarrow 1$. Thus in the limiting cases we have

$$\frac{|\delta_D|^2}{\Delta^2} = \begin{cases} \frac{\pi}{2}MG_QR_{\text{eff}}, & L \rightarrow 0, \\ MG_QR_{\text{eff}}\sqrt{\frac{2\pi L}{\xi(E_0)}}e^{-\frac{L}{\xi(E_0)}}, & L \rightarrow \infty, \end{cases} \quad (2.9)$$

We plot the normalized energy splitting $|\delta_D|/\delta_D(L=0)$ versus L in Fig. 2.2 (b), $\delta_D(L=0) = \Delta\sqrt{\pi MG_QR_{\text{eff}}/2}$.

For the experimentally relevant parameters $\Delta = 200 \mu\text{eV}$, $\xi_0 = 96 \text{ nm}$ [46], $R_\square = 1.43 \Omega$ [45], $L = 50 \text{ nm}$, $T_A = T_B = 1$, we find the crossing point at $\varphi_2 = 2.36$, $\varphi_1 = 3.93$, and $E_0 = 76.54 \mu\text{eV}$, and obtain the splitting $2|\delta_D| = 1.79 \mu\text{eV}$. The value for $|\delta_D| \simeq \Delta/250$ even though $R_\square G_Q \approx 10^{-4}$, which seems to be small.

The separation of scales between δ_D and Δ permits interesting quantum manipulation schemes for involved states. Let us describe the simplest one: quasiparticle swap between A and B . Let us take a point in parametric space of $\varphi_{1,2,3}$, where the ABS energies are well-split (for instance, $\varphi_3 = 0$ in Fig. 2.1 (b)) and put a quasiparticle to the state A . We pass the avoided crossing slowly to avoid Landau-Zener tunneling in this point (for instance, changing φ_3 from 0 to $\pi/2$), this brings the quasiparticle to B . If we get back to the initial point very quickly, the quasiparticle will remain in B , this completes the manipulation protocol. The same swap occurs if the quasiparticle is in B initially.

There is an interesting case, when both junctions have almost ideal transmission $T_{A,B} = 1 - R_{A,B}$, $R_{A,B} \ll 1$, and $\varphi_{1,2} = \pi + \delta\varphi_{1,2}$, $\delta\varphi_{1,2} \ll 1$. In this case the crossing occurs at $E_0 \ll \Delta$, which can also be comparable with $|\delta_D|$. The perturbation theory does not work here, but we can describe the situation with the following 4×4 effective Hamiltonian:

$$H_{\text{eff}} = \Delta \begin{pmatrix} 0 & h_A & g & f \\ h_A^* & 0 & f & -g \\ g & f & 0 & h_B \\ f & -g & h_B^* & 0 \end{pmatrix}, \quad (2.10)$$

where $h_{A,B} = \sqrt{R_{A,B}} + i\delta\varphi_{1,2}$. The terms f and g come from $\Sigma_{AB,BA}$, $\langle f^2 \rangle = \langle g^2 \rangle = 16\pi^3 v^2 |t_A|^2 |t_B|^2 G_Q R_{\text{eff}} F(L/\xi(E_0))$. In the limit $R_{A,B} = 0$ the ABS energies are given by

$$E = \sqrt{\tilde{\delta}^2 + \frac{(\delta\varphi)^2}{4} + \frac{\Phi^2}{4} \pm \Phi \sqrt{\tilde{\delta}^2 + \frac{(\delta\varphi)^2}{4}}}, \quad (2.11)$$

where $\tilde{\delta} = \sqrt{f^2 + g^2}$, $\delta\varphi_{1,2} = \Phi/2 \pm \delta\varphi/2$. Interestingly, if $|\Phi| < 2\tilde{\delta}$ the energies never cross zero, while there are two symmetric zero-energy crossings if $|\Phi| > 2\tilde{\delta}$, Fig. 2.3 (a), (b). In this approximation two ABS energies are precisely degenerate at $\Phi = 0$, this degeneracy is lifted upon increasing energy. At finite $R_{A,B}$ the zero-energy crossings are avoided, Fig. 2.3 (c), (d).

Before we conclude let us mention that the fact that the energy splitting is fine makes relevant a set of topics to research that we list here. For semiconducting nanowires the electron escape length can be $\gtrsim L$, this confines the overlap region to the nanowire and greatly enhance δ_D . The spin-orbit splitting [48] of ABS that is usually negligible can become relevant for small δ_D . Many-body effects shall provide small energy differences for doublet and singlet quasiparticle states in ABS [43]. Interestingly, the hybridization of degenerate singlet states in the setup under investigation can also occur without direct overlap of ABS wave functions, that is at $L \gg \xi_0$. It would be also interesting to consider with our method the ABS in superconductor/ferromagnetic structures [29].

We have investigated the energy splitting in an Andreev molecule, where in distinction from the common molecules the quantum superpositions are formed at macroscopic level and can be engineered changing the superconducting phases. Such molecules may become

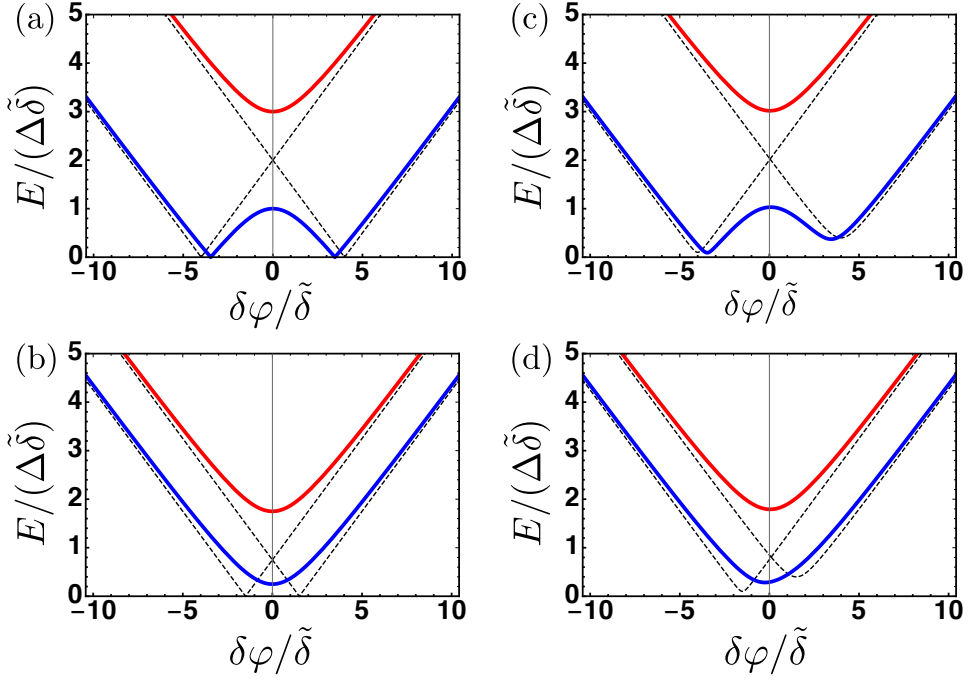


Figure 2.3: Spectra of the system for $E \sim 0$ for $f/\tilde{\delta} = \sqrt{3/5}$, $g/\tilde{\delta} = \sqrt{2/5}$, and (a) $\Phi/\tilde{\delta} = 4$, $R_A = R_B = 0$; (b) $\Phi/\tilde{\delta} = 1.5$, $R_A = R_B = 0$; (c) $\Phi/\tilde{\delta} = 4$ and $\sqrt{R_A}/\tilde{\delta} = 0.1$, $\sqrt{R_B}/\tilde{\delta} = 0.4$; (d) $\Phi/\tilde{\delta} = 1.5$ and $\sqrt{R_A}/\tilde{\delta} = 0.1$, $\sqrt{R_B}/\tilde{\delta} = 0.4$. The dashed line shows the case of $f = g = 0$ and for other parameters as described. The asymmetry in (c) and (d) comes from $R_A \neq R_B$.

a playground for interesting few-body quantum interactions. We establish that the energy splitting is fine even in the case of strong overlap. This is in contrast to common molecules either natural or artificially made in nanostructures. We relate the splitting to mesoscopic fluctuations, so that the splitting manifests the intrinsic randomness of the setup and provides the means of its experimental observation. The smallness of the splitting opens up possibilities for quantum manipulation and application as mentioned in Ref. [35].

BIBLIOGRAPHY

- [1] A. F. Andreev, “The Thermal Conductivity of the Intermediate State in Superconductors,” *Soviet Physics-JETP*, Vol. 19, No. 6, 1964, pp. 1228-1232. - References - Scientific Research Publishing. [Online; accessed 19. Dec. 2021]. Dec. 2021. URL: [https://www.scirp.org/\(S\(351jmbntvnsjtlaadkozje\)\)/reference/ReferencesPapers.aspx?ReferenceID=108402](https://www.scirp.org/(S(351jmbntvnsjtlaadkozje))/reference/ReferencesPapers.aspx?ReferenceID=108402).
- [2] S. M. Albrecht et al. “Exponential protection of zero modes in Majorana islands - Nature”. In: *Nature* 531 (Mar. 2016), pp. 206–209. ISSN: 1476-4687. DOI: [10.1038/nature17162](https://doi.org/10.1038/nature17162).
- [3] Jason Alicea. “New directions in the pursuit of Majorana fermions in solid state systems”. In: *Rep. Prog. Phys.* 75.7 (June 2012), p. 076501. ISSN: 0034-4885. DOI: [10.1088/0034-4885/75/7/076501](https://doi.org/10.1088/0034-4885/75/7/076501).
- [4] Alexander Altland and Ben D. Simons. *Condensed Matter Field Theory*. Cambridge, England, UK: Cambridge University Press, Mar. 2010. ISBN: 978-0-52176975-4. DOI: [10.1017/CBO9780511789984](https://doi.org/10.1017/CBO9780511789984).
- [5] P. W. Anderson. “Theory of dirty superconductors”. In: *J. Phys. Chem. Solids* 11.1 (Sept. 1959), pp. 26–30. ISSN: 0022-3697. DOI: [10.1016/0022-3697\(59\)90036-8](https://doi.org/10.1016/0022-3697(59)90036-8).
- [6] C. W. J. Beenakker. “Random-matrix theory of quantum transport”. In: *Rev. Mod. Phys.* 69.3 (July 1997), pp. 731–808. ISSN: 1539-0756. DOI: [10.1103/RevModPhys.69.731](https://doi.org/10.1103/RevModPhys.69.731).
- [7] C. W. J. Beenakker. “Universal limit of critical-current fluctuations in mesoscopic Josephson junctions”. In: *Phys. Rev. Lett.* 67.27 (Dec. 1991), pp. 3836–3839. ISSN: 1079-7114. DOI: [10.1103/PhysRevLett.67.3836](https://doi.org/10.1103/PhysRevLett.67.3836).
- [8] F. S. Bergeret et al. “Theory of Microwave-Assisted Supercurrent in Quantum Point Contacts”. In: *Phys. Rev. Lett.* 105.11 (Sept. 2010), p. 117001. ISSN: 1079-7114. DOI: [10.1103/PhysRevLett.105.117001](https://doi.org/10.1103/PhysRevLett.105.117001).
- [9] A. J. Berkley et al. “Entangled Macroscopic Quantum States in Two Superconducting Qubits”. In: *Science* (June 2003). URL: https://www.science.org/doi/10.1126/science.1084528?url_ver=Z39.88-2003%ED%94%AF_id=ori:rid:crossref.org%ED%94%AF_dat=cr_pub%20%200pubmed.
- [10] G. E. Blonder, M. Tinkham, and T. M. Klapwijk. “Transition from metallic to tunneling regimes in superconducting microconstrictions: Excess current, charge imbalance, and supercurrent conversion”. In: *Phys. Rev. B* 25.7 (Apr. 1982), pp. 4515–4532. ISSN: 2469-9969. DOI: [10.1103/PhysRevB.25.4515](https://doi.org/10.1103/PhysRevB.25.4515).

- [11] L. Bretheau et al. “Theory of microwave spectroscopy of Andreev bound states with a Josephson junction”. In: *Phys. Rev. B* 90.13 (Oct. 2014), p. 134506. ISSN: 2469-9969. DOI: [10.1103/PhysRevB.90.134506](https://doi.org/10.1103/PhysRevB.90.134506).
- [12] Landry Bretheau et al. “Tunnelling spectroscopy of Andreev states in graphene - Nature Physics”. In: *Nat. Phys.* 13 (Aug. 2017), pp. 756–760. ISSN: 1745-2481. DOI: [10.1038/nphys4110](https://doi.org/10.1038/nphys4110).
- [13] Sudip Chakravarty and Albert Schmid. “Weak localization: The quasiclassical theory of electrons in a random potential”. In: *Phys. Rep.* 140.4 (July 1986), pp. 193–236. ISSN: 0370-1573. DOI: [10.1016/0370-1573\(86\)90027-X](https://doi.org/10.1016/0370-1573(86)90027-X).
- [14] F. Chiodi et al. “Probing the dynamics of Andreev states in a coherent Normal/Superconducting ring - Scientific Reports”. In: *Sci. Rep.* 1.3 (June 2011), pp. 1–6. ISSN: 2045-2322. DOI: [10.1038/srep00003](https://doi.org/10.1038/srep00003).
- [15] Nikolai M. Chtchelkatchev and Yu. V. Nazarov. “Andreev Quantum Dots for Spin Manipulation”. In: *Phys. Rev. Lett.* 90.22 (June 2003), p. 226806. ISSN: 1079-7114. DOI: [10.1103/PhysRevLett.90.226806](https://doi.org/10.1103/PhysRevLett.90.226806).
- [16] J. C. Cuevas, A. Levy Yeyati, and A. Martín-Rodero. “Kondo effect in normal-superconductor quantum dots”. In: *Phys. Rev. B* 63.9 (Feb. 2001), p. 094515. ISSN: 2469-9969. DOI: [10.1103/PhysRevB.63.094515](https://doi.org/10.1103/PhysRevB.63.094515).
- [17] R. S. Deacon et al. “Tunneling Spectroscopy of Andreev Energy Levels in a Quantum Dot Coupled to a Superconductor”. In: *Phys. Rev. Lett.* 104.7 (Feb. 2010), p. 076805. ISSN: 1079-7114. DOI: [10.1103/PhysRevLett.104.076805](https://doi.org/10.1103/PhysRevLett.104.076805).
- [18] Anne W. Draelos et al. “Supercurrent Flow in Multiterminal Graphene Josephson Junctions”. In: *Nano Lett.* 19.2 (Feb. 2019), pp. 1039–1043. ISSN: 1530-6984. DOI: [10.1021/acs.nanolett.8b04330](https://doi.org/10.1021/acs.nanolett.8b04330).
- [19] M. F. Goffman et al. “Conduction channels of an InAs-Al nanowire Josephson weak link”. In: *New J. Phys.* 19.9 (Sept. 2017), p. 092002. ISSN: 1367-2630. DOI: [10.1088/1367-2630/aa7641](https://doi.org/10.1088/1367-2630/aa7641).
- [20] Siyuan Han et al. “Time-Resolved Measurement of Dissipation-Induced Decoherence in a Josephson Junction”. In: *Science* (Aug. 2001). URL: https://www.science.org/doi/10.1126/science.1062266?url_ver=Z39.88-2003%ED%94%AF_id=ori:rid:crossref.org%ED%94%AF_dat=cr_pub%20%200pubmed.
- [21] M. Hays et al. “Direct Microwave Measurement of Andreev-Bound-State Dynamics in a Semiconductor-Nanowire Josephson Junction”. In: *Phys. Rev. Lett.* 121.4 (July 2018), p. 047001. ISSN: 1079-7114. DOI: [10.1103/PhysRevLett.121.047001](https://doi.org/10.1103/PhysRevLett.121.047001).
- [22] F. W. J. Hekking and Yu. V. Nazarov. “Subgap conductivity of a superconductor–normal-metal tunnel interface”. In: *Phys. Rev. B* 49.10 (Mar. 1994), pp. 6847–6852. ISSN: 2469-9969. DOI: [10.1103/PhysRevB.49.6847](https://doi.org/10.1103/PhysRevB.49.6847).
- [23] C. Janvier et al. “Coherent manipulation of Andreev states in superconducting atomic contacts”. In: *Science* (Sept. 2015). URL: <https://www.science.org/doi/10.1126/science.aab2179>.

- [24] A. Yu Kitaev. “Unpaired Majorana fermions in quantum”. In: *Phys.-Usp.* 44.10S (Oct. 2001), pp. 131–136. ISSN: 1468-4780. DOI: [10.1070/1063-7869/44/10s/s29](https://doi.org/10.1070/1063-7869/44/10s/s29).
- [25] Viktoriia Kornich, Hristo S. Barakov, and Yuli V. Nazarov. “Fine energy splitting of overlapping Andreev bound states in multiterminal superconducting nanostructures”. In: *Phys. Rev. Res.* 1.3 (Oct. 2019), p. 033004. ISSN: 2643-1564. DOI: [10.1103/PhysRevResearch.1.033004](https://doi.org/10.1103/PhysRevResearch.1.033004).
- [26] Eduardo J. H. Lee et al. “Spin-resolved Andreev levels and parity crossings in hybrid superconductor–semiconductor nanostructures - Nature Nanotechnology”. In: *Nat. Nanotechnol.* 9 (Jan. 2014), pp. 79–84. ISSN: 1748-3395. DOI: [10.1038/nnano.2013.267](https://doi.org/10.1038/nnano.2013.267).
- [27] Roman M. Lutchyn, Jay D. Sau, and S. Das Sarma. “Majorana Fermions and a Topological Phase Transition in Semiconductor-Superconductor Heterostructures”. In: *Phys. Rev. Lett.* 105.7 (Aug. 2010), p. 077001. ISSN: 1079-7114. DOI: [10.1103/PhysRevLett.105.077001](https://doi.org/10.1103/PhysRevLett.105.077001).
- [28] John M. Martinis et al. “Rabi Oscillations in a Large Josephson-Junction Qubit”. In: *Phys. Rev. Lett.* 89.11 (Aug. 2002), p. 117901. ISSN: 1079-7114. DOI: [10.1103/PhysRevLett.89.117901](https://doi.org/10.1103/PhysRevLett.89.117901).
- [29] Georgo Metalidis et al. “Nonlocal conductance via overlapping Andreev bound states in ferromagnet-superconductor heterostructures”. In: *Phys. Rev. B* 82.18 (Nov. 2010), p. 180503. ISSN: 2469-9969. DOI: [10.1103/PhysRevB.82.180503](https://doi.org/10.1103/PhysRevB.82.180503).
- [30] V. Mourik et al. “Signatures of Majorana Fermions in Hybrid Superconductor-Semiconductor Nanowire Devices”. In: *Science* (May 2012). URL: https://www.science.org/doi/10.1126/science.1222360?url_ver=Z39.88-2003%ED%94%AF_id=ori:rid:crossref.org%ED%94%AF_dat=cr_pub%20%200pubmed.
- [31] Y. Nakamura, C. D. Chen, and J. S. Tsai. “Spectroscopy of Energy-Level Splitting between Two Macroscopic Quantum States of Charge Coherently Superposed by Josephson Coupling”. In: *Phys. Rev. Lett.* 79.12 (Sept. 1997), pp. 2328–2331. ISSN: 1079-7114. DOI: [10.1103/PhysRevLett.79.2328](https://doi.org/10.1103/PhysRevLett.79.2328).
- [32] Yuli V. Nazarov and Yaroslav M. Blanter. *Quantum Transport: Introduction to Nanoscience*. Cambridge, England, UK: Cambridge University Press, May 2009. ISBN: 978-0-52183246-5. DOI: [10.1017/CBO9780511626906](https://doi.org/10.1017/CBO9780511626906).
- [33] Yuval Oreg, Gil Refael, and Felix von Oppen. “Helical Liquids and Majorana Bound States in Quantum Wires”. In: *Phys. Rev. Lett.* 105.17 (Oct. 2010), p. 177002. ISSN: 1079-7114. DOI: [10.1103/PhysRevLett.105.177002](https://doi.org/10.1103/PhysRevLett.105.177002).
- [34] Natalia Pankratova et al. “Multiterminal Josephson Effect”. In: *Phys. Rev. X* 10.3 (Sept. 2020), p. 031051. ISSN: 2160-3308. DOI: [10.1103/PhysRevX.10.031051](https://doi.org/10.1103/PhysRevX.10.031051).
- [35] J.-D. Pillet et al. “Nonlocal Josephson Effect in Andreev Molecules”. In: *Nano Lett.* 19.10 (Oct. 2019), pp. 7138–7143. ISSN: 1530-6984. DOI: [10.1021/acs.nanolett.9b02686](https://doi.org/10.1021/acs.nanolett.9b02686).

- [36] Sébastien R. Plissard et al. “Formation and electronic properties of InSb nanocrosses - Nature Nanotechnology”. In: *Nat. Nanotechnol.* 8 (Nov. 2013), pp. 859–864. ISSN: 1748-3395. DOI: [10.1038/nnano.2013.198](https://doi.org/10.1038/nnano.2013.198).
- [37] Roman-Pascal Riwar et al. “Multi-terminal Josephson junctions as topological matter - Nature Communications”. In: *Nat. Commun.* 7.11167 (Apr. 2016), pp. 1–5. ISSN: 2041-1723. DOI: [10.1038/ncomms11167](https://doi.org/10.1038/ncomms11167).
- [38] Zoltán Scherübl, András Pályi, and Szabolcs Csonka. “Transport signatures of an Andreev molecule in a quantum dot–superconductor–quantum dot setup”. In: *Beilstein J. Nanotechnol.* 10.1 (Feb. 2019), pp. 363–378. ISSN: 2190-4286. DOI: [10.3762/bjnano.10.36](https://doi.org/10.3762/bjnano.10.36).
- [39] A. L. Shelankov. “Transition from metallic to tunneling regimes in superconducting microconstrictions: Excess current, charge imbalance, and supercurrent conversion”. In: *Fiz. Tverd. Tela (Leningrad)* 26.981 (Apr. 1984), pp. 4515–4532. ISSN: 2469-9969. DOI: [10.1103/PhysRevB.25.4515](https://doi.org/10.1103/PhysRevB.25.4515).
- [40] R. J. Soulen Jr. et al. “Measuring the Spin Polarization of a Metal with a Superconducting Point Contact”. In: *Science* (Oct. 1998). DOI: [10.1126/science.282.5386.85](https://doi.org/10.1126/science.282.5386.85).
- [41] Zhaoen Su et al. “Andreev molecules in semiconductor nanowire double quantum dots - Nature Communications”. In: *Nat. Commun.* 8.585 (Sept. 2017), pp. 1–6. ISSN: 2041-1723. DOI: [10.1038/s41467-017-00665-7](https://doi.org/10.1038/s41467-017-00665-7).
- [42] D. J. Thouless. “Electrons in disordered systems and the theory of localization”. In: *Phys. Rep.* 13.3 (Oct. 1974), pp. 93–142. ISSN: 0370-1573. DOI: [10.1016/0370-1573\(74\)90029-5](https://doi.org/10.1016/0370-1573(74)90029-5).
- [43] L. Tosi et al. “Spin-Orbit Splitting of Andreev States Revealed by Microwave Spectroscopy”. In: *Phys. Rev. X* 9.1 (Jan. 2019), p. 011010. ISSN: 2160-3308. DOI: [10.1103/PhysRevX.9.011010](https://doi.org/10.1103/PhysRevX.9.011010).
- [44] D. Vion et al. “Manipulating the Quantum State of an Electrical Circuit”. In: *Science* (May 2002). URL: https://www.science.org/doi/10.1126/science.1069372?url_ver=Z39.88-2003%ED%94%AF_id=ori:rid:crossref.org%ED%94%AF_dat=cr_pub%20%200pubmed.
- [45] David J. van Woerkom, Attila Geresdi, and Leo P. Kouwenhoven. “One minute parity lifetime of a NbTiN Cooper-pair transistor - Nature Physics”. In: *Nat. Phys.* 11 (July 2015), pp. 547–550. ISSN: 1745-2481. DOI: [10.1038/nphys3342](https://doi.org/10.1038/nphys3342).
- [46] David J. van Woerkom et al. “Microwave spectroscopy of spinful Andreev bound states in ballistic semiconductor Josephson junctions - Nature Physics”. In: *Nat. Phys.* 13 (Sept. 2017), pp. 876–881. ISSN: 1745-2481. DOI: [10.1038/nphys4150](https://doi.org/10.1038/nphys4150).
- [47] A. Levy Yeyati et al. “Resonant tunneling through a small quantum dot coupled to superconducting leads”. In: *Phys. Rev. B* 55.10 (Mar. 1997), R6137–R6140(R). ISSN: 2469-9969. DOI: [10.1103/PhysRevB.55.R6137](https://doi.org/10.1103/PhysRevB.55.R6137).
- [48] T. Yokoyama and Yu. V. Nazarov. “Magnetic anisotropy of critical current in nanowire Josephson junction with spin-orbit interaction”. In: *Europhys. Lett.* 108.4 (Nov. 2014), p. 47009. ISSN: 0295-5075. DOI: [10.1209/0295-5075/108/47009](https://doi.org/10.1209/0295-5075/108/47009).

3

OVERLAPPING ANDREEV STATES IN SEMICONDUCTING NANOWIRES: COMPETITION OF ONE-DIMENSIONAL AND THREE-DIMENSIONAL PROPAGATION

*To a man with a hammer
everything seems like a nail*

Mark Twain

This chapter has been published as Overlapping Andreev states in semiconducting nanowires: Competition of one-dimensional and three-dimensional propagation [14] and the data is available on https://zenodo.org/record/4073374#.YfuWVC8w2_U.

3.1. INTRODUCTION

The nanostructures made of semiconducting nanowires in contact with bulk superconducting leads or with superconducting shell are often used in the research aimed to achieve the Majorana-based qubits[19, 24, 21, 1]. This boosted the fabrication technology of such nanostructures that has progressed significantly over the last decade[11, 6, 35, 34, 5, 7, 28, 17, 3, 31, 36, 8, 15, 16, 10]. The improved technology makes it possible to realize more sophisticated and multi-functional setups that involve multiple superconducting terminals and gate electrodes. As one of the first steps in this direction, a setup of an "Andreev molecule" has been recently proposed in Ref. [26]. In this setup, a nanowire is covered with three superconducting electrodes (Fig. 3.1). The pieces of the nanowire not covered by electrodes form two Josephson junctions. Each junction can host an Andreev bound state (ABS) emerging from the Andreev scattering in the nanowire covered by a superconductor. If the separation L between the junctions is not too big, these states overlap and hybridize. This reminds a simple model of a diatomic molecule where two atomic states are hybridized, this analogy justifies the term. Different setups concerning Andreev molecules have been considered in Refs. [33, 30, 20]. In such simple artificial molecules, in distinction from atomic and molecular physics, the quantum states can be engineered and tuned by changing the parameters. Thus they can be a testbed for more complicated few-body systems, perhaps even actual molecules. The presence of tunable discrete levels and the peculiarities of the spectrum can be utilized in resonant and quantum computing devices.

We have considered the Andreev molecule setup suggested in Ref. [26] in our recent work[13]. We have shown that the energy splitting δE at the degeneracy point of two ABS is much smaller than the superconducting gap, Δ . The small parameter involved is an effective resistance of the lead where the ABS overlap, R , and $\delta E \simeq \sqrt{RG_Q}\Delta$, $G_Q \equiv e^2/(\pi\hbar)$ being the conductance quantum. For the present setup, the resistance R by order of the value is the resistance of the lead between the junctions, assuming the lead is in normal state. More precise definition is elaborated in Sec. 3.11. However, this conclusion is based on the assumption of quick electron transfer from the nanowire to the lead. This does not have to be a general case. If the contact between the nanowire and the superconducting lead is not very good[2, 12, 9], the electrons can stay in a nanowire for a sufficient time to propagate between the junctions without escaping to the lead. In this case, the ABS mainly overlap in the nanowire rather than in the lead, this results in much stronger hybridization[26, 36]. The 1D propagation in the wire brings about quite different and various physics, so the present manuscript is not an extension of Ref.[13].

In this work, we consider and analyse a number of regimes where 1D or 3D propagation dominate, or the two compete with each other. To characterize the contact between the lead and the nanowire, we use τ , the time a normal electron spends in the nanowire before escaping to the lead (Similar model has been considered in Refs. [29, 32], in their notations, $\tau = \gamma^{-1}$). This gives a correlation length $\xi_w = v_w\tau$, v_w being a typical electron velocity in the wire, that defines a spread of ABS wavefunction in the wire. The condition $L \ll \xi_w$ defines the regime of strong 1D hybridization (see Fig. 3.2). The opposite condition defines the regime of weak 1D hybridization, where the ABS are almost independent except the degeneracy points where they split with $\delta E \simeq \Delta \exp(-L/\xi_w)$. However, this does not exhaust the regimes. If $\exp(-L/\xi_w) \simeq \sqrt{RG_Q}$, the overlaps in the wire and in the lead become comparable, and we expect the regime of the competition of 1D and 3D propagation. At

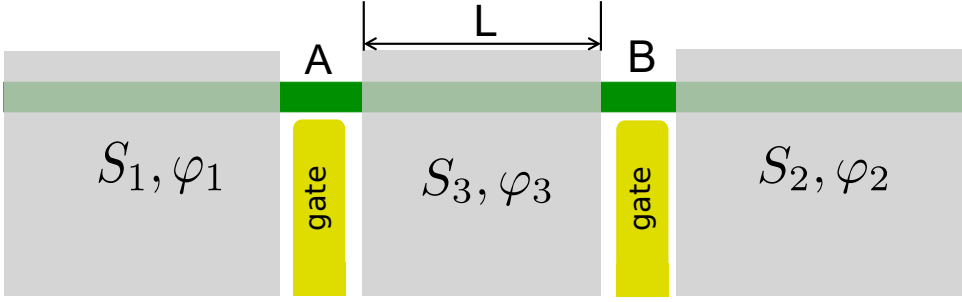


Figure 3.1: The Andreev molecule setup [26] consists of a semiconducting nanowire covered by three superconducting leads with the phases φ_1 , φ_2 , and φ_3 . Two junctions A and B are formed in the nanowire. Their transmissions can be tuned by the nearby gates. The ABS at these junctions can be hybridized depending on the separation L .

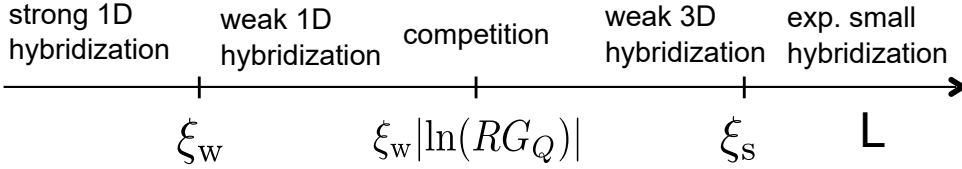


Figure 3.2: The hybridization regimes depending on the junction separation L and the correlation lengths ξ_w, ξ_s in the nanowire and in the lead, respectively. We distinguish strong 1D hybridization, weak 1D hybridization, competition of 1D and 3D hybridization, weak 3D hybridization. The ABS become independent at $L \gg \xi_s$. The 3D case has been considered in Ref. kornich:pr19. In this work, we concentrate on the first three regimes.

further increase of L/ξ_w , the 3D propagation dominates, this being the case described in Ref. [13], see Fig. 3.2. This sequence of regimes implies $\xi_w < \xi_s$, ξ_s being the correlation length in the superconducting lead. The propagation in the lead is naturally diffusive and is characterized by the scattering time τ_s , $\xi_s \approx v_s \sqrt{\tau_s} / \Delta$, v_s being the electron velocity in the superconducting material. If the velocities in the superconducting metal and the superconducting wire were the same, the diffusive propagation would have been slower implying $\xi_w \ll \xi_s$. However, the velocity in the semiconductor is typically two orders of magnitude slower. The condition $\xi_w < \xi_s$ then implies $\tau \Delta < (v_s / v_w) \sqrt{\tau_s} \Delta$. For good contacts between the wire and the superconductor, $\tau \approx 0.2 \Delta$ [18] and the condition holds even for rather dirty superconductors $\tau_s \Delta \ll 10^{-4}$.

We investigate the resulting ABS spectrum in all these regimes. Starting from a simple model of 1D semiconducting spectrum augmented with self-energy describing superconducting proximity effect, we derive scattering matrix formalism that permits to compute and understand the ABS energies in 1D regimes. We extend this formalism to include 3D propagation amplitudes to describe the competition regime. We present the spectra for different L , illustrating the transition from a strong 1D hybridization regime for $L/\xi_w \ll 1$ to the regime with two energy levels with a sizeable splitting at $L/\xi_w \sim 1$, and further to almost independent ABS hybridized at the degeneracy points, for $L/\xi_w \gg 1$. We present the details on how the upper energy level disappears merging with the continuous quasiparticle spectrum upon

decreasing L . We study the effect of quantum interference on the spectrum in various regimes, that is, the oscillatory dependence on the phase accumulated during the electron passage between the junctions. We demonstrate that the energies can be significantly affected by the interference for $L/\xi_w \ll 1$ in the whole range of the phases, while for larger L/ξ_w the interference is pronounced only in the vicinity of the degeneracy points. We provide analytical formulas for this case. We ly address an interesting case of ballistic junctions and discuss its peculiarities with respect to other results. We derive and analyse analytical formulas for the competition regime demonstrating the interference of 1D and two 3D transmission amplitudes. We show that the variances of 3D amplitudes are the same and scale as $\sim G_Q R$. As the 1D transmission amplitudes scale as e^{-L/ξ_w} , the competition regime occurs, when these two scales are of the same order. We derive an analytical formula for the energy splitting due to 3D propagation and compare it to the results of Ref. [13].

Let us explain in detail our motivation to study ABS in this setup in different regimes, as well as outline the significance of the results obtained for interesting device operations. The device provides two discrete ABS, their energies depending on two external parameters - two superconducting phases, and, in addition, on a gate voltage that controls the interference. As such, it can be used as a quantum computation unit, or, more generally, as an element coupled to a microwave field with the frequency matching the energy difference between a pair of quantum states. Such resonant conditions enable high-precision measurement of the energy dependence on the parameters involved. This opens up a variety of applications in quantum sensing and in implementation of feedback schemes.

The setup can be used as a quantum unit utilizing resonant quantum manipulation. Various qubit realizations are possible in the device under consideration. Here we do not speculate which one would be more practical, but just count all of them. A single junction with a single spin-degenerate ABS provides 4 quantum states that differ in fermion occupation numbers $n_\sigma = 0, 1, \sigma$ labelling the spin projection. For each parity of quasiparticle number, we have two states. Thus, there are two ways to make a qubit out of this: either Andreev singlet qubit for even parity [38, 11] or an Andreev spin qubit [4, 11] for odd parity. The double-junction setup under consideration typically encompasses 2 spin-degenerate ABS levels, this provides $4 \times 4 = 16$ quantum states, 8 for each parity. For a single qubit realization, one chooses two states out of 8: this gives 28 possible realizations for each parity. If one of the qubit states is the ground state, which is convenient in some quantum applications, there are 7 possible realizations. There are enough states for a double-qubit realization. Four basis states should be chosen. This gives 70 possible realizations. If one of the basis states is the ground state, 35 realizations are available. The basis states differ in fermion occupation numbers $n_{i,\sigma}$, i and σ labelling the level and the spin, respectively. Their energies are given by:

$$E = \sum_{i,\sigma} E_i(n_{i,\sigma} - 1/2). \quad (3.1)$$

The peculiar features of our results permit various interesting quantum manipulation applications. Without making a complete list, let us shortly mention the most evident ones. In the weak coupling regime, one can realize two singlet qubits corresponding to two junctions. These qubits are conveniently uncoupled in the most of the parameter space. Bringing then to the degeneracy lines makes it possible to arrange two-qubit gates. The pronounced interference effect at the anticrossing makes it possible to operate this gate by a

voltage gate. Another example of an interesting quantum manipulation in the weak coupling regime has been outlined in Ref.[13]. This manipulation makes a swap of a quasiparticle between the junctions. The protocol is to sweep the phases slowly through an avoided level crossing, this prevents Landau-Zener tunnelling, and to get back rapidly. The merging of an ABS state with a continuum upon changing a parameter (one of the phases) is interesting for a realization of a non-unitary quantum gate. It provides a wave function collapse and can be used as a quantum measurement. To see this, let us consider phase setting when there are two ABS, and a quasiparticle that is in the superposition: it is delocalized between the upper and lower level. Changing the setting to the region where only lower level is present makes the wave function to collapse: we have either no quasiparticle or a quasiparticle localized in the lower level. Similar non-unitary operations can be realized for other qubit realizations. The manipulations are performed changing the gate voltages of the gates adjacent to the nanowire and fluxes controlling the superconducting phases. To describe this quantitatively, one needs, in addition to the ABS energies, to compute the off-diagonal elements of the Hamiltonian describing the manipulation. This, as well as a specification of a concrete quantum manipulation scheme, is beyond the scope of this work.

The paper is organized as follows. In Sec. 3.2 we present the details of the setup and the model in use. We consider the wave functions and the spectrum edge for the infinite uniform nanowire and discuss the dependence on the parameter $\tau\Delta$ in Sec. 3.3. The scattering matrix approach is derived and outlined in Sec. 3.4. We summarize and discuss the main results in Sec. 3.5. In Sec. 3.6 we consider the strong 1D hybridization. We develop a perturbation theory suitable in the opposite limit, in Sec. 3.7. The detailed discussion of the interference effect is presented in Sec. 3.8. The transfer between single-band and two-band regimes is detailed in Sec. 3.9. The Sec. 3.10 focuses on the case of the fully transparent junctions. The competition regime is considered in Sec. 3.11. We conclude in Sec. 3.12.

3.2. THE SETUP AND MODEL

Let us detail the Andreev molecule setup (Fig. 3.1). Electrically, this is a three-terminal circuit with two junctions. We assume same superconducting material for all electrodes, so that the superconducting gap is the same for all of them. The spectrum of the bound states will depend on three superconducting phases of the electrodes, φ_1 , φ_2 , and φ_3 . In fact, by virtue of gauge invariance, it depends only on two phase differences $\tilde{\varphi}_1 = \varphi_1 - \varphi_3$, $\tilde{\varphi}_2 = \varphi_1 - \varphi_3$. If the junctions can be regarded as independent, two independent ABS with energies $E_{1,2}(\tilde{\varphi}_{1,2})$ are formed. If the ABS are hybridized, each energy depends on both phase differences. We assume that the wire is sufficiently long in comparison with the electron wavelength, $k_F L \gg 1$.

We describe the electron spectrum in the nanowire with a minimal model. We have to stress that this is not a toy model: it is essentially more elaborated and directly related to the actual nanowires, so we expect the results to be immediately relevant for the experiments.

We assume that the nanowire has a single propagation mode, disregard the spin splitting and concentrate on the states close to the Fermi surface. Since the energies of the ABS are of the order of the proximity-induced gap $\tilde{\Delta}$, this implies sufficiently big Fermi energy $E_F \gg \tilde{\Delta}$. The Hamiltonian with the linearized spectrum is naturally written as a matrix in the basis of right- and left-moving electrons, whose field operators are envelope functions of $\exp(\pm i k_F x)$, $\Psi_\sigma(x) = \exp(i k_F x) \Psi_{R,\sigma}(x) + \exp(-i k_F x) \Psi_{L,\sigma}(x)$, x being an effective coordinate

along the nanowire, σ being spin index. It reads:

$$H_{\text{nw}} = \int dx' dx \sum_{\alpha, \beta=R,L;\sigma} \Psi_{\alpha,\sigma}^\dagger(x') H_{\alpha\beta}^{\text{nw}}(x, x') \Psi_{\beta,\sigma}(x), \quad (3.2)$$

$$\hat{H}^{\text{nw}} = -i\nu_w \frac{\partial}{\partial x} \tau_z + \hat{V}_A(x) + \hat{V}_B(x) \quad (3.3)$$

Here, ν_w is the Fermi velocity, τ_z is a diagonal matrix with $\tau_z^{RR} = -\tau_z^{LL} = 1$. We assume that the wire is ballistic under the electrodes while the electrons are scattered in the junction regions, $\hat{V}_A(x)$ and $\hat{V}_B(x)$ are the matrix potentials responsible for this scattering. In principle, there is no much work to generalize H_{nw} and to include parabolic dispersion, spin-orbit splitting and spin magnetic field [35, 19, 24]. However, in this Chapter, we would like to focus on the phenomenon of hybridization that does not necessarily involve spin, so we keep it simple. The Fermi energy, ν_w and k_F in the nanowire can be changed by the applying voltage to an underlying gate [21]. Importantly, even small changes of this gate voltage can cause significant change of the phase $k_F L$ accumulated by an electron moving between the junctions.

The Hamiltonian describing the j th superconducting lead, where $j = \{1, 2, 3\}$, is convenient to write not specifying the orbital electron states present in a disordered superconductor. We label these states with q , and assume a homogeneous superconducting order parameter $\Delta e^{i\varphi_j}$. In terms of the corresponding creation/annihilation operators $d_{q,\sigma}^\dagger$ and $d_{q,\sigma}$ the Hamiltonian reads as follows:

$$H_j = \sum_q \xi_n d_{q,\sigma}^\dagger d_{q,\sigma} + \Delta e^{-i\varphi_j} d_{q,\uparrow} d_{q,\downarrow} + \Delta e^{i\varphi_j} d_{q,\uparrow}^\dagger d_{q,\downarrow}^\dagger. \quad (3.4)$$

ξ_n being the energies of the orbital states counted from the Fermi energy.

The contact between the nanowire and a lead is of tunneling nature and is described with a tunneling Hamiltonian

$$H_T = \sum_{k,q} t_{k,q} a_{k,\sigma}^\dagger d_{q,\sigma} + t_{k,q}^* d_{q,\sigma}^\dagger a_{k,\sigma}, \quad (3.5)$$

k labeling the normal-electron states in the nanowire, a_k^\dagger and a_k being the creation/annihilation operators in these states. The tunnel coupling $t_{k,q}$ depends on the electron states in both the nanowire and the leads. In the absence of superconductivity, the escape rate from the state k to the lead, $1/\tau_k$ is given by the Fermi Golden Rule

$$\frac{1}{\tau_k} = \frac{2\pi}{\hbar} \sum_q |t_{k,q}|^2 \delta(E_k - \xi_q). \quad (3.6)$$

It is convenient and realistic to assume that this escape rate does not depend on the state, so the quality of the contact between the nanowire and the leads is characterized by a single escape time τ .

Under these circumstances, the tunneling into a lead can be conveniently incorporated into a local self-energy [29, 32] Σ_j , which is a matrix in the basis of right- and left-moving

electrons and holes ($\Psi^{e,R}, \Psi^{h,L}, \Psi^{e,L}, \Psi^{h,R}$)

$$\Sigma_j = \frac{1}{\tau \sqrt{\Delta^2 - E^2}} \begin{pmatrix} -E & \Delta e^{i\varphi_j} & 0 & 0 \\ \Delta e^{-i\varphi_j} & -E & 0 & 0 \\ 0 & 0 & -E & \Delta e^{i\varphi_j} \\ 0 & 0 & \Delta e^{-i\varphi_j} & -E \end{pmatrix}, \quad (3.7)$$

so the resulting equation for the Green's function in the nanowire reads:

$$(E - \mathcal{H}) G(x, x') = -\delta(x - x') \quad (3.8)$$

$$\mathcal{H} = -i \nu_w \eta \frac{\partial}{\partial x} + W_A(x) + W_B(x) + \Sigma(x), \quad (3.9)$$

with

$$\eta = \begin{pmatrix} 1 & 0 & 0 & 0 \\ 0 & -1 & 0 & 0 \\ 0 & 0 & -1 & 0 \\ 0 & 0 & 0 & 1 \end{pmatrix}, \quad (3.10)$$

$$W_A = \begin{pmatrix} V_A^{RR} & 0 & V_A^{RL} & 0 \\ 0 & -V_A^{LL} & 0 & -V_A^{RL} \\ V_A^{LR} & 0 & V_A^{LL} & 0 \\ 0 & -V_A^{LR} & 0 & -V_A^{RR} \end{pmatrix}, \quad (3.11)$$

W_B having the same structure.

3.3. UNIFORM NANOWIRE

In this Section, we will consider the spectrum and the wavefunctions in an infinite and uniform semiconducting nanowire with the proximity-induced gap $\tilde{\Delta} < \Delta$. There are no states at energies below $\tilde{\Delta}$ in a uniform nanowire, there are modes confined in the nanowire at $\tilde{\Delta} < E < \Delta$, and there are extended states in the wire and leads at $E > \Delta$. For a uniform wire, we can regard $\det(E - \mathcal{H})$ as an equation for the wave vector for a given energy. Correspondingly, the wave vector is imaginary at $0 < E < \tilde{\Delta}$, is real in the interval $\tilde{\Delta} < E < \Delta$, and complex otherwise.

Since we will later concentrate on ABS, we concentrate at $E < \tilde{\Delta}$. The imaginary part of the wave vector gives an energy-dependent inverse localization length ξ_w^{-1} :

$$\nu_w \tau \xi_w^{-1} = \sqrt{1 - E^2 \tau^2 - \frac{2E^2 \tau}{\sqrt{\Delta^2 - E^2}}}. \quad (3.12)$$

The condition $\xi_w^{-1}(E) = 0$ eventually defines the gap $\tilde{\Delta}$. It is given by an implicit relation

$$\tau \Delta = \frac{\Delta}{\tilde{\Delta}} \sqrt{\frac{\Delta - \tilde{\Delta}}{\Delta + \tilde{\Delta}}}. \quad (3.13)$$

and is plotted in Fig. 3.3 (a) as a function of $(\tau \Delta)^{-1}$. Short τ implies a good contact, so $\tilde{\Delta} \approx \Delta$ at $\tau \Delta \ll 1$. In the opposite limit, $\tilde{\Delta} \approx 1/\tau \ll \Delta$. In Fig. 3.3 (b) we plot the inverse

correlation length versus energy normalized by the proximity gap $\tilde{\Delta}$, for various $\tau\Delta$. We see that for any value of this parameter the correlation length is close to the escape length $\nu_w\tau$. For a bad contact, $\nu_w\tau\xi_w^{-1} = \sqrt{1 - (E/\tilde{\Delta})^2}$, for a good contact $\xi_w = \nu_w\tau$ for all energies except the vicinity of the gap edge.

There are four eigenfunctions at each energy, corresponding to right- or left-moving electrons and the exponent decreasing either to the left or to the right,

$$\begin{pmatrix} \Psi^{e,R} \\ \Psi^{h,L} \end{pmatrix} = \begin{pmatrix} 1 \\ e^{i(\mp\chi-\varphi)} \end{pmatrix} e^{\mp x/\xi_w}, \quad (3.14)$$

$$\begin{pmatrix} \Psi^{e,L} \\ \Psi^{h,R} \end{pmatrix} = \begin{pmatrix} 1 \\ e^{i(\pm\chi-\varphi)} \end{pmatrix} e^{\mp x/\xi_w}. \quad (3.15)$$

Here, we introduce an important phase χ associated with the phase of Andreev reflection from a corresponding piece of the nanowire,

$$\chi = \arcsin \sqrt{1 - \left[\frac{E(1 + \tau\sqrt{\Delta^2 - E^2})}{\Delta} \right]^2} \quad (3.16)$$

in the interval $0 < E < \tilde{\Delta}$. As we will see, the ABS energies are determined from the energy dependence of χ . At any value of $\tau\Delta$, $\chi(0) = \pi/2$, $\chi(\tilde{\Delta}) = 0$. It is interesting to note that $\chi(E/\tilde{\Delta})$ exhibits very little dependence on $\tau\Delta$. This is seen in Fig. 3.3 (c) where all the curves corresponding to different $\tau\Delta$ collapse into one. This is why the ABS spectrum is hardly sensitive to $\tau\Delta$, and we do not have to explore its dependence on this parameter.

3.4. SCATTERING APPROACH

To avoid describing the details of the junctions and the corresponding potentials in their vicinity, we implement the scattering approach for the problem under consideration. The scattering approach to the setup was first implemented in Refs. [26, 25] at lesser detail level, and recently elaborated in Ref. [27]. Their results are qualitatively the same. A scattering matrix, by definition, is a matrix that relates the outgoing wave amplitudes to incoming ones. In the setup under consideration, there are two junctions, A and B (see Fig. 3.1). We assume that the junction region is shorter than ξ_w , this assumption permits to neglect possible Andreev scattering in the junctions as well as the energy dependence of the scattering amplitudes at the energy scale $\simeq \tilde{\Delta}$. If we regard the junction A as a scattering region, the incoming electron wave amplitudes are $\{\Phi_1^{e,R}, \Phi_3^{e,L}\}$ and the outgoing ones are $\{\Phi_1^{e,L}, \Phi_3^{e,R}\}$, where 1,3 refer to the leads adjacent to the junction A , and the amplitudes correspond to the wave functions on the side of a lead. The electron scattering matrix for the junction A in this basis is

$$S_A^e = \begin{pmatrix} r_A e^{-i\theta_1^A} & t_A e^{-i\frac{\theta_1^A + \theta_3^A}{2}} \\ t_A e^{-i\frac{\theta_1^A + \theta_3^A}{2}} & -r_A e^{-i\theta_3^A} \end{pmatrix}. \quad (3.17)$$

Here, real r_A and t_A , $r_A^2 + t_A^2 = 1$, denote reflection and transmission amplitudes, $\theta_{1,3}^A$ are the corresponding reflection phases. The electron scattering matrix for junction B , S_B^e , is

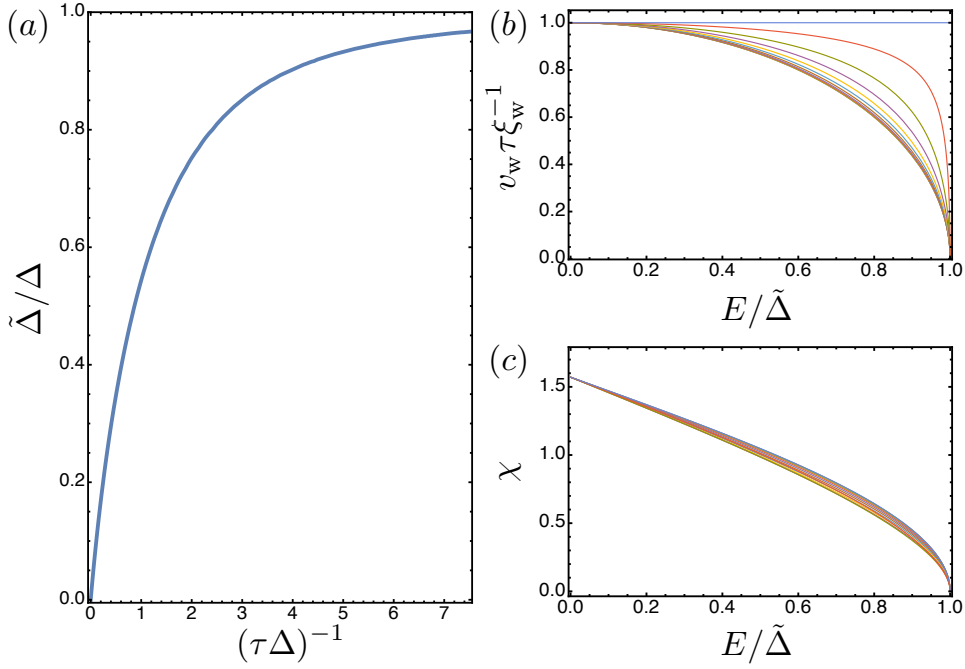


Figure 3.3: (a) The relative proximity gap $\tilde{\Delta}/\Delta$ versus the parameter $(\tau\Delta)^{-1}$ characterizing the quality of the tunnel contact between the nanowire and the superconducting lead. For a good contact, $\tau \rightarrow 0$, $\tilde{\Delta} \rightarrow \Delta$. (b) The inverse correlation length $\xi_w(E)$ versus energy for different values of $\tau\Delta$. (c) The Andreev reflection phase χ versus energy. In both plots, the values of the parameter for different curves correspond to $\tilde{\Delta}/\Delta = \{0, 0.1, 0.2, 0.3, \dots, 0.9, 0.98, 1\}$.

defined in a similar basis: the incoming amplitudes are $\{\Phi_4^{e,R}, \Phi_2^{e,L}\}$ and outgoing ones are $\{\Phi_4^{e,L}, \Phi_2^{e,R}\}$, where 4 refers to the wave functions in the lead 3 close to the junction B . The matrix reads:

$$S_B^e = \begin{pmatrix} r_B e^{-i\theta_3^B} & t_B e^{-i\frac{\theta_3^B + \theta_2^B}{2}} \\ t_B e^{-i\frac{\theta_3^B + \theta_2^B}{2}} & -r_B e^{-i\theta_2^B} \end{pmatrix}. \quad (3.18)$$

The scattering matrix for holes is obtained from the electron one via complex conjugation. Thus, the total scattering matrix describing the scattering from the junctions, S_{NS} , relates the incoming amplitudes $\Phi_+ = \{\Phi_1^{e,R}, \Phi_3^{e,L}, \Phi_1^{h,R}, \Phi_3^{h,L}, \Phi_4^{e,R}, \Phi_2^{e,L}, \Phi_4^{h,R}, \Phi_2^{h,L}\}$ to the outgoing ones $\Phi_- = \{\Phi_1^{e,L}, \Phi_3^{e,R}, \Phi_1^{h,L}, \Phi_3^{h,R}, \Phi_4^{e,L}, \Phi_2^{e,R}, \Phi_4^{h,L}, \Phi_2^{h,R}\}$, and has a block-diagonal form

$$S_{NS} = \begin{pmatrix} S_A^e & 0 & 0 & 0 \\ 0 & S_A^h & 0 & 0 \\ 0 & 0 & S_B^e & 0 \\ 0 & 0 & 0 & S_B^h \end{pmatrix}. \quad (3.19)$$

The subscript "NS" here stands for "normal scattering". Since the junctions are short, no Andreev scattering mixing electrons and holes occur there. The matrix therefore is in blocks, for electrons and holes. Andreev scattering occurs in the wire regions covered by superconducting leads and is described by Andreev scattering matrix S_{AS} . The outgoing wave amplitudes for S_{NS} are incoming wave amplitudes for S_{AS} and vice versa. This gives $\Phi_- = S_{AS}\Phi_+$, and the matrix S_{AS} is derived from the matching of the wavefunctions (3.14). It reads:

$$S_{AS} = \begin{pmatrix} 0 & 0 & r_1^{eh} & 0 & 0 & 0 & 0 & 0 \\ 0 & 0 & 0 & r_3^{eh} & t_R^e & 0 & 0 & 0 \\ r_1^{he} & 0 & 0 & 0 & 0 & 0 & 0 & 0 \\ 0 & r_3^{he} & 0 & 0 & 0 & 0 & t_R^h & 0 \\ 0 & t_L^e & 0 & 0 & 0 & 0 & r_4^{eh} & 0 \\ 0 & 0 & 0 & 0 & 0 & 0 & 0 & r_2^{eh} \\ 0 & 0 & 0 & t_L^h & r_4^{he} & 0 & 0 & 0 \\ 0 & 0 & 0 & 0 & 0 & r_2^{he} & 0 & 0 \end{pmatrix}, \quad (3.20)$$

with

$$r_{1,2}^{eh,he} = e^{i(\pm\varphi_{1,2} + \chi)}, \quad (3.21)$$

$$r_3^{eh,he} = r_4^{eh,he} = e^{i(\pm\varphi_3 + \chi)} r_3, \quad (3.22)$$

$$r_3 = \frac{1 - e^{-2L/\xi_w}}{1 - e^{2i\chi} e^{-2L/\xi_w}}, \quad (3.23)$$

$$t_R^{e,h} = t_L^{e,h} = e^{\pm i k_F L} t, \quad (3.24)$$

$$t = \frac{(1 - e^{2i\chi}) e^{-L/\xi_w}}{1 - e^{2i\chi} e^{-2L/\xi_w}}, \quad (3.25)$$

$$|t|^2 + |r_3|^2 = 1. \quad (3.26)$$

The notations eh and he imply the electron conversion into a hole and vice versa. The transmission amplitudes $t_{R,L}^{e,h}$ do not involve a conversion and correspond to electron or hole propagation through the part of the nanowire under the third lead. The phases $\pm k_F L$ acquired in the course of propagation are manifested in the quantum interference effect, as we will show later. For a small separation between the junctions, $L/\xi_w \ll 1$, $r_3 \rightarrow 0$ and $|t| \rightarrow 1$. This implies that the electrons or holes do not exhibit Andreev reflection directly passing to another junction. In the opposite limit, $L/\xi_w \gg 1$, $|r_3| = 1$, and $|t| = 0$. The scattering matrix is separated into blocks indicating the separation of ABS formed at the two junctions are completely separate from each other.

Since $\Phi_- = S_{AS}\Phi_+$ and $\Phi_+ = S_{NS}\Phi_-$ an ABS is formed provided $S_{NS}S_{AS}$ has a unit eigenvalue. This gives an equation that is satisfied at an energy corresponding to an ABS energy,

$$\det\{(1 - S_{NS}S_{AS})\} = 0. \quad (3.27)$$

In this work, we solve this equation numerically and analytically for various cases.

3.5. OVERVIEW OF THE ABS SPECTRUM

In this Section, we discuss the propagation processes in the setup, relate those to the features of the spectrum, and give an overview of the concrete results. To start with, we shall note that the hybridization of ABS states formed at two junctions requires either electron or hole propagation between the junctions. This is evident from the scattering approach where the scattering matrix is separated into the blocks for each junction unless there are non-zero transmission amplitudes $t_{R,L}^{e,h}$. This propagation may naturally take place in 1D wire, or involve an escape to the 3D lead with a subsequent return to the wire.

In the strong 1D hybridization regime $L \ll \xi_w$ the propagation between the junctions is unobstructed by anything, even by Andreev reflection, since the propagation time is too short for a particle to feel the induced gap in the nanowire. As the result, the third electrode has no effect on the ABS, and we have a compound junction between A and B that supports a single ABS. We show this explicitly and analytically in Sec. 3.6. In the opposite limit $L \gg \xi_w$ of the weak 1D hybridization the direct propagation is strongly reduced by Andreev reflection in the wire: an electron/hole is turned back as a hole/electron. There are two independent ABS and hybridization is only important in the vicinity of degeneracy points where two energies cross. We develop a perturbation theory valid for a small direct transmission amplitude (Sec. 3.7) that provides an analytical expression for this splitting for general scattering matrices.

The crossover between the regimes is not trivial since the number of ABS in two limits are different. We illustrate the crossover by numerical calculations presented in Fig. 3.4. In the Figure, we plot the ABS spectrum versus the phase of the third lead, φ_3 , at various separations between the junctions and for representative choice of the junction scattering matrices. In Fig. 3.4 (a) that corresponds to a small separation and strong 1D hybridization regime, we observe a single ABS with no φ_3 dependence. The second ABS emerges from continuous spectrum at larger separations (Fig. 3.4 (b)), and the energies get closer to each other upon increasing L (Fig. 3.4 (c)). Deep in the weak 1D hybridization regime, the ABS energies correspond to independent junction states with virtually invisible anticrossings (Fig. 3.4 (d)). The emergence of the second ABS from the continuum is of interest and is

investigated in Sec. 3.9.

A clear idealized case is where the propagation in the junctions is ballistic like in the covered sections of the nanowire. In principle, this can be realized in sufficiently pure nanowires. This case is characterized by the absence of quantum interference involving the phase $k_F L$ since the electrons or holes are never reflected, and zero-energy crossings of ABS. It is detailed in Sec. 3.10.

In general, the junctions are not transparent, that is, $t_{A,B} \neq 1$, the electrons and holes propagating between the junctions may reflect from those and bounce in the piece of the nanowire covered by the third lead. The bounces result in the quantum interference pattern involving the phase $k_F L$. This pattern can be observed experimentally by changing k_F slightly with a back gate. We discuss and illustrate the interference in Sec. 3.8. It is clearly visible in both 1D regimes.

If the 1D propagation amplitudes become sufficiently small, $\approx G_Q R$, we enter the competition regime (Fig. 3.2). To describe this, we extend the perturbation theory of Sec. 3.7 to include the 3D propagation amplitudes next to the 1D propagation amplitudes. This analysis is rather involved since 3D propagation also encompasses the electron-hole and hole-electron conversion, and is detailed in Sec. 3.11. We will show that the result can be regarded as interference of 2 independent 3D amplitudes affected by mesoscopic fluctuations in the lead and a single 1D amplitude affected by the phase $k_F L$. To describe the 3D amplitudes, we refine the semiclassical approach suggested in Ref. [13] and eventually correct an error in that reference.

3.6. STRONG 1D HYBRIDIZATION

In this Section, we consider the limit $L \ll \nu_w \tau, \xi_w$, when electrons do not exhibit Andreev reflection in the piece of the nanowire covered by the third lead. For the scattering amplitudes defined in Eqs. (3.21)-(3.25) this implies $r_3 \rightarrow 0$, $t \rightarrow 1$. Solving the Eq. (3.27) in this limit, we obtain an equation for the ABS energy,

$$\sin^2 \chi = T_s \sin^2 \left[\frac{\varphi_1 - \varphi_2}{2} \right]. \quad (3.28)$$

Here, T_s is in fact the transmission coefficient of the normal scattering in a compound junction obtained by putting the junctions A and B in series. It is given by the usual expression (see, e.g. Ref. [22])

$$T_s = \frac{t_A^2 t_B^2}{1 + r_A^2 r_B^2 + 2r_A r_B \cos \theta}, \quad (3.29)$$

where $\theta \equiv \theta_3^A + \theta_3^B - 2k_F L$. As a rather trivial interference effect, it involves the phase accumulated in the course of round trip between the junctions.

As mentioned in the Section 3.3, the dependence of χ on the parameter $\tau \Delta$ is insignificant if normalized on the proximity gap $\tilde{\Delta}$. So we can approximate $\sin \chi \approx \sqrt{1 - (E/\tilde{\Delta})^2}$. This reproduces a standard relation for an ABS in a one-channel junction between two leads [22]:

$$E_{\text{ABS}} = \tilde{\Delta} \sqrt{1 - T_s \sin^2 \left[\frac{\varphi_1 - \varphi_2}{2} \right]}. \quad (3.30)$$

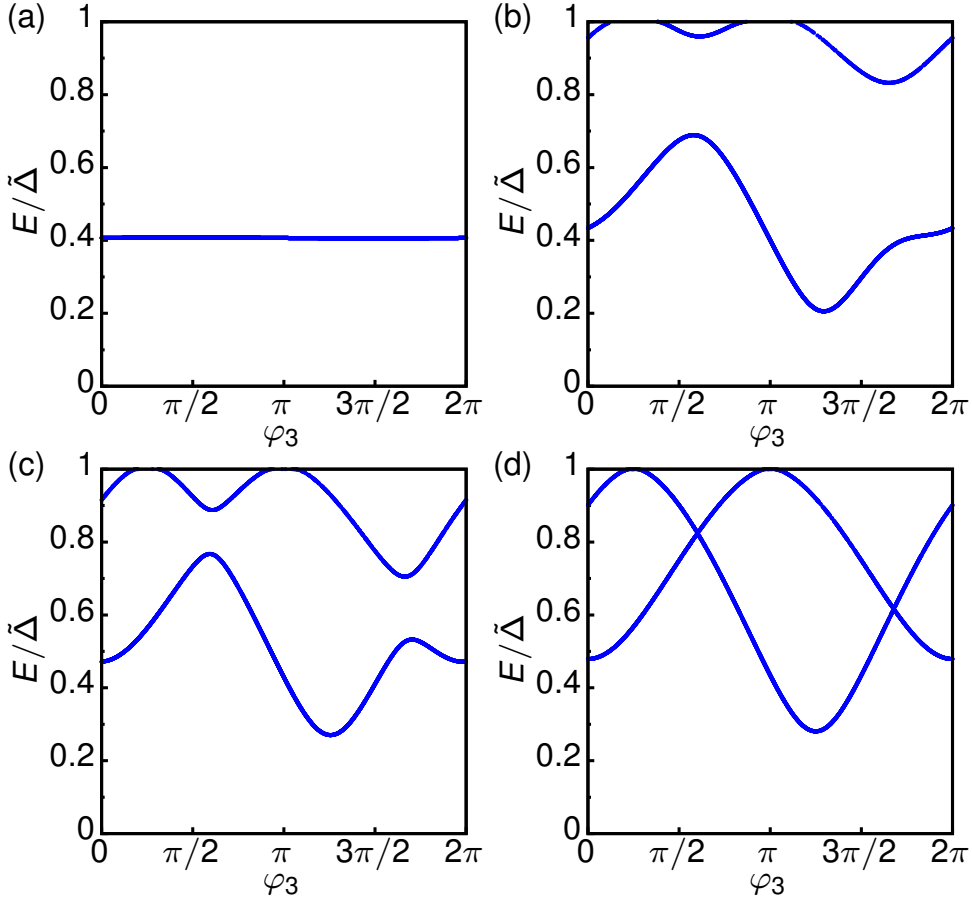


Figure 3.4: The overview of the ABS spectrum. The ABS energies are plotted versus the phase of the third lead φ_3 for different separations L . For all plots, $t_A = 0.85$, $t_B = 0.95$, $\theta_1^A = \theta_3^B = 0$, and $\theta_3^A = \theta_2^B = -\pi$, $\tau\Delta = 0.2$, $\varphi_1 = \pi$, $\varphi_2 = \pi/4$. (a) $L/(v_W\tau) = 0.1$. The strong 1D hybridization regime: a single ABS in both junctions hardly depending on φ_3 . (b) $L/(v_W\tau) = 1$. The crossover between the regimes. The second ABS emerges from the continuous spectrum. It remains close to the band edge. (c) $L/(v_W\tau) = 2$. The system tends towards the formation of two independent ABS. The energy splitting at anticrossings is still comparable with $\tilde{\Delta}$. (d) $L/(v_W\tau) = 6$. The weak 1D hybridization regime. Two ABS are almost independent, the energy splitting near degeneracy points is almost invisible.

3.7. WEAK 1D HYBRIDIZATION: PERTURBATION THEORY

Let us turn to the opposite limit $L/\xi_w \gg 1$. In this weak 1D hybridization regime, the transmission amplitude t is small, eventually, exponentially small, $t = (1 - e^{2i\chi})e^{-L/\xi_w}$. We will develop a perturbation theory for the ABS energies in terms of t . We restrict ourselves to the most important situation of the vicinity of the degeneracy points, where the energies of two ABS formed at the junctions A and B , almost coincide. The perturbation lifts the degeneracy resulting in the anticrossing of two energy levels. The energy splitting at the anticrossing δE is much smaller than $\tilde{\Delta}$, $\delta E \simeq |t|\tilde{\Delta}$.

The derivation is as follows. In the limit $t = 0$ the scattering matrix $S_{NS}S_{AS}$ is separated into two independent 4×4 blocks corresponding to the junctions A and B . We examine the eigenvectors of the blocks and pick up one corresponding to the eigenvalue 1 at certain energy, that is, to the ABS energy. The perturbation enters an off-diagonal 4×4 block. We project this block on the eigenvectors $|A\rangle$ and $|B\rangle$ found for the A and B blocks. We take the derivative of the diagonal blocks A and B with respect to energy. With this, we obtain an effective 2×2 Hamiltonian to describe the anticrossing region,

$$H_{\text{eff}} = E_0 + \begin{pmatrix} \delta E_A & \mathcal{M} \\ \mathcal{M}^* & \delta E_B \end{pmatrix}, \quad (3.31)$$

where E_0 is the energy at the degeneracy point, $\delta E_{A,B}$ are small deviations from the degeneracy in zeroth order in $|t|$, and $\mathcal{M} \propto t$ is the non-diagonal matrix element representing the perturbation. This element contains the expressions for the 4-eigenvectors that are rather clumsy. In the most compact form, it can be expressed using the notations

$$\sqrt{2}u_{A,B}^{\pm} = \sqrt{1 \pm \text{sgn}\tilde{\varphi}_{1,2}} \sqrt{1 - \frac{r_{A,B}^2}{\cos^2 \chi_0}}, \quad (3.32)$$

$(u_{A,B}^+)^2 + (u_{A,B}^-)^2 = 1$, u^{\pm} are related to electron and hole amplitudes in the third lead. The matrix element is defined upon an arbitrary phase factor and reads

$$\mathcal{M} = \frac{e^{-L/\xi_w} \sin \chi_0}{\chi'(E_0)} \left[u_B^- u_A^+ e^{-i\theta/2} - u_A^- u_B^+ e^{i\theta/2} \right], \quad (3.33)$$

where $\chi'(E_0) = \partial \chi / \partial E|_{E=E_0}$, $\chi_0 = \chi(E_0)$.

The matrix element is thus contributed by two amplitudes corresponding to the right- and left-moving electrons. If the junctions are ballistic, only one of these amplitudes survives depending on the $\text{sgn}\tilde{\varphi}_1$ ($\text{sgn}\tilde{\varphi}_2 = -\text{sgn}\tilde{\varphi}_1$ in the anticrossing). This case is further detailed in Sec. 3.10.

The energy splitting then assumes the form

$$\delta E^2 = 4|\mathcal{M}|^2 = C((u_A^+ u_B^-)^2 + (u_A^- u_B^+)^2 - 2u_A^- u_A^+ u_B^- u_B^+ \cos \theta), \quad (3.34)$$

where

$$C = \frac{4e^{-2L/\xi_w} \sin^2 \chi_0}{(\chi'(E_0))^2}. \quad (3.35)$$

If we implement the heuristic approximation we made for $\chi(E)$, $C = 4(\tilde{\Delta} - E^2/\tilde{\Delta})^2 e^{-2L/\xi_w}$.

The Eq. (3.34) makes explicit the interference pattern that is periodic in θ . Moreover, both amplitudes become equal in modulus and the energy splitting vanishes at $\theta = 0$ provided the junctions have the same transmission coefficients and $\text{sgn}\tilde{\varphi}_1 = \text{sgn}\tilde{\varphi}_2$.

3.8. INTERFERENCE AT $L \simeq \xi_w$

In both regimes of strong and weak 1D hybridization, we have seen a significant interference effect, Eqs. (3.29), (3.34). However, in the strong hybridization regime the effect was confined to the ABS energies not depending on the phase of the third lead, while in the weak hybridization regime it was visible in the vicinity of the degeneracy points only. This motivates us to explore the effect at the intermediate values of $L \simeq \xi_w$. The numerical results obtained are presented in Fig. 3.5. The subplots are computed at increasing values of L . In each subplot, the different curves correspond to different values of the phase $k_F L$.

As we see, the significant interference effect is compatible with φ_3 -dependence of the curves, that is, with significant probability of Andreev reflection between the junctions. However, the magnitude of interference gradually reduces upon increasing L and becomes confined to anticrossing regions at $L \simeq 3\nu_w\tau$.

In Fig. 3.6 we present the zoom on the vicinity of the degeneracy point, this makes the strong interference effect evident. For this parameter choice, the spectrum in the zoom window is described by the perturbation Hamiltonian (3.31) with the accuracy of 3 significant digits.

3.9. UPPER ABS MERGING WITH THE CONTINUUM

Generally, an upper ABS that persist in a multi-terminal system at certain phase settings, may disappear merging with the continuous spectrum. In a general context, this situation has been thoroughly investigated in Ref. [37]. For our three-terminal setup with no appreciable spin-orbit interaction, this consideration predicts the gap edge touching (GET) curves in the two-dimensional space of the phases $\tilde{\varphi}_1, \tilde{\varphi}_2$. The merging occurs at these curves.

Our setup provides a natural cause for such merging since we expect a single ABS in the strong 1D hybridization regime and two ABS in the weak 1D hybridization regime. The upper band should therefore go to the continuum upon decreasing the separation L . We investigate this in detail in this Section.

It turns out that the upper ABS is present in the structure at any settings of L and junction scattering matrices. The region in the space $(\tilde{\varphi}_1, \tilde{\varphi}_2)$ where both states are present, fills almost the entire space in the weak hybridization regime and shrinks to a line in the strong hybridization regime. Thus the upper state in the strong hybridization regime is present only on this line.

This is illustrated in Fig. 3.7(a) where we plot the GET curves for various L in an elementary cell $(0,0), (2\pi, 2\pi)$ (The overall spectrum is periodic in both phases with the period 2π). The curves are symmetric with respect to $\tilde{\varphi}_1 = \tilde{\varphi}_2$ line. At vanishing L , the curves converge to the line. It is easy to understand why. Since the third lead is irrelevant, there is a zero phase difference at this line for the resulting 2-terminal junction. It is known to be a GET point for a two-terminal junctions [22]. Upon increasing L , the curves move apart bounding a region where the upper ABS is present. Already at $L/(\nu_w\tau) = 1$, this

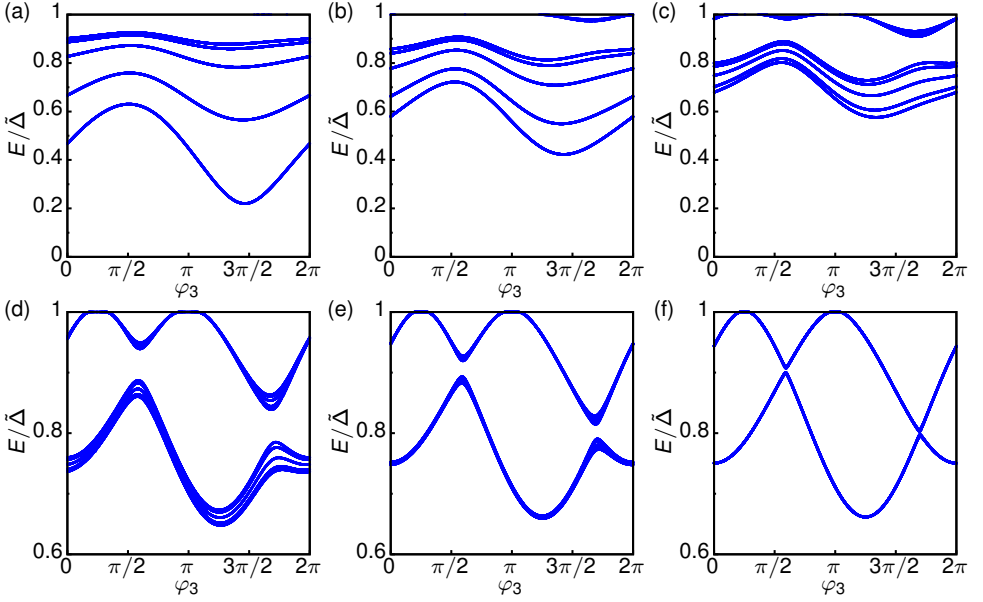


Figure 3.5: The overview of the interference effect. The ABS energies at different settings of the phase $k_F L$ versus the phase of the third lead φ_3 . The values of the separation for the subplots are: $L/(v_w \tau) =$ (a) 0.25, (b) 0.50, (c) 1.00, (d) 2.00, (e) 3.00, (f) 5.00. In each subplot, the accumulated phase takes the value $k_F L \bmod \pi = \{0, 1, 2, 3, 4\}\pi/8$, and the curves move upwards upon increasing the phase. For all the plots $t_A = 0.6$, $t_B = 0.7$, $\theta_1^A = \theta_3^B = 0$, $\theta_3^A = \theta_2^B = -\pi$, $\tau\Delta = 0.2$, $\varphi_1 = \pi$, $\varphi_2 = \pi/4$. (a) The strong 1D hybridization regime. A single ABS persists in the system. Its energy is related to the transmission coefficient of the effective junction, the transmission coefficient depends on interference. (b) The second ABS appears, the interference effect is still strong over the whole range of φ_3 . (c)-(e) The effect is gradually confined to the anticrossing regions. (f) The weak 1D hybridization regime, the energy splitting near degeneracy points is not visible although is still affected by the interference.

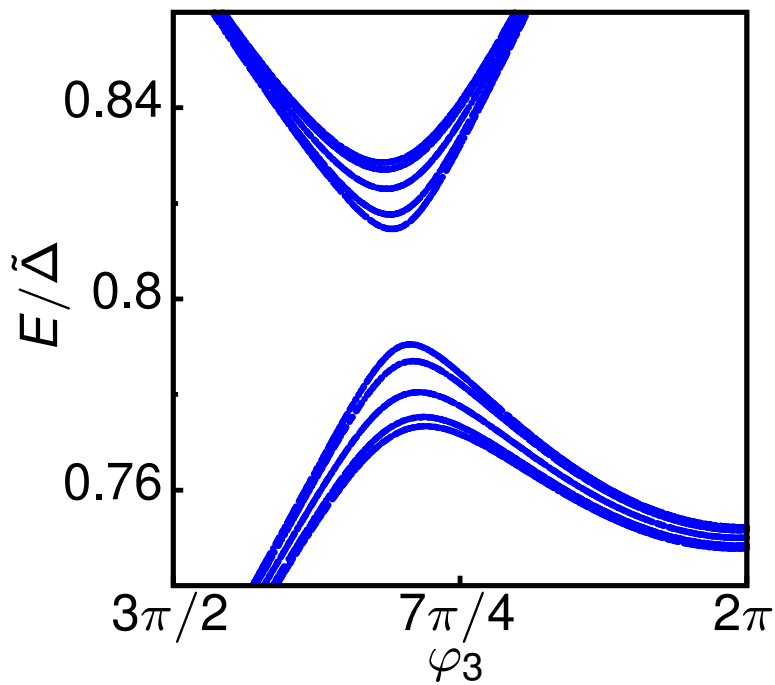


Figure 3.6: A zoom of an anticrossing region in Fig. 3.5 (c). The energies are computed numerically and coincide with the perturbation theory results of Sec. 3.7 in three significant digits.

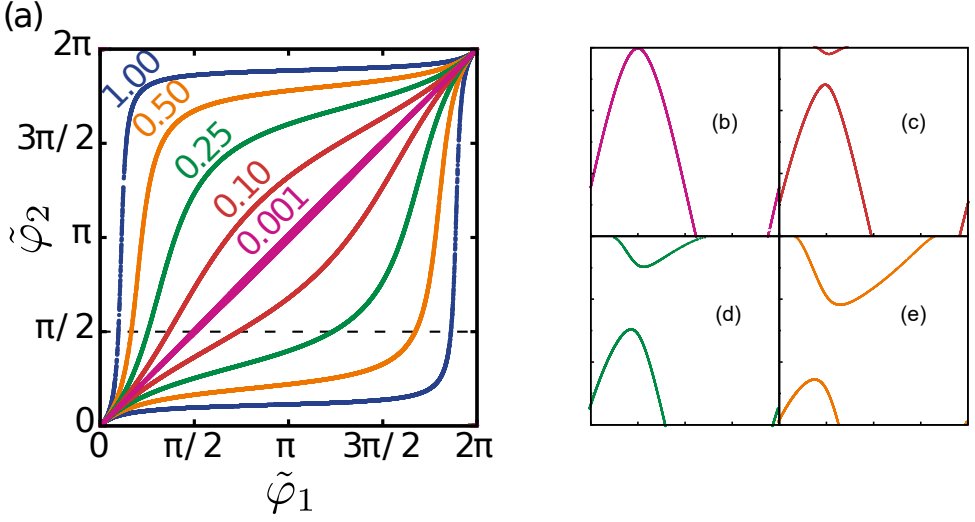


Figure 3.7: Gap edge touching by the upper ABS. (a) The GET curves in the plane $(\tilde{\varphi}_1, \tilde{\varphi}_2)$ for different separations $L/(v_W\tau)$ given in the labels. The fixed parameters are: $t_A = 0.85$, $t_B = 0.95$, $\tau\Delta = 0.2$, $v_F/(L\Delta) = 1$, $\varphi_3 = 0$, $\theta_1^A = \theta_3^B = 0$, $\theta_3^A = \theta_2^B = -\pi$, and $k_F L = \pi/4$. (b)-(e) The ABS energies at $\tilde{\varphi}_2 = \pi/4$ (dashed line in (a)) illustrate the merging of the upper ABS with the continuous spectrum. The values of the separation go through $L/(v_W\tau) = \{0.001, 0.1, 0.25, 0.5\}$ from (b) to (e). For all plots, the vertical axis is $E/\tilde{\Delta}$ ranging from 0.7 to 1, the horizontal axis is $\tilde{\varphi}_1$ ranging from 0 to 2π .

region fills the elementary cell almost entirely. Upon further increase, the GET curves are pressed to the boundaries of the elementary cell where either $\tilde{\varphi}_1 = 0$ or $\tilde{\varphi}_2 = 0$. Indeed, in this limit we have two independent two-terminal junctions, and this defines the positions of their GET points.

It is interesting and instructive to look at the spectrum of both ABS. It is plotted in Figs. 3.7 (b)-(e) along the line $\tilde{\varphi}_1 = \pi/2$. The subfigures correspond to different settings of L . The Fig. 3.7 (b) corresponding to the smallest L represents the *lowermost* ABS and seems to touch the edge at $\tilde{\varphi}_1 = \tilde{\varphi}_2$. However, it only seems. In fact, there is a tiny region near this point where the upper ABS is present, and it is separated in energy from the lowermost one. This structure becomes apparent upon increase of L (see Figs. 3.7 (c)-(e)).

3.10. BALLISTIC JUNCTIONS

In this Section we concentrate on the special case of ballistic junctions, implying no normal reflection in the regions A, B : $r_A = r_B = 0$. The spectrum separates into two parts: for right-moving electrons and left-moving holes, and for left-moving electrons and right-moving holes, that are obtained from each other by exchange of the electrons and holes. An energy level at E in one part corresponds to the energy level at $-E$ in another part by virtue of Bogoliubov-de Gennes symmetry. Correspondingly, the Eq. (3.27) splits into two parts.

The part for right-moving electrons and left-moving holes reads

$$\begin{aligned} & \left[e^{-i(2\chi - \tilde{\varphi}_1)} - \kappa(e^{i\tilde{\varphi}_1} - 1) - 1 \right] \times \\ & \left[e^{-i(2\chi + \tilde{\varphi}_2)} - \kappa(e^{-i\tilde{\varphi}_2} - 1) - 1 \right] \\ & = -4\kappa \sin^2 \chi. \end{aligned} \quad (3.36)$$

Here, $\kappa \equiv \exp(-2L/\xi_w)$. This equation is to be solved for χ and then energy for any given $\tilde{\varphi}_{1,2}$.

To understand the qualitative characteristics of the spectrum, let us consider the weak hybridization regime $\kappa \rightarrow 0$. In zeroth order approximation, two first brackets give rise to two solutions $\chi = \tilde{\varphi}_1/2$ and $\chi = \pi - \tilde{\varphi}_2/2$. Under heuristic approximation discussed, this gives rise to two ABS energies $E = \tilde{\Delta} \cos(\tilde{\varphi}_1/2)$ and $E = -\tilde{\Delta} \cos(\tilde{\varphi}_2/2)$ for the states localized at the junctions A and B , respectively. The energies of the states cross zero at $\tilde{\varphi}_{1,2} = \pi$, which is a known peculiarity of the completely ballistic two-terminal junction [22]. The small κ is relevant at the degeneracy line $\tilde{\varphi}_1 + \tilde{\varphi}_2 = 2\pi$ and especially near the point $\tilde{\varphi}_1 = \tilde{\varphi}_2 = \pi$ where the degeneracy occurs at zero energy. We expand all the phases in the vicinity of this point, $\chi = \pi/2 + E\chi'(0)$, $\tilde{\varphi}_{1,2} = \pi + \delta\varphi_{1,2}$. With this, the equation reduces to

$$(2E\chi'(0) - \delta\varphi_1)(2E\chi'(0) + \delta\varphi_2) = 4\kappa. \quad (3.37)$$

In the limit $L \rightarrow \infty$ this equation decouples into two brackets, each corresponding to junctions A and B . Assuming, L is large, but finite, we obtain

$$E\chi'(0) = \frac{1}{4} \left[\delta\varphi_1 - \delta\varphi_2 \pm \sqrt{(\delta\varphi_1 + \delta\varphi_2)^2 + 16\kappa} \right]. \quad (3.38)$$

We see that the finite hybridization removes the degeneracy at $\delta\varphi_2 = -\delta\varphi_1$. However, it does not remove the zero energy crossings. Those are just shifted to a hyperbola $\delta\varphi_1\delta\varphi_2 + 4\kappa = 0$.

To get an overview of the spectrum for the whole range of L , we plot the energies of ABS along the symmetry line $\tilde{\varphi}_1 = \tilde{\varphi}_2$ (Fig. 3.8, left column) and in the perpendicular direction $\tilde{\varphi}_1 = -\tilde{\varphi}_2$. Along both lines, there is a convenient opportunity to make implicit plots expressing the phases through the energy.

At the symmetry line, the ABS is double-degenerate: the states for right- and left-moving electrons have the same energy. In the weak 1D hybridization regime (Fig. 3.8(a)), the phase dependence approaches that of independent junctions. However, in accordance with Eq. (3.38), the zero-energy crossing is shifted from the symmetry line even for small κ . Upon decreasing L , (Figs. 3.8(b)-(d)), the energy raises approaching the gap edge, this is in accordance with the limit of a single compound junction.

For the plots in the perpendicular direction, the curves of blue (red) color correspond to right- (left-)moving electrons. We see the energy crossings that is a hallmark of the ballistic junction case. The positions of the crossing gradually shift from $\pm\pi$ at big separations to $\pm\pi/2$ at small separations in accordance with the limits of independent junctions and a single compound junction.

We remind that there is no interference effect on ABS since there is no normal scattering at the junctions. The plots along the lines $\tilde{\varphi}_1 = \pm\tilde{\varphi}_2$ do not visually resemble those in Fig. 3.4 which may lead to the idea that the spectra are very different. To prevent this, we replot the ABS for ballistic case in Fig. 3.9 for the same parameters except setting $r_A = r_B = 0$. The resulting plots do resemble those in Fig. 3.4, zero-energy crossings being the only qualitative difference.

3.11. COMPETITION BETWEEN 1D AND 3D PROPAGATION

In this Section, we consider the competition of 1D and 3D electron propagation as seen in the hybridization of the ABS in the Andreev molecule setup under consideration. As we have seen, the 1D propagation amplitudes $t_{R,L}^{e,h}$ between the junctions formally become exponentially small. However, this should not immediately imply the exponentially small hybridization. As estimated in Ref. kornich:pr19, the 3D propagation amplitudes are of the order of $\sqrt{RG_Q}$, R being a resistance characterizing the lead, and thus are not exponentially small provided the separation $L \lesssim \xi_s$.

A full and simultaneous account for 1D and 3D propagation seems a formidable task. In principle, it can be achieved by a non-local extension of the self-energy in Eq. (3.7): $\Sigma(x) \rightarrow \Sigma(x, x')$. However, such self-energy cannot be conveniently averaged over the disorder in the superconducting lead without cancelling the effect, which makes it hardly computable. A solution could be brute-force numerical computation of the Green's function for an atomic-level lattice model. However, such numerical exercises are seldom conclusive in practice, in view of long computation times and arbitrary modelling.

We proceed with a different method which may seem heuristic, but, in fact, is completely adequate to the problem in hand. To explain it, let us formulate a problem in terms of scattering matrix for the junctions. Whatever the propagation, it can be incorporated into (electron and hole) transmission amplitudes between the junctions. Let us note that the competition occurs for small amplitudes where a perturbation theory is applicable. In this case, the amplitudes can be regarded as the sums over possible electron trajectories connecting the junctions. There is a direct 1D trajectory that connects the junctions through the nanowire. It accounts for the amplitudes $t_{R,L}^{e,h}$ considered above. In addition, there are trajectories where an electron starts at the junction, escapes to the lead at rather short distances $\nu_w \tau \ll L$, travels in the lead, and returns to the nanowire close to the opposite junction. In distinction from the 1D amplitude, the 3D amplitude represented by the sum over these trajectories is a random quantity: it depends on the disorder configuration in the superconducting lead and vanishes upon the averaging over disorder. Importantly, the variance of this amplitude can be averaged over disorder and is determined by the properties of the superconducting lead at the space scale L rather than the details of the escape. Technically, it is computed as the average of electron Green's function $G(\mathbf{r}, \mathbf{r}')$, \mathbf{r}, \mathbf{r}' being close to the opposite junctions. Besides, there are trajectories that enter and escape the nanowire several times. Since the wire is separated from the lead by a tunnel barrier, and the wire cross-section is small compared to that of the lead, the contribution of such trajectories can be safely neglected. In conclusion, the relevant transmission amplitude in the competition regime is a sum of the 1D amplitude specified above, and a random 3D amplitude. Let us compute the hybridization.

First of all, we need to extend the perturbation theory developed in Sec. 3.7 onto

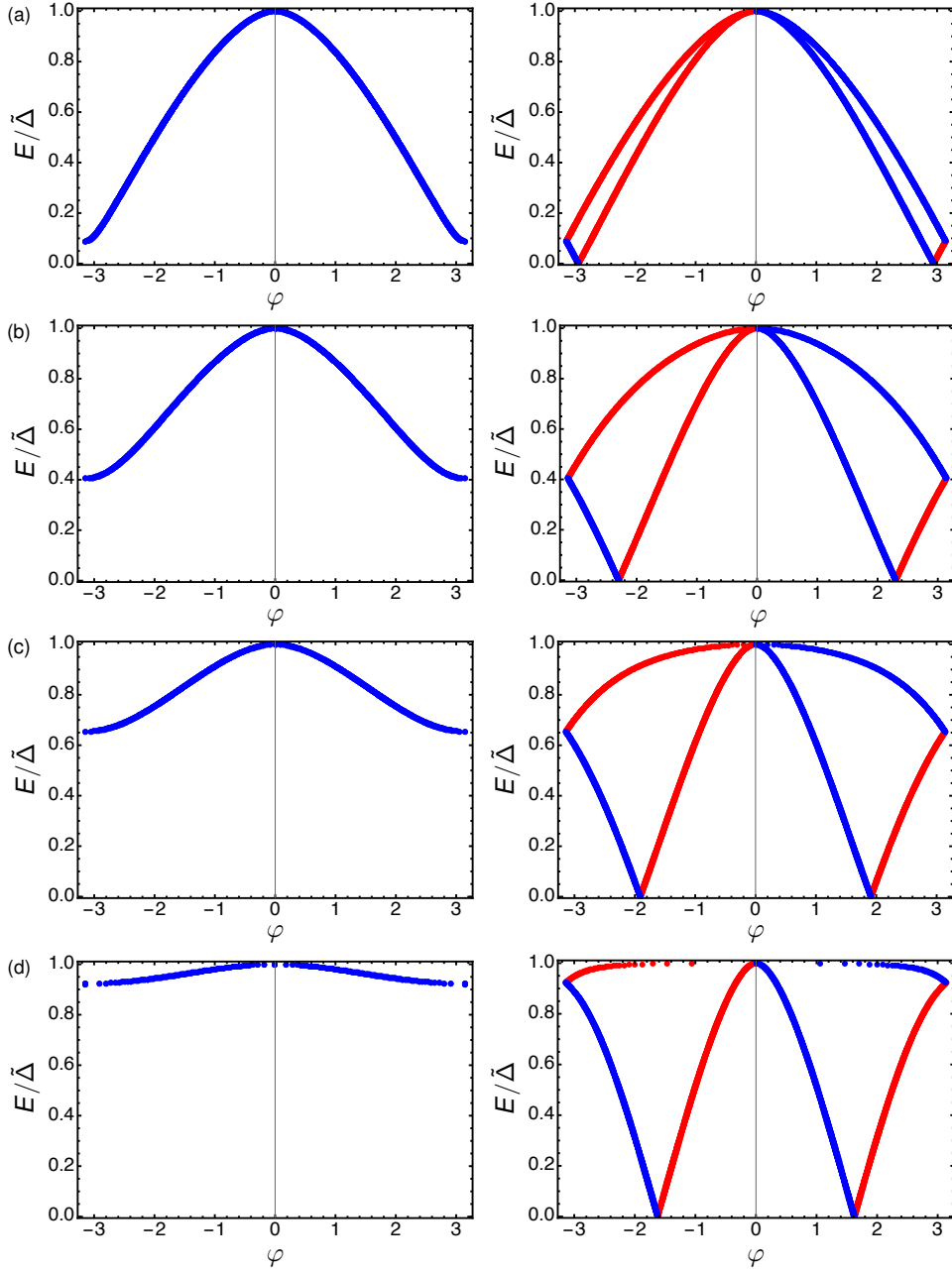


Figure 3.8: The ABS energies for purely ballistic junctions. We plot along the lines $\bar{\varphi}_1 = \bar{\varphi}_2 = \varphi$ (left column) and $\bar{\varphi}_2 = -\bar{\varphi}_1 = \varphi$ (right column). The energies are doubly degenerate in the left column plots. In the right column, the blue (red) color corresponds to right-(left-)moving electrons. The values of $L/(v_w \tau)$ for the rows are: (a) 2.30, (b) 0.8, (c) 0.35 (d) 0.05. We have taken the limit $\tau \Delta \rightarrow 0$ disregarding the energy dependence of ξ_w . The zero energy crossings visible in the right column is the main peculiarity of the purely ballistic case.

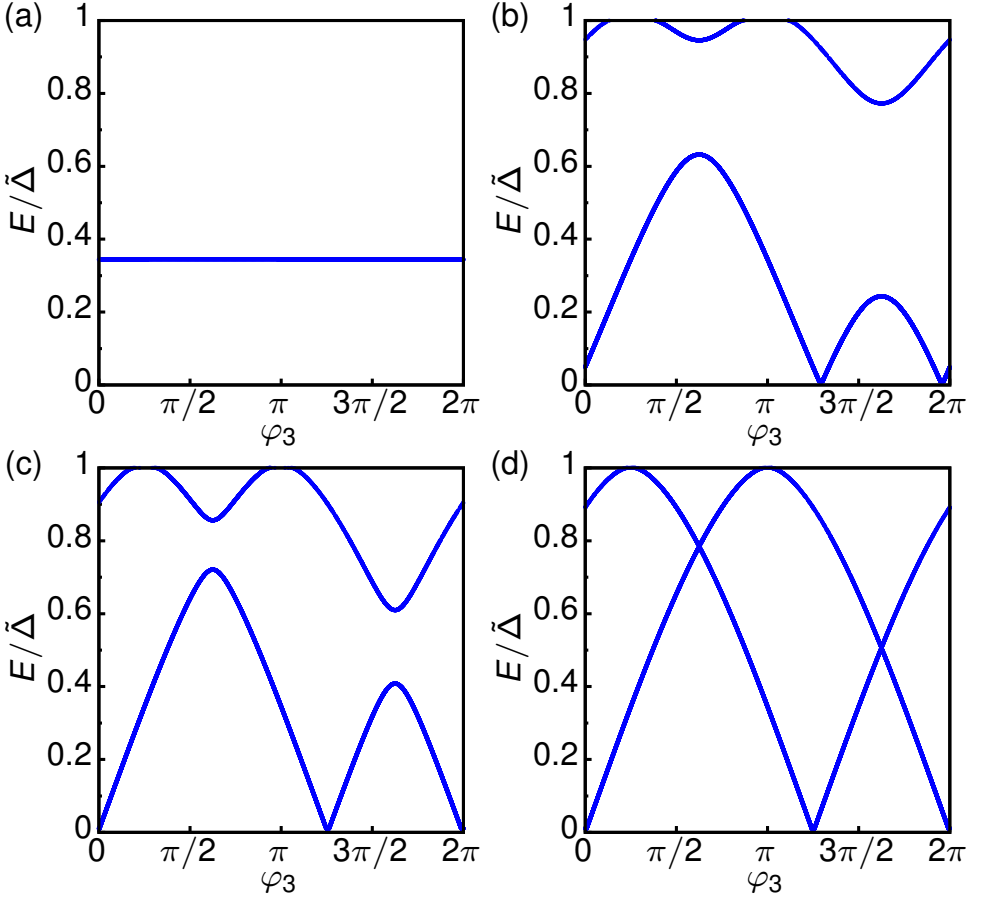


Figure 3.9: The ABS for the setup with purely ballistic junctions ($r_A = r_B = 0$) versus the phase of the third lead φ_3 for a set of different separations L . All parameters except $t_{A,B}$ are the same as for the plots in Fig. 3.4.

arbitrary set of transmission amplitudes connecting the junctions A, B . The non-diagonal matrix element \mathcal{M} can be presented in the following form (cf. Eq. (3.33))

$$\begin{aligned} \mathcal{M} = & \frac{1}{2\chi'(E_0)} \times \\ & \times [e^{-i\frac{\theta_3^A - \theta_3^B}{2}} e^{i\varphi_3} t_{he} u_A^+ u_B^+ + e^{-i\frac{\theta_3^A + \theta_3^B}{2}} t_{hh} u_A^+ u_B^- + \\ & + e^{i\frac{\theta_3^A + \theta_3^B}{2}} t_{ee} u_A^- u_B^+ + e^{i\frac{\theta_3^A - \theta_3^B}{2}} e^{-i\varphi_3} t_{eh} u_A^- u_B^-]. \end{aligned} \quad (3.39)$$

The Eq. (3.33) is reproduced if we leave here only the direct 1D propagation amplitudes substituting $t^{eh} = t^{he} = 0$, $t^{ee} = t_L^e$, $t^{hh} = t_R^h$, with t_L^e, t_R^h taken from Eq. (3.24).

We need to add the 3D amplitudes. We choose two points in the lead \mathbf{r}_A and \mathbf{r}_B , that are close to the corresponding junctions. The matrix of four transmission amplitudes is related to the Green's function describing the propagation between the points as follows[23]:

$$t_{AB} = \frac{i}{2\pi\nu} G_3(\mathbf{r}_A, \mathbf{r}_B), \quad (3.40)$$

ν being the density of states in the lead per one spin direction. Owing to the assumption of the uniform order parameter, the Green's function $G_3(\mathbf{r}_A, \mathbf{r}_B)$ can be related to the quantum propagator $P(\mathbf{r}_A, \mathbf{r}_B, \xi)$ defined in terms of the exact electron wavefunctions $\Psi_n(\mathbf{r})$ in the normal state,

$$P(\mathbf{r}_A, \mathbf{r}_B, \xi) = \sum_n \Psi_n^*(\mathbf{r}_A) \Psi_n(\mathbf{r}_B) \delta(\xi - \xi_n), \quad (3.41)$$

and thus expressed in terms of the electron propagation in the normal state,

$$\begin{aligned} G_3(\mathbf{r}_A, \mathbf{r}_B) = & \\ = & \int d\xi P(\mathbf{r}_A, \mathbf{r}_B, \xi) \frac{1}{\xi^2 + \Delta^2 - E^2} \begin{pmatrix} E + \xi & \Delta e^{i\varphi_3} \\ \Delta e^{-i\varphi_3} & E - \xi \end{pmatrix}, \end{aligned} \quad (3.42)$$

Using Eq. (3.40), we define two 3D amplitudes A_e and A_o for the diffusive case as

$$A_e = \int \frac{d\xi}{2\pi\nu} \frac{\sqrt{\Delta^2 - E^2}}{\xi^2 + \Delta^2 - E^2} P(\mathbf{r}_A, \mathbf{r}_B, \xi), \quad (3.43)$$

$$A_o = \int \frac{d\xi}{2\pi\nu} \frac{\xi}{\xi^2 + \Delta^2 - E^2} P(\mathbf{r}_A, \mathbf{r}_B, \xi). \quad (3.44)$$

Those are real in the subgap region $|E| < \Delta$ provided we assume time reversibility in the normal state. For the energies above the gap, A_e becomes imaginary and these two amplitudes can be related to real and imaginary parts of an electron wave at \mathbf{r}_B , that is emitted from a source at \mathbf{r}_A . With this, the transmission amplitudes are represented as the sum of the 1D propagation amplitudes and two random 3D amplitudes $A_{e,o}$ taken with

proper coefficients,

$$t_{ee} = \frac{iE}{\sqrt{\Delta^2 - E^2}} A_e + iA_0 + e^{ik_F L} (1 - e^{2i\chi}) e^{-L/\xi_w}, \quad (3.45)$$

$$t_{eh} = \frac{i\Delta e^{i\varphi_3}}{\sqrt{\Delta^2 - E^2}} A_e, \quad (3.46)$$

$$t_{he} = \frac{i\Delta e^{-i\varphi_3}}{\sqrt{\Delta^2 - E^2}} A_e, \quad (3.47)$$

$$t_{hh} = \frac{iE}{\sqrt{\Delta^2 - E^2}} A_e - iA_0 + e^{-ik_F L} (1 - e^{2i\chi}) e^{-L/\xi_w}. \quad (3.48)$$

To obtain the variances of the random $A_{e,0}$ we implement the relation between the product of two quantum propagators and the semiclassical propagator $\mathcal{P}(\mathbf{r}_A, \mathbf{r}_B, t)$, that gives the probability for a particle to be at the point \mathbf{r}_B at the time moment t , provided it is at \mathbf{r}_A in the time moment 0. This relation was implemented in Ref. [13] and reads

$$\frac{\nu}{2\pi} \int dt \mathcal{P}(\mathbf{r}_A, \mathbf{r}_B, t) e^{i(\xi - \xi')t} = P(\mathbf{r}_B, \mathbf{r}_A, \xi) P(\mathbf{r}_A, \mathbf{r}_B, \xi'). \quad (3.49)$$

With this, the variances are given by

$$\langle A_e^2 \rangle = \langle A_0^2 \rangle = \frac{1}{8\pi\nu} \int \mathcal{P}(\mathbf{r}_A, \mathbf{r}_B, t) e^{-2\sqrt{\Delta^2 - E^2}|t|} dt, \quad (3.50)$$

$$\langle A_e A_0 \rangle = 0. \quad (3.51)$$

Simply enough, A_e and A_0 are independent variables with equal variations.

There is a remarkably simple and general expression for the variances valid in the limit $L \ll \xi_s$, that is, for the separations much smaller than the correlation length in the superconductor. In this case, we can replace the factor $e^{-2\sqrt{\Delta^2 - E^2}|t|}$ with 1. Let us regard the lead in the normal state as a distributed conducting media earthed far from the points $\mathbf{r}_{A,B}$. Let us inject the current I_A in the point \mathbf{r}_A and measure the voltage V_B at the point \mathbf{r}_B . This defines a three-point resistance $R \equiv V_B / I_A$. Considering kinetics of the semiclassical electron motion, we can express R in terms of the semiclassical propagator,

$$R = \frac{1}{2e^2\nu} \int_0^\infty \mathcal{P}(\mathbf{r}_A, \mathbf{r}_B, t) dt. \quad (3.52)$$

The variances are expressed in terms of this resistance,

$$\langle A_e^2 \rangle = \langle A_0^2 \rangle = \frac{G_Q R}{2}. \quad (3.53)$$

This expression does not depend on the geometry and resistivity distribution in the lead.

To give a simple formula that describes the competition regime, let us assume $E \ll \Delta$, ballistic junctions, and $\text{sgn}\tilde{\varphi}_1 = -\text{sgn}\tilde{\varphi}_2$. Under these assumptions,

$$\mathcal{M} = \tilde{\Delta} \left[-iA_0 + 2e^{-ik_F L} e^{-L/\xi_w} \right], \quad (3.54)$$

and the energy splitting is given by

$$(\delta E)^2 = 4\tilde{\Delta}^2 \left[4e^{-2L/\xi_w} + A_0^2 + 4A_0 \sin(k_F L) e^{-L/\xi_w} \right]. \quad (3.55)$$

Let us note the presence of interference effect that was absent for 1D consideration of ballistic junctions. It arises due to the absence of momentum conservation in the course of 3D propagation. The 1D and 3D propagation provides in average the same contribution into the energy splitting provided $e^{-L/\xi_w} = \sqrt{G_Q \bar{R}/8}$.

In Ref. kornich:pr19 we have addressed the situation $L \simeq \xi_s$ assuming a concrete model of a quasi-2D lead of width L , thickness $d \ll L$, and resistance per square R_\square , $\mathbf{r}_A, \mathbf{r}_B$ being at the corners of the lead. The classical propagator in this case reads:

$$\mathcal{P}(\mathbf{r}_A, \mathbf{r}_B, t) = \frac{1}{dL} \sqrt{\frac{1}{\pi D|t|}} \sum_{n=-\infty}^{\infty} (-1)^n e^{-D \frac{\pi^2}{L^2} n^2 |t|}, \quad (3.56)$$

D being the diffusion coefficient, $D = (2e^2 v d R_\square)^{-1}$.

We neglect the contribution of 1D transmission and find from Eq. (3.39) the average energy splitting

$$(\delta E)^2 = \frac{1}{2(\chi'(E_0))^2} M G_Q R_{\text{eff}} F\left(\frac{L}{\xi_L}\right), \quad (3.57)$$

$$\begin{aligned} M = & \frac{1}{\Delta^2 - E^2} [\Delta^2 + \\ & + 2E\Delta[u_A^- u_A^+ \cos\theta_3^A + u_B^- u_B^+ \cos\theta_3^B] + \\ & + 2u_A^+ u_A^- u_B^+ u_B^- (\Delta^2 \cos(\theta_3^A - \theta_3^B) + \\ & + (2E^2 - \Delta^2) \cos(\theta_3^A + \theta_3^B))], \end{aligned} \quad (3.58)$$

where, conform to the definitions of Ref. kornich:pr19 $R_{\text{eff}} = R_\square \xi_L / L$, $F(z) = 4z/\pi \sum_{n=0}^{\infty} K_0((2n+1)z)$, $F(0) = 1$. This generalizes Eq. (6) of that work to the case of arbitrary scattering matrices. A calculation error in Eq. (6) is corrected by dividing its r.h.s. by π .

3.12. CONCLUSIONS

In this work, we present a detailed study of the ABS spectrum in the three-terminal Andreev molecule setup concentrating on the effects of 1D propagation in the wire and on the competition of 1D and 3D propagation. We have identified several regimes for various relations of the junction separation L as compared with the correlation lengths ξ_w, ξ_s in the nanowire and in the superconducting lead. We have presented the details of ABS spectrum in these regimes and discussed the crossovers between the regimes. In particular, we have discussed the limits of weak and strong 1D hybridization, the interference effect, the emergence of the upper ABS from the continuous spectrum, and detailed the competition of 1D and 3D transmissions seen in the hybridization of the ABS. Our results facilitate the experimental realization of the setup where the presence of the discrete ABS and the peculiarities of their spectrum can be used for quantum sensing and manipulation.

BIBLIOGRAPHY

- [1] Jason Alicea. “New directions in the pursuit of Majorana fermions in solid state systems”. In: *Rep. Prog. Phys.* 75 (June 2012), p. 076501. DOI: [10.1088/0034-4885/75/7/076501](https://doi.org/10.1088/0034-4885/75/7/076501). URL: <https://iopscience.iop.org/article/10.1088/0034-4885/75/7/076501>.
- [2] W Chang et al. “Hard gap in epitaxial semiconductor–superconductor nanowires”. In: *Nature nanotechnology* 10.3 (2015), p. 232.
- [3] W. Chang et al. “Tunneling Spectroscopy of Quasiparticle Bound States in a Spinful Josephson Junction”. In: *Phys. Rev. Lett.* 110 (21 May 2013), p. 217005. DOI: [10.1103/PhysRevLett.110.217005](https://doi.org/10.1103/PhysRevLett.110.217005). URL: <https://link.aps.org/doi/10.1103/PhysRevLett.110.217005>.
- [4] Nikolai M. Chtchelkatchev and Yu. V. Nazarov. “Andreev Quantum Dots for Spin Manipulation”. In: *Phys. Rev. Lett.* 90 (22 June 2003), p. 226806. DOI: [10.1103/PhysRevLett.90.226806](https://doi.org/10.1103/PhysRevLett.90.226806). URL: <https://link.aps.org/doi/10.1103/PhysRevLett.90.226806>.
- [5] Anindya Das et al. “Zero-bias peaks and splitting in an Al–InAs nanowire topological superconductor as a signature of Majorana fermions”. In: *Nature Physics* 8.12 (2012), p. 887.
- [6] R. S. Deacon et al. “Tunneling Spectroscopy of Andreev Energy Levels in a Quantum Dot Coupled to a Superconductor”. In: *Phys. Rev. Lett.* 104 (7 Feb. 2010), p. 076805. DOI: [10.1103/PhysRevLett.104.076805](https://doi.org/10.1103/PhysRevLett.104.076805). URL: <https://link.aps.org/doi/10.1103/PhysRevLett.104.076805>.
- [7] MT Deng et al. “Anomalous zero-bias conductance peak in a Nb–InSb nanowire–Nb hybrid device”. In: *Nano letters* 12.12 (2012), pp. 6414–6419.
- [8] MF Goffman et al. “Conduction channels of an InAs–Al nanowire Josephson weak link”. In: *New Journal of Physics* 19.9 (2017), p. 092002.
- [9] Önder Gül et al. “Hard Superconducting Gap in InSb Nanowires”. In: *Nano Letters* 17.4 (Apr. 2017), pp. 2690–2696. DOI: [10.1021/acs.nanolett.7b00540](https://doi.org/10.1021/acs.nanolett.7b00540). URL: <https://doi.org/10.1021/acs.nanolett.7b00540>.
- [10] M. Hays et al. “Direct Microwave Measurement of Andreev-Bound-State Dynamics in a Semiconductor–Nanowire Josephson Junction”. In: *Phys. Rev. Lett.* 121 (4 July 2018), p. 047001. DOI: [10.1103/PhysRevLett.121.047001](https://doi.org/10.1103/PhysRevLett.121.047001). URL: <https://link.aps.org/doi/10.1103/PhysRevLett.121.047001>.

- [11] C. Janvier et al. “Coherent manipulation of Andreev states in superconducting atomic contacts”. In: *Science* 349.6253 (2015), pp. 1199–1202. ISSN: 0036-8075. DOI: [10.1126/science.aab2179](https://doi.org/10.1126/science.aab2179). eprint: <https://science.sciencemag.org/content/349/6253/1199.full.pdf>. URL: <https://science.sciencemag.org/content/349/6253/1199>.
- [12] M. Kjaergaard et al. “Quantized conductance doubling and hard gap in a two-dimensional semiconductor–superconductor heterostructure”. In: *Nature Communications* 7.1 (2016), p. 12841. DOI: [10.1038/ncomms12841](https://doi.org/10.1038/ncomms12841). URL: <https://doi.org/10.1038/ncomms12841>.
- [13] Viktoriia Kornich, Hristo S. Barakov, and Yuli V. Nazarov. “Fine energy splitting of overlapping Andreev bound states in multiterminal superconducting nanostructures”. In: *Phys. Rev. Research* 1 (3 Oct. 2019), p. 033004. DOI: [10.1103/PhysRevResearch.1.033004](https://doi.org/10.1103/PhysRevResearch.1.033004). URL: <https://link.aps.org/doi/10.1103/PhysRevResearch.1.033004>.
- [14] Viktoriia Kornich, Hristo S. Barakov, and Yuli V. Nazarov. “Overlapping Andreev states in semiconducting nanowires: Competition of one-dimensional and three-dimensional propagation”. In: *Phys. Rev. B* 101.19 (May 2020), p. 195430. ISSN: 2469-9969. DOI: [10.1103/PhysRevB.101.195430](https://doi.org/10.1103/PhysRevB.101.195430).
- [15] G. de Lange et al. “Realization of Microwave Quantum Circuits Using Hybrid Superconducting–Semiconducting Nanowire Josephson Elements”. In: *Phys. Rev. Lett.* 115 (12 Sept. 2015), p. 127002. DOI: [10.1103/PhysRevLett.115.127002](https://doi.org/10.1103/PhysRevLett.115.127002). URL: <https://link.aps.org/doi/10.1103/PhysRevLett.115.127002>.
- [16] T. W. Larsen et al. “Semiconductor-Nanowire-Based Superconducting Qubit”. In: *Phys. Rev. Lett.* 115 (12 Sept. 2015), p. 127001. DOI: [10.1103/PhysRevLett.115.127001](https://doi.org/10.1103/PhysRevLett.115.127001). URL: <https://link.aps.org/doi/10.1103/PhysRevLett.115.127001>.
- [17] Eduardo J. H. Lee et al. “Spin-resolved Andreev levels and parity crossings in hybrid superconductor–semiconductor nanostructures”. In: *Nature Nanotechnology* 9 (Dec. 2013), 79 EP -. URL: <https://doi.org/10.1038/nnano.2013.267>.
- [18] R. M. Lutchyn. In: *private communications* (2019).
- [19] Roman M. Lutchyn, Jay D. Sau, and S. Das Sarma. “Majorana Fermions and a Topological Phase Transition in Semiconductor-Superconductor Heterostructures”. In: *Phys. Rev. Lett.* 105 (7 Aug. 2010), p. 077001. DOI: [10.1103/PhysRevLett.105.077001](https://doi.org/10.1103/PhysRevLett.105.077001). URL: <https://link.aps.org/doi/10.1103/PhysRevLett.105.077001>.
- [20] Georgo Metalidis et al. “Nonlocal conductance via overlapping Andreev bound states in ferromagnet-superconductor heterostructures”. In: *Phys. Rev. B* 82 (18 Nov. 2010), p. 180503. DOI: [10.1103/PhysRevB.82.180503](https://doi.org/10.1103/PhysRevB.82.180503). URL: <https://link.aps.org/doi/10.1103/PhysRevB.82.180503>.

- [21] V. Mourik et al. “Signatures of Majorana Fermions in Hybrid Superconductor-Semiconductor Nanowire Devices”. In: *Science* 336.6084 (2012), pp. 1003–1007. ISSN: 0036-8075. DOI: [10.1126/science.1222360](https://doi.org/10.1126/science.1222360). eprint: <https://science.sciencemag.org/content/336/6084/1003.full.pdf>. URL: <https://science.sciencemag.org/content/336/6084/1003>.
- [22] Y.V. Nazarov and Y. Blanter. *Quantum Transport. Introduction to Nanoscience*. Cambridge University Press, 2009.
- [23] Yu. V. Nazarov. “Limits of universality in disordered conductors”. In: *Phys. Rev. Lett.* 73 (1 July 1994), pp. 134–137. DOI: [10.1103/PhysRevLett.73.134](https://doi.org/10.1103/PhysRevLett.73.134). URL: <https://link.aps.org/doi/10.1103/PhysRevLett.73.134>.
- [24] Yuval Oreg, Gil Refael, and Felix von Oppen. “Helical Liquids and Majorana Bound States in Quantum Wires”. In: *Phys. Rev. Lett.* 105 (17 Oct. 2010), p. 177002. DOI: [10.1103/PhysRevLett.105.177002](https://doi.org/10.1103/PhysRevLett.105.177002). URL: <https://link.aps.org/doi/10.1103/PhysRevLett.105.177002>.
- [25] J. -D. Pillet et al. In: *arXiv:1809.11011v1* (2018).
- [26] J. -D. Pillet et al. “Nonlocal Josephson Effect in Andreev Molecules”. In: *Nano Letters* 19.10 (Oct. 2019), pp. 7138–7143. DOI: [10.1021/acs.nanolett.9b02686](https://doi.org/10.1021/acs.nanolett.9b02686). URL: <https://doi.org/10.1021/acs.nanolett.9b02686>.
- [27] J. -D. Pillet et al. “Scattering description of Andreev molecules”. In: *arXiv:2002.10952* (2020).
- [28] Sébastien R. Plissard et al. “Formation and electronic properties of InSb nanocrosses”. In: *Nature Nanotechnology* 8 (Oct. 2013), 859 EP -. URL: <https://doi.org/10.1038/nnano.2013.198>.
- [29] Jay D. Sau et al. “Non-Abelian quantum order in spin-orbit-coupled semiconductors: Search for topological Majorana particles in solid-state systems”. In: *Phys. Rev. B* 82 (21 Dec. 2010), p. 214509. DOI: [10.1103/PhysRevB.82.214509](https://doi.org/10.1103/PhysRevB.82.214509). URL: <https://link.aps.org/doi/10.1103/PhysRevB.82.214509>.
- [30] Z. Scherübl, A. Pályi, and S. Csonka. “Transport signatures of an Andreev molecule in a quantum dot?superconductor?quantum dot setup”. In: *Beilstein J. Nanotechnol.* 10 (2019), p. 363.
- [31] D. Sherman et al. “Normal, superconducting and topological regimes of hybrid double quantum dots”. In: *Nature Nanotechnology* 12 (Nov. 2016), 212 EP -. URL: <https://doi.org/10.1038/nnano.2016.227>.
- [32] Tudor D. Stanescu, Roman M. Lutchyn, and S. Das Sarma. “Majorana fermions in semiconductor nanowires”. In: *Phys. Rev. B* 84 (14 Oct. 2011), p. 144522. DOI: [10.1103/PhysRevB.84.144522](https://doi.org/10.1103/PhysRevB.84.144522). URL: <https://link.aps.org/doi/10.1103/PhysRevB.84.144522>.
- [33] Zhaoen Su et al. “Andreev molecules in semiconductor nanowire double quantum dots”. In: *Nature communications* 8.1 (2017), p. 585.
- [34] Zhaoen Su et al. “Andreev molecules in semiconductor nanowire double quantum dots - Nature Communications”. In: *Nat. Commun.* 8.585 (Sept. 2017), pp. 1–6. ISSN: 2041-1723. DOI: [10.1038/s41467-017-00665-7](https://doi.org/10.1038/s41467-017-00665-7).

- [35] L. Tosi et al. “Spin-Orbit Splitting of Andreev States Revealed by Microwave Spectroscopy”. In: *Phys. Rev. X* 9 (1 Jan. 2019), p. 011010. DOI: [10.1103/PhysRevX.9.011010](https://doi.org/10.1103/PhysRevX.9.011010). URL: <https://link.aps.org/doi/10.1103/PhysRevX.9.011010>.
- [36] David J. van Woerkom et al. “Microwave spectroscopy of spinful Andreev bound states in ballistic semiconductor Josephson junctions”. In: *Nature Physics* 13 (June 2017), 876 EP -. URL: <https://doi.org/10.1038/nphys4150>.
- [37] Tomohiro Yokoyama and Yuli V. Nazarov. “Singularities in the Andreev spectrum of a multiterminal Josephson junction”. In: *Phys. Rev. B* 92 (15 Oct. 2015), p. 155437. DOI: [10.1103/PhysRevB.92.155437](https://doi.org/10.1103/PhysRevB.92.155437). URL: <https://link.aps.org/doi/10.1103/PhysRevB.92.155437>.
- [38] A. Zazunov et al. “Andreev Level Qubit”. In: *Phys. Rev. Lett.* 90 (8 Feb. 2003), p. 087003. DOI: [10.1103/PhysRevLett.90.087003](https://doi.org/10.1103/PhysRevLett.90.087003). URL: <https://link.aps.org/doi/10.1103/PhysRevLett.90.087003>.

4

SUPERCURRENT IN THE PRESENCE OF DIRECT TRANSMISSION AND A RESONANT LOCALIZED STATE

*If it wasn't for bad luck,
I would have no luck at all.*

Albert King

This chapter has been published as Supercurrent in the presence of direct transmission and a resonant localized state [1] and the data is available on https://zenodo.org/record/5879475#.YfunmC8w2_U.

4.1. SCOPE, STYLE AND STRUCTURE OF THE CHAPTER

In its present form, this Chapter is not intended for a submission to a journal. We believe that the theory developed here is worth a journal publication only together with the account of experimental activities, and full comparison of experimental and theoretical findings. This publication is in preparation.

We also find the model to be of significant general interest for current research in superconducting nanostructures. Despite the basic simplicity, the derivation of the model and elaboration on concrete results invokes a big number of technical details which are not normally given in a journal publication. So we chose to share our results in the present form that gives a full account of these technical details.

The structure of the Chapter is as follows. In Section 4.2, we give a short summary of our impression of the experimental results. We explain motivation of the model and list its key ingredients in Section 4.3. The Hamiltonian formulation is given in Section 4.4. In Section 4.5 we derive the Landauer description of normal electron transport for an arbitrary number of dots and leads. We specify to two-dot, two-lead model in Section 4.6 where we perform the necessary derivations to adjust the model to the situation at hand for the case of normal transport. The illustrative normal transport examples are given in Section 4.7. We turn to theoretical description of superconducting transport in Section 4.8 and describe our numerical methods in Section 4.9. The most important Section ?? provides several examples of superconducting transport. We conclude in Section 4.10.

4.2. SHORT SUMMARY OF EXPERIMENTAL OBSERVATIONS

Let us shortly present the essence of experimental findings that inspired us to elaborate on the model. These experiments have been performed by V. Levajac, J. Y. Wang, L.P. Kouwehnoen, and other members of their team at QuTech, Delft University of Technology. The proper account of the experiments will be published elsewhere. Here we present our personal (theoretical) impression of the results.

The setup involves two superconducting junctions made by covering a semiconducting nanowire with superconducting electrodes. The junctions are enclosed in a SQUID loop that enables to characterize the dependence of the currents in the junctions on the superconducting phases changing the magnetic flux in the loop. A substantial magnetic field can be also applied in the plane of the substrate. There are gate electrodes affecting the junctions separately. The measurement is a simple voltage measurement at a given current bias. (Fig. 4.1 a). From this, one can inherit the critical current of two junctions in parallel. Another parameter that can be varied in this experiment is the magnetic field in the plane of substrate, parallel field.

Naturally, the supercurrents vary smoothly upon changing the gate voltages at various magnetic fields. This is explained by depletion/addition of electron density to the junction that closes/opens the transport channels and modulates their transparency. The conductances of the junctions are several $G_Q \equiv e^2/\pi\hbar$ suggesting 1-2 open transport channels. An unusual observation the experimentalists share with us is a sharp dependence of the supercurrent upon changing one of the gate voltages in a narrow interval. In this interval, the change of the electron energies induced by the gate voltage is of the order of 1meV, that is comparable with the value of the superconducting gap and Zeeman energy coming from the parallel

field.

Some data can be interpreted as two close $0 - \pi$ transitions in this narrow interval of gate voltages. In an idealized case (which is not necessary an experimental one) where the supercurrents through the junctions differ much in the magnitude, the $I - \phi$ dependence of the Josephson current in the junction with smaller current can be directly seen in the dependence of the critical current on the flux Φ in the SQUID loop. If one changes the gate voltage controlling the smallest junction, the observation could be then summarized as follows (Fig. 4.1 b): i. the positions of supercurrent minima are close to $\Phi_0/4 + n\Phi_0$ indicating the minimum of Josephson energy at $\phi = 0$ ii. π -shifted dependence in the middle of the interval indicating the minimum of Josephson energy at $\phi = \pi$ iii. Double periodicity of the current at the borders of the interval.

Such pairs of close $0 - \pi$ transitions occur may occur several times at different gate voltage settings. The widths of the interval increases upon increasing the parallel magnetic field. Sometimes the transitions merge and disappear at small magnetic field. Sometimes the effect persists even at zero field.

4.3. THE MOTIVATION AND ESSENCE OF THE MODEL

The sharp dependence on the gate voltage in a narrow interval suggest that a localized state is involved. The gate voltage shifts its energy level with respect to Fermi energy. Beyond the interval, the state is either empty or occupied and hardly participates in transport, either normal or superconducting. In the interval, resonant transport occurs via the state. The width of the interval is set by either Γ , the width of the level due to escape to the leads, or Δ , the superconducting energy gap.

There are known mechanisms of $0 - \pi$ transitions involving a localized state. First one is due to spin splitting of Andreev states in magnetic field. If the splitting is of the order of Δ , the curvature of Andreev levels at zero phase may be inverted, and the Josephson energy achieves minimum at $\phi = \pi$ rather than zero. If interaction in the localized state is essential, the state is single-occupied in an interval of the gate voltage, and the minimum of Josephson energy may be at $\phi = \pi$ in this interval (Contrary to a popular belief, this is not always true for a single-occupied state). These mechanisms are not mutually exclusive but rather related: in a mean-field approximation, the interaction may be described as a spin splitting, and the field-induced splitting leads to single occupation if the chemical potential is between the split levels. This provides extra motivation to explain the experimental observation with a localized state.

However, the situation is obviously more complex than just the transport through a localized state. At least a single transport channel is open when the localized state becomes resonant. A very simplistic model would be independent parallel transport in the localized state and in the channel. This model, however, is not flexible enough to fit the experimental data. We need to take into account interference of transmissions through the channel and the resonant states.

A motivation for this also comes from the presumed geometry of electron distribution in the nanowire: the localized states are most likely appear in random potential minima of a nanowire part where the density is depleted. (Fig. 4.2 a) Electron tunneling from these minima may proceed to the leads as well as to the transport channel. There may be many such minima that are subsequently filled upon changing the gate voltage giving rise to many

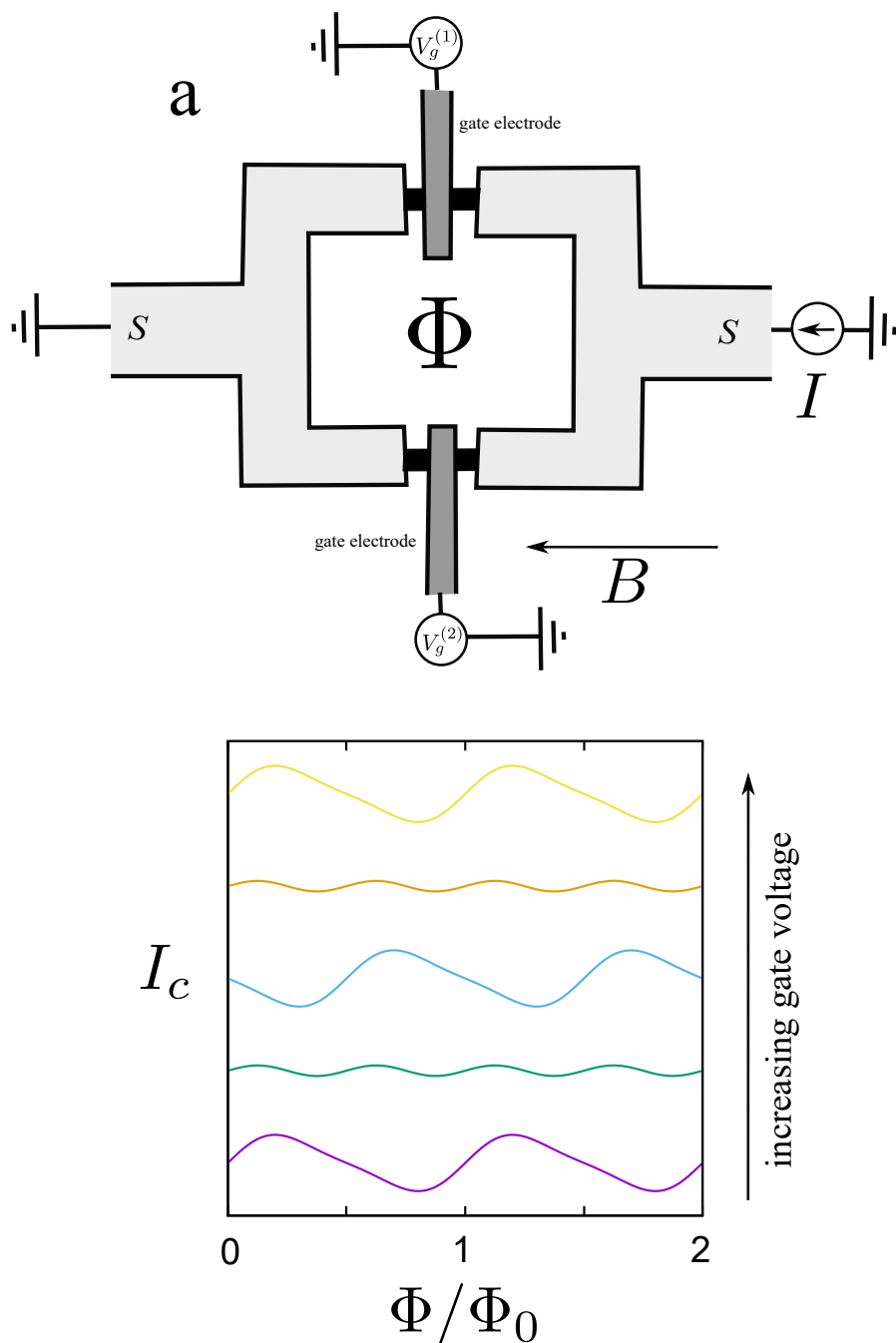


Figure 4.1: a. Scheme of the setup (not in scale). Two semiconducting wires (black) are covered with a superconducting film (light grey) forming two Josephson junctions in a SQUID loop. The wires are affected by the voltages applied to the gate electrodes (dark grey). The loop is penetrated by magnetic flux Φ . The parallel magnetic field B may be applied. b. An intriguing observation: a pair of $0-\pi$ transitions in a narrow interval of a gate voltage. The curves give the dependence of critical current on the flux in the loop for a set of increasing gate voltages and are offset for clarity.

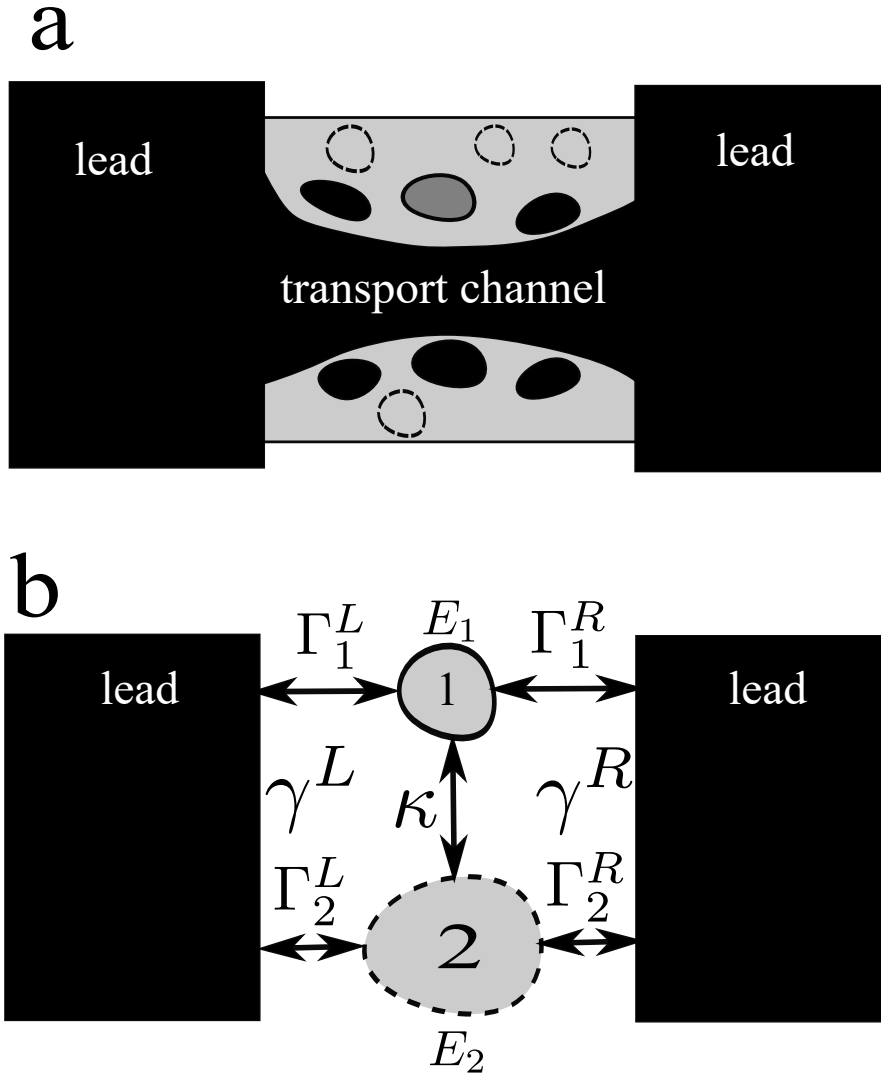


Figure 4.2: a. Cross-section of the wire. Geometry of electron distribution in the wire and the leads. The filled states are given in black. The electron density is depleted near the wire surface. Random potential minima are either filled (small black regions) or empty (regions with dashed boundaries). The resonant state is given in dark grey. b. Essential parameters of the two-dot model in use. The second dot is only used to simulate a transport channel with a transmission not depending on energy, so that the tunnel rates $\Gamma_{1,2}^{R,L}$ and the positions of the dot energy levels with respect to Fermi level, $E_{1,2}$, satisfy $\Gamma_2^{R,L}, E_2 \gg \Delta \approx \Gamma_1^{R,L}, E_1$. There is also tunneling κ between the dots, and the tunneling rates $\gamma_{R,L}$ that cannot be ascribed to a certain dot.

localized states. We note that only the states with the escape rate $\Gamma \simeq \Delta$ may be responsible for the observed peculiarity. Those with $\Gamma \gg \Delta$ modify the transport smoothly at the energy scale Γ , so at the energy scale Δ that is relevant for superconducting transport would only cause the renormalization of the transmission coefficients of the transport channels. Those with $\Gamma \ll \Delta$ modify the transmission only in a narrow energy interval: this would not give rise to Andreev states that require significant transmission at two opposite energies (for electrons and holes).

To formulate a practical model encompassing the channel and the localized state, we note that the transport channel can be conveniently modelled with a localized state as well, provided the escape rate of this state Γ_2 by far exceeds Δ . So we elaborate the model that encompasses two localized states, or dots, that are connected to two leads by tunnelling. Before writing any Hamiltonians, let us list most important parameters of the model (see Fig. 4.2 b). Two dots are at energy levels $E_{1,2}$ and are connected to left and right lead by tunneling with the rates $\Gamma_{1,2}^{L,R}$. There is a direct tunnel coupling κ between the dots. Important non-trivial element are tunneling rates $\gamma_{L,R}$ that can not be ascribed to a certain dot but are required to describe tunneling of a superposition state of two dots. Since the second dot is here only to model a channel, the model only makes sense under assumption $\Gamma_2^{L,R} \gg \Gamma_1^{L,R}, E_1$. Owing to this, we can neglect the influence of the gate voltage and magnetic field on E_2 . The parameters κ, γ are at intermediate scale, $\kappa, \gamma \simeq \sqrt{\Gamma_1 \Gamma_2}$.

The most important interaction in this model is the on-site interaction in the localized state. It would be tempting to neglect this interaction, since we cannot treat it exactly. Besides, the localized state is near the transport channel so the interaction should be strongly suppressed by screening. However, the $0-\pi$ transition pairs are sometimes observed at zero magnetic field, this suggests that interaction should play a role. We compromise by treating the on-site interaction in a simple mean-field approach.

The bandstructure of the semiconductor material of the wire provides strong spin-orbit interaction that we also include to the model. The coefficients $\kappa, \gamma_{L,R}$ therefore possess the corresponding spin structure.

4.4. HAMILTONIANS

In this Section, we give the Hamiltonians of the constituents of our model.

4.4.1. THE SINGLE DOT

We start with a dot Hamiltonian. It involves on-site annihilation operators \hat{d}_α , α being the spin index, and reads

$$\hat{H}_D = \hat{d}_\alpha^\dagger H_{\alpha\beta} \hat{d}_\beta + U \hat{n}_\uparrow \hat{n}_\downarrow \quad (4.1)$$

$\hat{n}_\alpha = \hat{d}_\alpha^\dagger \hat{d}_\alpha$. The single-particle Hamiltonian reads

$$\check{H} = E + \mathbf{B} \cdot \boldsymbol{\sigma}$$

\mathbf{B} being the magnetic field, $\boldsymbol{\sigma}$ being the vector of Pauli matrices.

Importantly, we treat the interaction in the mean-field approximation. If there is a natural quantization axis (that can be absent in the presence of SO interaction in the coupling

to the leads), the mean field gives the following additions to the single-particle Hamiltonian,

$$H_{\uparrow\uparrow} = U\langle\hat{n}_{\downarrow}\rangle; H_{\downarrow\downarrow} = U\langle\hat{n}_{\uparrow}\rangle. \quad (4.2)$$

In general situation,

$$H_{\alpha\beta} = U\left(\delta_{\alpha\beta}\langle\hat{N}\rangle - \langle\hat{d}_{\alpha}^{\dagger}\hat{d}_{\beta}\rangle\right) \quad (4.3)$$

The advantage of this mean-field scheme is that it delivers exact results in the absence of tunnel coupling. In particular, at zero magnetic field the ground state corresponds to single occupation of the dot in the interval $U > E - \mu > 0$. At the ends of the interval, sharp transitions bring the dot to the states of zero and double occupation. The scheme is approximate in the presence of tunnel coupling, yet we use it for the lack of better general approach to interaction.

4.4.2. THE LEADS

We introduce annihilation operators in the leads $\hat{c}_{k,\alpha}$ where k labels the states of quasi-continuous spectrum in the leads. The states k are distributed over the leads, those are labelled with a . We assume the states k are invariant with respect to time inversion.

The leads are described by the usual BSC Hamiltonian

$$\hat{H}_{\text{leads}} = \sum_k \xi_k \hat{c}_{k,\alpha}^{\dagger} \hat{c}_{k,\alpha} + \sum_a \sum_{k \in a} (\Delta_a^* \hat{c}_{k,\uparrow} \hat{c}_{k,\downarrow} + \text{h.c.}) \quad (4.4)$$

ξ_k are the energies of the corresponding states. The superconducting order parameter Δ_a is different in different leads. To describe normal leads, we just put $\Delta_a = 0$.

4.4.3. TUNNEL COUPLING

The tunnel coupling to the states is described by the following Hamiltonian

$$\hat{H}_T = \sum_k \hat{c}_{k,\alpha}^{\dagger} t_{\alpha\beta}^k \hat{d}_{\beta} + \text{h.c.} \quad (4.5)$$

For time-reversible case, the tunnel amplitudes are given by

$$\check{t} = t_k + i\mathbf{t}_k \cdot \boldsymbol{\sigma} \quad (4.6)$$

with real t_k, \mathbf{t}_k . Of course, the multitude of tunneling amplitudes comes to the answers only in a handful of parameters. One of such parameters is the decay rate from the dot to the continuous spectrum of the lead a ,

$$\Gamma_a(\epsilon) = 2\pi \sum_{k \in a} (|t_k|^2 + |\mathbf{t}_k|^2) \delta(\xi_k - \epsilon) \quad (4.7)$$

One can disregard the dependence of the rates on the energy ϵ .

4.5. NORMAL TRANSPORT FOR MANY DOTS

In this Section, we will derive the currents in the nanostructure assuming the leads are normal and are kept at different filling facts. We do this derivation for an arbitrary number

of the leads and dots, and later specify this for two dots and two terminals. Let us consider the following Hamiltonian where we do not specify spin or dot structure

$$\hat{H} = \sum_k \xi_k \hat{c}_k^\dagger c_k + \hat{d}_\alpha^\dagger H_{\alpha\beta} \hat{d}_\beta + \sum_k (\hat{c}_k^\dagger t^{k\beta} \hat{d}_\beta + h.c) \quad (4.8)$$

The Heisenberg equations read

$$i\dot{\hat{c}}_k = \xi_k \hat{c}_k + t_{k\alpha} \hat{d}_\alpha \quad (4.9)$$

$$i\dot{\hat{d}}_\alpha = H_{\alpha\beta} \hat{d}_\beta + t_{k\alpha}^* \hat{c}_k \quad (4.10)$$

The current operators are thus given by

$$\hat{I}_a = \sum_{k \in a} -i t_{k\alpha} \hat{d}_k^\dagger \hat{c}_\alpha + h.c. \quad (4.11)$$

We solve for operators \hat{c}_k ,

$$\hat{c}_k(t) = \hat{c}_k^0 e^{-ix_k t} + \int dt' g_k(t, t') t_{k\alpha} \hat{d}_\alpha(t'),$$

$g_k(t, t') \equiv -ie^{-i\xi_k(t-t')}$, and subsequently for \hat{d}_α ,

$$\hat{d}_\alpha(t) = \int dt' G_{\alpha\beta}(t, t') t_{\beta k}^* e^{-i\xi_k t'} \hat{d}_k^0$$

where the Green's function obeys

$$(i\partial_t - \check{H} - \check{\Sigma}) \check{G} = \delta(t - t') \quad (4.12)$$

and

$$\check{\Sigma}(t, t') = \sum_k t_{k\alpha}^* g_k(t, t') t_{k\beta}. \quad (4.13)$$

It is also useful to introduce partial Σ that describe the decay to a certain lead,

$$\check{\Sigma}^a(t, t') = \sum_{k \in a} t_{k\alpha}^* g_k(t, t') t_{k\beta} \quad (4.14)$$

. With this,

$$\begin{aligned} \hat{c}_k(t) &= c_k^0 e^{-i\xi_k t} \\ &+ g_k(t, t') t_{k\alpha} G_{\alpha\beta}(t', t'') t_{k'\beta}^* e^{-i\xi_{k'} t''} \hat{c}_{k'}^0 \end{aligned} \quad (4.15)$$

in the above expression, we assume summation over t', t'', k' . We substitute this into the current operator, average over the quantum state replacing $\langle \hat{c}_k^{0\dagger} \hat{c}_k^0 \rangle = f_k$ and get two contributions corresponding to two terms in Eq. 4.15. The contribution A depends only on the filling factor in the lead a and reads

$$I_A^a = \text{Tr} \left(\check{G}(t, t') \check{F}^a(t', t) - \check{F}^a(t, t') \check{G}(t, t') \right) \quad (4.16)$$

where $\tilde{G}(t, t') \equiv G^\dagger(t', t)$,

$$\check{F}^a(t, t') = \sum_{k \in a} t_{k\alpha}^* t_{k\beta} f_k e^{-i\xi_k(t-t')} \quad (4.17)$$

The contribution B depends on filling factors in all leads

$$I_B^a = \text{Tr} \left(\check{G}(t, t') \sum_b \check{F}^b(t', t'') \check{G}(t'', t''') \Sigma_a^\dagger(t''', t) \right. \\ \left. - \Sigma_a(t, t') \check{G}(t', t'') \sum_b \check{F}^b(t'', t''') \check{G}(t''', t) \right) \quad (4.18)$$

We switch to the energy representation. To deal with the tunnel amplitudes, we will use the following relation

$$\check{\Gamma}^a(\epsilon) = 2\pi \sum_k t_{k\alpha}^* t_{k\beta} \delta(\epsilon - \xi_k) \quad (4.19)$$

$\check{\Gamma}^a$ characterizing the decay from all dots to the lead a . Conventionally, we will disregard the energy dependence of Γ (since we are working close to the Fermi level). With this,

$$\check{F}^a = -i\check{\Gamma}^a f_a(\epsilon); \quad \check{\Sigma}_a = -\frac{i}{2}\check{\Gamma}^a, \quad (4.20)$$

where we have taken into account that the filling factor depends on energy only, and disregarded real part of Σ (that would lead to a renormalization of the dot Hamiltonian). With this, the Green function is given by

$$\check{G} = \frac{1}{\epsilon - \check{H} + i\check{\Gamma}/2}; \quad (4.21)$$

$\check{\Gamma} \equiv \sum_a \check{\Gamma}_a$. The B contribution for the current for all $b \neq a$ can be written as

$$I_a/e = \sum_{b \neq a} \int \frac{d\epsilon}{2\pi} P_{ab}(\epsilon) f_b(\epsilon) \quad (4.22)$$

P_{ab} being the probability to scatter from all channels of terminal b to the channels of terminal a ,

$$P_{ab}(\epsilon) = \text{Tr}\{\check{\Gamma}^a \check{G}(\epsilon) \check{\Gamma}^b \check{G}(\epsilon)\} \quad (4.23)$$

This is in accordance with the corresponding part of Landauer formula for multi-terminal case. The contribution A reads:

$$I_A^a/e = -i \int \frac{d\epsilon}{2\pi} f_a(\epsilon) \text{Tr}\{\check{\Gamma}^a (\check{G} - \check{\check{G}})\} \quad (4.24)$$

We use the relation

$$\check{G} - \check{\check{G}} = -i\check{G}\check{\Gamma}\check{G} \quad (4.25)$$

to represent the contribution A in the form

$$I_A^a/e = - \int \frac{d\epsilon}{2\pi} f_a(\epsilon) \sum_b P_{ab}(\epsilon) \quad (4.26)$$

summing everything together, we reproduce the Landauer formula

$$I_a/e = \int \frac{d\epsilon}{2\pi} \sum_{b \neq a} P_{ab}(\epsilon) (f_a(\epsilon) - f_b(\epsilon)) \quad (4.27)$$

Let us construct a scattering matrix corresponding to the situation. The scattering to a terminal a is described by $\check{\Gamma}^a$. Let us represent this matrix as $\check{\Gamma}^a = \check{W}_a^\dagger \check{W}_a$. The matrix \check{W}_a is a matrix where the second index goes over the dots and the first one over the channels of the terminal a . This is of course an ambiguous representation, but so the scattering matrix is (tell more about?) We combine all matrices W_a block by block to the matrix W where the first index goes over all channels in all terminals. We note $\check{W}^\dagger \check{W} = \check{\Gamma}$. With this, a scattering matrix describing the situation reads

$$\check{S} = 1 - i\check{W}\check{G}\check{W}^\dagger \quad (4.28)$$

Its unitarity can be proven with using the relation (4.25).

4.6. NORMAL TRANSPORT FOR TWO DOTS

The case of the two dots, two terminals seems trivial but requires some elaboration for the limit where Γ in the dots are very different, this is the case under consideration. To warm up, let us specify to a single dot. We note that Γ_a in this case are diagonal in spin owing to time-reversability and can be regarded as numbers. The transmission probability from the left to the right (or vice versa) can be written as

$$T_0(\epsilon) = \frac{\Gamma_L \Gamma_R}{(\epsilon - E)^2 + \Gamma^2/4} \quad (4.29)$$

The ideal transmission is achieved at $\Gamma_L = \Gamma_R = \Gamma/2$ and $\epsilon = E$. Let us go for two dots and list possible parameters of the model. Those are: level energies (split in spin) $E_1 + \mathbf{B}_1 \cdot \boldsymbol{\sigma}$, $E_2 + \mathbf{B}_1 \cdot \boldsymbol{\sigma}$, decays from the dots $\Gamma_1 = \Gamma_1^L + \Gamma_1^R$, $\Gamma_2 = \Gamma_2^L + \Gamma_2^R$, tunneling between the dots $\kappa + i\boldsymbol{\kappa} \cdot \boldsymbol{\sigma}$, and non-diagonal tunneling to the leads $\Gamma_{12,21} \equiv \gamma \pm i\boldsymbol{\gamma} \cdot \boldsymbol{\sigma}$. Let us write down the Green's function:

$$\check{G}^{-1} = \epsilon - \begin{bmatrix} H_1 & H_{12} \\ H_{12}^\dagger & H_2 \end{bmatrix} \quad (4.30)$$

$$H_{1,2} \equiv E_{1,2} + \mathbf{B}_{1,2} \cdot \boldsymbol{\sigma} - i\Gamma_{1,2}/2 \quad (4.31)$$

$$H_{12} \equiv \kappa + i\boldsymbol{\kappa} \cdot \boldsymbol{\sigma} - i(\gamma + i\boldsymbol{\gamma} \cdot \boldsymbol{\sigma})/2 \quad (4.32)$$

The idea of further transform is that the second dot provides a featureless background for the first dot. To this end, we consider big $E_2, \Gamma_2 \gg \epsilon, B_2, E_1, \Gamma_1$. As to γ, κ , they are assumed to be of an intermediate scale, say $\gamma \approx \sqrt{\Gamma_1 \Gamma_2}$.

We will apply a transform that approximately diagonalises the Green function so that

$$\check{G} = \check{U} \check{G}_d \check{U}^{-1} \quad (4.33)$$

where

$$\check{U} = \sqrt{\frac{1+s}{2s}} \begin{bmatrix} 1 & \eta_+ \\ -\eta_- & 1 \end{bmatrix}; \quad (4.34)$$

$$\check{U}^{-1} = \sqrt{\frac{1+s}{2s}} \begin{bmatrix} 1 & -\eta_+ \\ \eta_- & 1 \end{bmatrix} \quad (4.35)$$

and

$$\eta_{\pm} = \frac{\mu_{\pm}}{1+s}; \quad s \equiv \sqrt{1+\mu_+\mu_-}; \quad (4.36)$$

$$\mu_{\pm} = 2 \frac{k \pm \mathbf{k} \cdot \boldsymbol{\sigma}}{-E_2 + i\Gamma_2/2}; \quad (4.37)$$

$$k, \mathbf{k} \equiv -\kappa + i\gamma/2, -\kappa + i\gamma/2 \quad (4.38)$$

with this, the biggest block of \check{G}_d^{-1} is $-E_2 + i\Gamma_2/2$, while the smallest one reads

$$\epsilon - E_1 + i\Gamma_1/2 - \frac{k^2 + \mathbf{k}^2}{-E_2 + i\Gamma_2/2} \quad (4.39)$$

We rewrite it as

$$\epsilon - E_1 + i\Gamma/2 - \Delta E_1 \quad (4.40)$$

where the actual level width Γ is given by

$$\Gamma = \Gamma_1 + \frac{\Gamma_2 C_{11} - 2E_2 C_{10}}{E_2^2 + \Gamma_2^2/4}; \quad (4.41)$$

$$C_{11} \equiv \kappa^2 - \gamma^2/4 + \mathbf{\kappa}^2 - \boldsymbol{\gamma}^2/4; \quad (4.42)$$

$$C_{10} \equiv \kappa\gamma + \mathbf{\kappa}\boldsymbol{\gamma} \quad (4.43)$$

and we neglect insignificant shift of the level position

$$\Delta E_1 = -\frac{C_{10}\Gamma_2/2 + C_{11}E_2}{E_2^2 + \Gamma_2^2/4} \quad (4.44)$$

The Γ_a matrices are transformed as $\check{\Gamma}^L \rightarrow \check{U}^\dagger \check{\Gamma}^L \check{U}$, $\check{\Gamma}^L \rightarrow \check{U}^{-1\dagger} \check{\Gamma}^L \check{U}^{-1}$.

Keeping terms of the relevant orders only, we obtain

$$\check{\Gamma}^L = \begin{bmatrix} g_L & \Gamma_{12}^{+L} - \eta_-^* \Gamma_2^L \\ \Gamma_{12}^{-L} - \Gamma_2^L \eta_- & \Gamma_2^L \end{bmatrix} \quad (4.45)$$

$$g_L \equiv \Gamma_1^L - \Gamma_{12}^{+L} \eta_- - \eta_-^* \Gamma_{12}^{-L} + \eta_-^* \Gamma_2^L \eta_- \quad (4.46)$$

$$\check{\Gamma}^R = \begin{bmatrix} g_R & \Gamma_{12}^{+R} - \eta_+ \Gamma_2^R \\ \Gamma_{12}^{-R} - \Gamma_2^R \eta_+^* & \Gamma_2^R \end{bmatrix} \quad (4.47)$$

$$g_R \equiv \Gamma_1^R - \Gamma_{12}^{+R} \eta_+^* - \eta_+ \Gamma_{12}^{-R} + \eta_+ \Gamma_2^R \eta_+^* - \quad (4.48)$$

With this, we can summarize the results for the total transmission coefficient T_{tot} (summed over two spin directions). We introduce compact notations that adsorb the energy dependence of the coefficient:

$$G_{\pm} = \frac{1}{\epsilon - E_1 \pm B + i\Gamma/2}; \quad (4.49)$$

$$G_{s,a} = \frac{G_+ \pm G_-}{2}; \quad \bar{G}_i = G_i^* \quad (4.50)$$

and write it down as

$$T_{tot}(E) = 2T_0 + (\Gamma_L \Gamma_R + \Gamma^2)(G_+ \bar{G}_+ + G_- \bar{G}_-) \quad (4.51)$$

$$+ 2((\mathbf{\Gamma} \cdot \mathbf{B})^2/B^2 - \Gamma^2)G_a \bar{G}_a \quad (4.52)$$

$$+ RX(G_+ + G_- + \bar{G}_+ + \bar{G}_-) \quad (4.53)$$

$$- IX \text{Im}(G_+ + G_- - \bar{G}_+ - \bar{G}_-) \quad (4.54)$$

Here, the partial decay rate read $(\Gamma_L + \Gamma_R = \Gamma)$

$$\Gamma_L = \Gamma_1^L + \frac{C_1 \Gamma_2^L - C_3^L \Gamma_2 - 2E_2 C_2^L}{E_2^2 + \Gamma_2^2/4} \quad (4.55)$$

$$C_1 \equiv \kappa^2 + \gamma^2/4 + \kappa^2 + \gamma^2/4 \quad (4.56)$$

$$C_2^L \equiv \kappa \cdot \gamma_L + \gamma_L \kappa \quad (4.57)$$

$$C_3^L \equiv \gamma \cdot \gamma_L + \gamma \gamma_L, \quad (4.58)$$

and similar for R . The spin-orbit interaction is represented by the vector $\mathbf{\Gamma}$,

$$\mathbf{\Gamma} = \frac{E_2 \mathbf{C}_5 + \kappa \mathbf{C}_4 + \mathbf{C}_6 \times \kappa + \kappa \mathbf{C}_6}{E_2^2 + \Gamma_2^2/4} \quad (4.59)$$

$$C_4 = \Gamma_2^L \gamma_R - \Gamma_2^R \gamma_L \quad (4.60)$$

$$\mathbf{C}_5 = \gamma_R \gamma_L - \gamma_L \gamma_R + \gamma_R \times \gamma_L \quad (4.61)$$

$$\mathbf{C}_6 = \Gamma_2^R \gamma_L - \Gamma_2^L \gamma_R \quad (4.62)$$

and the coefficients RX , IX read

$$RX = \frac{1}{E_2^2 + \Gamma_2^2/4} (-E_2 C_7 + \kappa C_8 + \kappa \cdot \mathbf{C}_9 - T_0(E_2 C_{11} + C_{10} \Gamma_2/2)) \quad (4.63)$$

$$IX = \frac{1}{E_2^2 + \Gamma_2^2/4} (-C_7 \Gamma_2/2 + \gamma C_8/2 + \gamma \cdot \mathbf{C}_9/2 - T_0(E_2 C_{10} - C_{11} \Gamma_2/2)) \quad (4.64)$$

$$C_7 = \gamma_R \gamma_L + \gamma_R \cdot \gamma_L \quad (4.65)$$

$$C_8 = \Gamma_2^L \gamma_R + \Gamma_2^R \gamma_L \quad (4.66)$$

$$\mathbf{C}_9 = \gamma_R \Gamma_2^L + \gamma_L \Gamma_2^R \quad (4.67)$$

We will explain the physical significance of each term in Eq. 4.54 in the next Section.

To treat the interaction self-consistently, we also need the average charge and spin in the dot,

$$\langle \hat{d}_\alpha^\dagger \hat{d}_\beta \rangle \equiv n \delta_{\alpha\beta} + \mathbf{n} \cdot \boldsymbol{\sigma} \quad (4.68)$$

This is given by

$$\begin{aligned} \check{n} = \int \frac{d\epsilon}{2\pi} & \check{G}((\Gamma_R + \boldsymbol{\Gamma} \cdot \boldsymbol{\sigma}) f^R(\epsilon) \\ & + (\Gamma_L - \boldsymbol{\Gamma} \cdot \boldsymbol{\sigma}) f^L(\epsilon)) \end{aligned} \quad (4.69)$$

This can be rewritten in more detail as ($\mathbf{b} = \mathbf{B}/B$)

$$\begin{aligned} n &= \int \frac{d\epsilon}{2\pi} ((G_s \bar{G}_s + G_a \bar{G}_a)(\Gamma_R f^R(\epsilon) + \Gamma_L f^L(\epsilon)) \\ &+ (\mathbf{b} \cdot \boldsymbol{\Gamma})(G_a \bar{G}_s + G_s \bar{G}_a)(f^R(\epsilon) - f^L(\epsilon))) \end{aligned} \quad (4.70)$$

$$\begin{aligned} \mathbf{n} &= \int \frac{d\epsilon}{2\pi} (2\mathbf{b}(\mathbf{b} \cdot \boldsymbol{\Gamma}) G_a \bar{G}_a + \boldsymbol{\Gamma}(G_s \bar{G}_s - G_a \bar{G}_a) + \\ &(\mathbf{b} \times \boldsymbol{\Gamma}) i(G_a \bar{G}_s - G_s \bar{G}_a)(f^R(\epsilon) - f^L(\epsilon)) \\ &+ \mathbf{b}(G_a \bar{G}_s + G_s \bar{G}_a)(\Gamma_R f^R(\epsilon) + \Gamma_L f^L(\epsilon))) \end{aligned} \quad (4.71)$$

We substitute filling factors at vanishing temperature $f^{L,R} = \Theta(eV_{L,R} - \epsilon)$ and integrate over ϵ to obtain n, \mathbf{n} and full current. It is also advantageous at this stage to switch to dimensionless variables measuring energy in units of Γ and setting $e = 1$. We introduce convenient functions

$$K_{R,L}^\pm = \frac{1}{2\pi} \text{atan}(2(V_{R,L} - \epsilon_d \pm B)); \quad (4.72)$$

$$L_{R,L}^\pm = \frac{1}{2\pi} \ln(4(V_{R,L} \pm B)^2 + 1); \quad (4.73)$$

$$L^\pm = L_R^\pm - L_L^\pm; \quad K^\pm = K_R^\pm - K_L^\pm. \quad (4.74)$$

With this,

$$\begin{aligned} n &= \sum_{k=L,R} \Gamma_k (1/2 + K_k^+ + K_k^-) \\ &+ (\mathbf{b} \cdot \boldsymbol{\Gamma})(K^+ + K^-), \end{aligned} \quad (4.75)$$

$$\begin{aligned} \mathbf{n} &= \mathbf{b}(\Gamma_R(K_R^- - K_R^+) + \Gamma_L(K_L^- - K_L^+)) \\ &+ \frac{\boldsymbol{\Gamma}}{1+4B^2} (K^+ + K^- + B(L^- - L^+)) \\ &+ \frac{(\mathbf{b} \times \boldsymbol{\Gamma})}{2(1+4B^2)} (B(K^+ + K^-) + L^+ - L^-) \\ &+ \frac{2\mathbf{b}(\mathbf{b} \cdot \boldsymbol{\Gamma})B}{1+4B^2} (4B(K^+ + K^-) + L^+ - L^-) \end{aligned} \quad (4.76)$$

The self-consistency equations then read:

$$\epsilon_d = Un; \quad \mathbf{B} = \mathbf{B}_0 - U\mathbf{n} \quad (4.77)$$

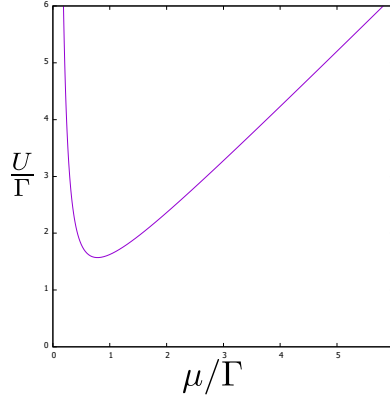


Figure 4.3: The domain of magnetic phase.

\mathbf{B}_0 being the external magnetic field. This equation has to be solved at each $V_{R,L}$. With this solution, we can evaluate the current

$$\begin{aligned}
 I &= T_0(V_L - V_R)/\pi + 2(\Gamma_L\Gamma_R + \Gamma^2)(K^+ + K^-) \\
 &+ 4((\Gamma \cdot \mathbf{b})^2 - \Gamma^2) \frac{B}{1 + 4B^2} \\
 &\times (4B(K^+ + K^-) + L^+ - L^-) \\
 &+ RX(L^+ + L^-) - IX(K^+ + K^-)/2
 \end{aligned} \tag{4.78}$$

Let us elaborate on the equilibrium case $V_R = V_L = \mu$. The terms with spin-orbit interaction do not appear in this case and the self-consistency equations read ($\tilde{K} = K^R = K^L$)

$$\epsilon_d = U(1/2 + \tilde{K}^+ + \tilde{K}^-); \tag{4.79}$$

$$\mathbf{B} = \mathbf{B}_0 - \mathbf{b}U(\tilde{K}_- - \tilde{K}_+) \tag{4.80}$$

We specify to $\mathbf{B}_0 = 0$ and determine the boundary of spontaneously magnetic phase where $B \rightarrow 0$. In this limit,

$$\tilde{K}_- - \tilde{K}_+ \rightarrow -B \frac{2}{\pi} \frac{1}{1 + 4(\mu^*)^2}; \mu^* = \mu - \epsilon_d \tag{4.81}$$

with this, the equations for the boundary read

$$U = (1 + 4(\mu^*)^2) \frac{\pi}{2}; \tag{4.82}$$

$$\mu = \mu^* + U(1/2 + (1/\pi) \text{atan}(2\mu^*)) \tag{4.83}$$

An implicit plot is given in Fig 4.3. The splitting occurs above critical value $U_c = \pi/2$, at large U the magnetic phase occurs in the interval $\mu = (0, U)$ as it should be.

4.7. NORMAL TRANSPORT EXAMPLES

In this Section, we will analyse the peculiarities of normal transport in the model at hand. We restrict ourselves to zero-voltage conductance and non-interacting case where zero-voltage conductance is simply given by T_{tot} at ϵ corresponding to Fermi level,

$$G(V_g) = \frac{G_Q}{2} T_{tot}(\epsilon = E_F). \quad (4.84)$$

Since E_1 is a linear function of the gate voltage, and shift of ϵ in Eq. 4.54 is equivalent to the shift of E_1 , the energy dependence of T_{tot} directly gives the gate voltage dependence of the conductance. The conductance with interaction is qualitatively similar to the non-interacting one since the main effect of interaction in our model is the spin-splitting corresponding to $B \simeq U$.

Let us explain the physical significance of the terms in Eq. 4.54. All spin-orbit effects are incorporated into a single vector $\mathbf{\Gamma}$ in the spin space. To start with, let us neglect the spin-orbit interaction setting $\mathbf{\Gamma} = 0$, so we can disregard the third term. In this case, T_{tot} is contributed independently by spin orientations \pm with respect to \mathbf{B} . Their contributions are shifted by $2B$ in energy.

The first term in Eq. 4.54 gives the featureless transmission of the transport channel and asymptotic value of the conductance at $|E_1| \gg \Gamma$. The second term describes the resonant transmission via the localized state and would show up even if there is no interference between the transmissions through the channel and the localized state. It gives rise to a Lorentzian peak - resonant transmission - of the width $\simeq \Gamma$ in conductance that splits into two at sufficiently big spin splitting $\simeq \Gamma$. Let us bring the fifth term into consideration. Since $G - \bar{G} = -i\Gamma G \bar{G}$ its energy dependence is identical to the second one. However, it usually gives a negative contribution to transmission describing destructive interference of the transmissions in the dot and in the channel - resonant reflection.

The fourth term describes the celebrated Fano effect coming about the interference of the resonant and featureless transmission. It is visually manifested as asymmetry of otherwise Lorentzian peaks or dips. The antisymmetric Fano tail $\propto \epsilon^{-1}$ at large distances from the peak/dip centre beats Lorentzian tail $\propto \epsilon^{-2}$. All these terms are hardly affected by spin-orbit interaction, while the second one manifests it fully. It mixes up spin channels and makes conductance to depend on the orientation of \mathbf{B} with respect to $\mathbf{\Gamma}$.

We illustrate the possible forms of the conductance energy/gate-voltage dependence with the plots in Fig. 4.4 for 4 settings of the parameters $\Gamma_2^{L,R}, E_2, \kappa, \mathbf{\kappa}, \gamma_{L,R}, \mathbf{\gamma}_{L,R}$. Owing to separation of the scales assumed, the relevant parameters $\Gamma_{L,R}, \mathbf{\Gamma}, RX, IX$ are invariant with respect to rescale with the factor A ,

$$\Gamma_2^{L,R}, E_2 \rightarrow A(\Gamma_2^{L,R}, E_2) \quad (4.85)$$

$$\kappa, \mathbf{\kappa}, \gamma_{L,R}, \mathbf{\gamma}_{L,R} \rightarrow \sqrt{A}(\kappa, \mathbf{\kappa}, \gamma_{L,R}, \mathbf{\gamma}_{L,R}). \quad (4.86)$$

For all settings, energy is in units of the resulting Γ . For each setting, we give the plots at $B = 0$ and $B = 2\Gamma$, the latter to achieve a visible separation of resonant peculiarities. Spin-orbit interaction is weak except the last setting where we give separate plots for $\mathbf{B} \parallel \mathbf{\Gamma}$ and $\mathbf{B} \perp \mathbf{\Gamma}$.

For Fig. 4.4 a we choose $\Gamma_2^L, \Gamma_2^R, E_2 = A(0.2, 0.8, 0.5)$, $\kappa, \gamma_L, \gamma_R = \sqrt{A}(0.5, 0.2, 0.2)$, $\Gamma_1^L, \Gamma_1^R = 1.6, 3.5$. We also specify small but finite spin-orbit terms yet they hardly affect the conductance.

In this case, the transmission through the localized state is faster than the interference with the transmission in the channel. This results in a resonant reflection peak at $B = 0$ that splits into two upon increasing the magnetic field. A little Fano asymmetry can be noticed upon a close look.

For Fig. 4.4 b we choose $\Gamma_2^L, \Gamma_2^R, E_2 = A(0.5, 0.5, 0)$, $\kappa, \gamma_L, \gamma_R = \sqrt{A}(3.5, 0.2, 0.2)$, $\Gamma_1^L, \Gamma_1^R = 0.5, 0.5$. The transmission trough the channel is ideal, $T_0 = 1$, the localized state is connected to the channel better than to the leads. This results in a pronounced resonant reflection dip at $B = 0$ that also splits into two upon increasing the magnetic field.

For Fig. 4.4 c we choose $\Gamma_2^L, \Gamma_2^R, E_2 = A(0.2, 1.5, 0)$, $\kappa, \gamma_L, \gamma_R = \sqrt{A}(1.5, 0.3, 0.1)$, $\Gamma_1^L, \Gamma_1^R = 0.8, 0.1$. This choice is such that the competing processes of resonant transmission and reflection almost compensate each other so the resulting resonance peculiarity assumes almost antisymmetric Fano shape. The separation of the peculiarities upon the spin splitting is less pronounced than in the previous examples owing to long-range Fano tails mentioned.

We illustrate the effect of strong spin-orbit interaction in Fig. 4.4 d. We choose $\Gamma_2^L, \Gamma_2^R, E_2 = A(0.2, 0.8, 0.5)$, $\kappa, \gamma_L, \gamma_R = \sqrt{A}(0.5, 0.2, 0.2)$, $\Gamma_1^L, \Gamma_1^R = 1.6, 3.5$. As to spin-dependent parameters, we choose $\kappa = \sqrt{A}SO[0, 0.2, -0.6]$, $\gamma_L = \sqrt{A}SO[0.3, 0, 0]$, $\gamma_R = \sqrt{A}SO[0.0, 0, 1]$ and set the coefficient SO to 1.6, this is its maximal value that satisfies the positivity conditions imposed on the matrices of the rates. The peculiarity at $B = 0$ is a peak with a noticeable Fano addition. It splits at $B = 2\Gamma$ changing its shape, that is different for $\mathbf{B} \parallel \Gamma$ and $\mathbf{B} \perp \Gamma$ as well as for positive and negative energies. Note that owing to Onsager symmetry $G(\mathbf{B}) = G(-\mathbf{B})$.

We also provide an example with interaction implementing the self-consistent scheme described in the previous Section (Fig. 4.5). For this example, we choose $\Gamma_2^L, \Gamma_2^R, E_2 = A(0.2, 1.5, -15)$, $\kappa, \gamma_L, \gamma_R = \sqrt{A}(0.8, 0.1, 0.1)$, $\Gamma_1^L, \Gamma_1^R = 1.1, 0.9$. This choice corresponds to very low channel transmission ($T_0 = 10^{-3}$). The average number of electrons in the dot is presented in Fig. 4.5a as a function of E_1 for several interaction strengths, at zero voltage difference and magnetic field. All curves change from full occupation at big negative E_1 to zero occupation big positive E_1 . At $U = 0$ and $U = \Gamma$ the curves are smooth with no spontaneous spin splitting emerging throught the whole interval of E_1 . For higher interaction strengths, there is an interval of E_1 where the spontaneous splitting is present. The ends of this interval are in principle manifested by cusps in the curves. Only cusps at the end of the interval close to zero are visible, the cusps at the other end are too small. It might seem that the zero-voltage conductance (Fig. 4.5 b) can be computed from T_{tot} at the parameters \tilde{E}_1, \tilde{B} that solve the self-consistency equation at zero voltage difference. However, this is not so, since these parameters also depend on voltage difference. We compute zero-voltage conductance by numerically differentiating the current (Eq. 4.78) at small voltage differences. At zero interaction, we see a resonant transmission peak. Its height does not reach G_Q because of the asymmetry $\Gamma_R \neq \Gamma_L$. At $U = \Gamma$, there is still a single peak. At higher U we see the splitting of the peak. The height of the peaks split is a half of the height of the original peak if they are sufficiently separated. As we have conjectured earlier, this is qualitatively similar to the conductance traces where spin splitting is induced by the magnetic field.

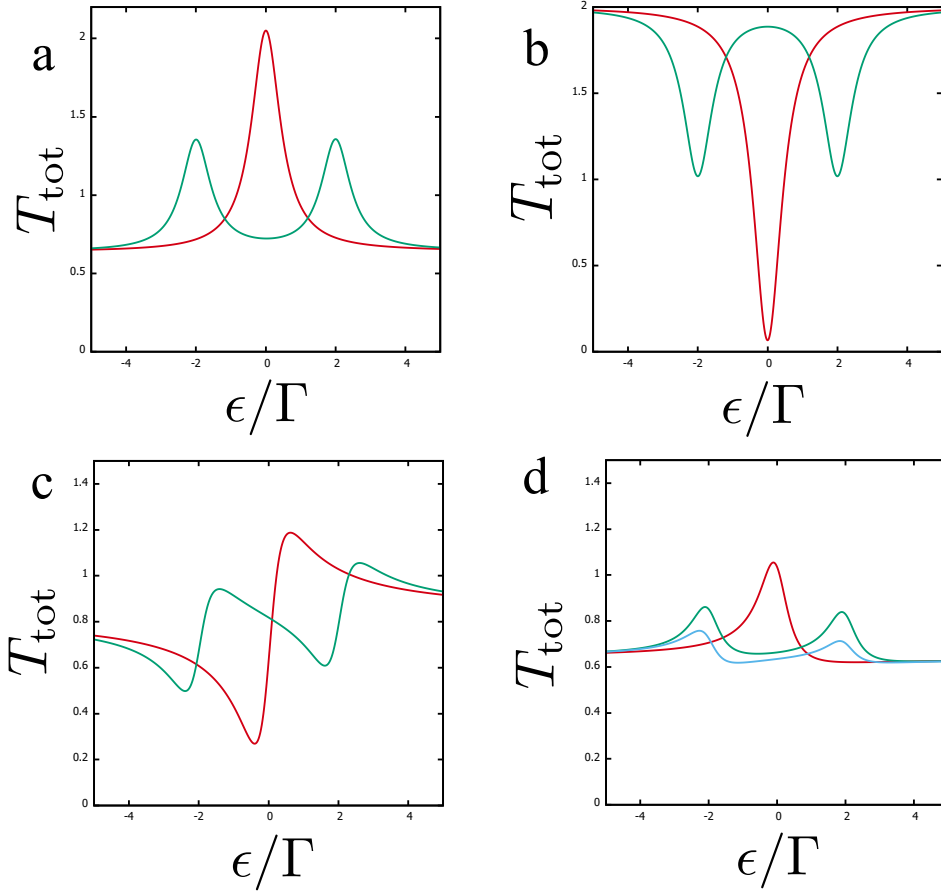


Figure 4.4: Examples of normal transport. The energy dependence of T_{tot} is the same as the conductance dependence on the gate voltage. Red curves correspond to $B = 0$, green curves to $B = 2\Gamma$. a. Basic example: resonant transmission b. Dip: resonant reflection c. Fano. d. Strong spin-orbit. Here, green (blue) curve is for parallel (perpendicular) orientation of \mathbf{B} with respect to Γ .

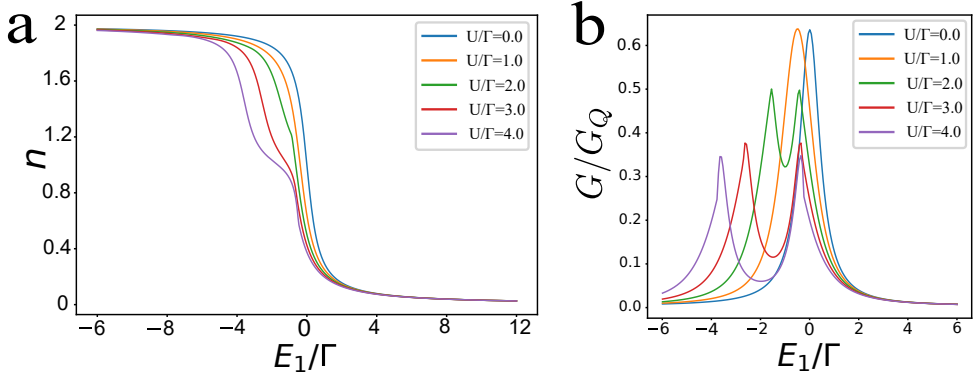


Figure 4.5: Example of normal transport with interaction. Resonant transmission regime, no magnetic field, no SO coupling. The setup parameters are given in the text. a. The average number of electrons in the localized state versus E_1 at various interaction strengths. b. Zero-voltage conductance versus E_1 at various interaction strengths.

4.8. SUPERCONDUCTING TRANSPORT

In this Section, we elaborate on the description of superconducting transport in our model. Since supercurrent is a property of the ground state of the system, it is convenient to work with electron Green functions in imaginary time and introduce Nambu structure. Let us start, as we did previously, with an arbitrary number of dots and superconducting leads. If we neglect tunnel couplings, the inverse Green function $\check{\mathcal{H}}(\epsilon)$ is a matrix in the space of the dots, spin and Nambu and reads:

$$\check{\mathcal{H}} = i\epsilon\tau_z - \check{H}. \quad (4.87)$$

The tunnel couplings to the leads labelled by a add the self-energy part

$$\check{\mathcal{H}} = i\epsilon\tau_z - \check{H} + \frac{i}{2} \sum_a \check{\Gamma}_a \check{Q}_a \quad (4.88)$$

where $\check{\Gamma}_a$ are given by Eq. 4.19 and the matrix \check{Q}_a is a matrix in Nambu space reflecting the properties of the superconducting lead a ,

$$Q_a = \frac{1}{\sqrt{\epsilon^2 + \Delta_a^2}} \begin{bmatrix} \epsilon & \Delta_a e^{i\phi_a} \\ \Delta_a e^{-i\phi_a} & -\epsilon \end{bmatrix}, \quad (4.89)$$

$$Q_a^2 = 1.$$

To find supercurrents, we need to evaluate the total energy and take its derivatives with respect to the phase differences. Since that are dots that connect the leads with different phase, the phase-dependent energy is the energy of the dots. The latter can be expressed as

$$\mathcal{E} = -\frac{1}{2} \int \frac{d\epsilon}{2\pi} \ln \det(\check{\mathcal{H}}) \quad (4.90)$$

To see how does this work, let us check this formula neglecting tunnel couplings. With this, the energy is the sum over eigenvalues of \check{H} , E_n ,

$$\mathcal{E} = -\frac{1}{2} \int \frac{d\epsilon}{2\pi} \ln(\epsilon^2 + E_n^2) \quad (4.91)$$

The integral formally diverges at $\epsilon \rightarrow \infty$. To regularize it, we subtract its value at $E_n = 0$ to obtain

$$\mathcal{E} = -\sum_n \frac{|E_n|}{2} + \text{const} \quad (4.92)$$

To recover a familiar formula, we shift the constant by $\text{Tr}(\check{H})/2$,

$$\mathcal{E} = -\sum_n \frac{|E_n|}{2} + \sum_n \frac{E_n}{2} + \text{const} = \quad (4.93)$$

$$\sum_n E_n \Theta(-E_n) + \text{const}, \quad (4.94)$$

so it becomes the energy of the filled states (those with $E_n < 0$). This suggest we need to handle the integral with care keeping eye on possible problems at big ϵ . Fortunately, no special care has to be taken for the phase-dependent energy since it is accumulated at superconducting gap scale $\epsilon \simeq \Delta$. We have to be careful when expressing the occupation of the dots in terms of derivatives of \mathcal{E} with respect to dot energies (as we do for numerical calculations). For instance, the average occupation of the dot 1 reads

$$\langle \hat{n}_1 \rangle = \frac{\partial \mathcal{E}}{\partial E_1} + 1, \quad (4.95)$$

the last term correcting for high-energy divergences.

For our starting two-dot, two-lead model, the inverse Green function reads (c.f. with Eq. 4.30).

$$\mathcal{H} = \begin{bmatrix} \mathcal{H}_{11} & \mathcal{H}_{12} \\ \mathcal{H}_{21} & \mathcal{H}_{22} \end{bmatrix} \quad (4.96)$$

, where

$$\begin{aligned} \mathcal{H}_{11} &= i\epsilon\tau_z - E_1 - (\mathbf{B}_1 \cdot \check{\boldsymbol{\sigma}})\tau_z \\ &+ \frac{i}{2}(\Gamma_1^R \check{Q}_R + \Gamma_1^L \check{Q}_L), \end{aligned} \quad (4.97)$$

$$\begin{aligned} \mathcal{H}_{22} &= i\epsilon\tau_z - E_2 - (\mathbf{B}_1 \cdot \check{\boldsymbol{\sigma}})\tau_z \\ &+ \frac{i}{2}(\Gamma_2^R \check{Q}_R + \Gamma_2^L \check{Q}_L), \end{aligned} \quad (4.98)$$

$$\mathcal{H}_{12} = -\check{\kappa} + \frac{i}{2}\{\check{\gamma}_L \check{Q}_L + \check{\gamma}_R \check{Q}_R\}, \quad (4.99)$$

$$\mathcal{H}_{21} = -\check{\kappa}^\dagger + \frac{i}{2}\{\check{\gamma}_L^\dagger \check{Q}_L + \check{\gamma}_R^\dagger \check{Q}_R\}, \quad (4.100)$$

and we turn back to the compact notations

$$\check{\kappa}, \check{\kappa}^\dagger = \kappa \pm i\boldsymbol{\kappa} \cdot \boldsymbol{\sigma} \quad (4.101)$$

$$\check{\gamma}_{L,R}, \check{\gamma}_{L,R}^\dagger = \gamma_{L,R} \pm i\boldsymbol{\gamma}_{L,R} \cdot \boldsymbol{\sigma} \quad (4.102)$$

and made use of Q matrices corresponding to two leads

$$\check{Q}_{L,R} = \frac{1}{\sqrt{\epsilon^2 + \Delta^2}} \begin{bmatrix} \epsilon & \Delta e^{i\phi_{L,R}} \\ \Delta e^{-i\phi_{L,R}} & -\epsilon \end{bmatrix}. \quad (4.103)$$

Next goal is to reduce the number of parameters implementing the separation of scales mentioned and implemented for the normal transport. This is achieved by the following transformation of the determinant

$$\begin{aligned} \ln \det(\check{\mathcal{H}}) &= \ln \det(\check{\mathcal{H}}_{11} - \check{\mathcal{H}}_{12} \check{\mathcal{H}}_{22}^{-1} \check{\mathcal{H}}_{21}) \\ &\quad + \ln \det(\check{\mathcal{H}}_{22}) \end{aligned} \quad (4.104)$$

and implementing $E_2, \Gamma_2 \gg \gamma, \kappa \gg \epsilon, B_2, E_1, \Gamma_1$.

Let us first evaluate $\det(\check{\mathcal{H}}_{22})$, which is that of a 4×4 matrix with spin structure taken into account. Since we may assume $\epsilon, B_2 \ll \Gamma_2, E_2$ the spin structure is trivial and the answer reads

$$\begin{aligned} \ln \det(\check{\mathcal{H}}_{22}) &= 2 \ln \left(E_2^2 + \frac{1}{4} \Gamma_2^2 \right) + \\ &\quad 2 \ln \left(1 - T_0 \frac{\Delta^2}{\Delta^2 + \epsilon^2} \sin^2 \phi/2 \right), \end{aligned} \quad (4.105)$$

where, as previously, we define $\Gamma_2 = \Gamma_2^L + \Gamma_2^R$ and $T_0 = \Gamma_2^L \Gamma_2^R / (E_2^2 + \frac{1}{4} \Gamma_2^2)$.

The energies of Andreev levels are determined from zeros of this determinant. We recover the well-known expression for the energy of the spin-degenerate Andreev level in a contact with transparency T_0 ,

$$E_{Andr} = \Delta \sqrt{1 - T_0 \sin^2(\phi/2)} \quad (4.106)$$

The integration of the log of the determinant over the energy gives the expected result for the energy of the ground state,

$$\mathcal{E} = -E_{Andr} \quad (4.107)$$

Let us turn to evaluation of the rest of the expression. We note that

$$\check{\mathcal{H}}_{22}^{-1} = - \frac{E_2 + \frac{i}{2} (\Gamma_{2R} \check{Q}_R + \Gamma_{2L} \check{Q}_L)}{\left(E_2^2 + \frac{\Gamma_2^2}{4} \right) (1 - T_0 s)} \quad (4.108)$$

where we have introduced a convenient compact notation

$$s \equiv \frac{\Delta}{\sqrt{\Delta^2 + \epsilon^2}} \sin^2(\phi/2) \quad (4.109)$$

The matrix in the first determinant thus contains a factor $(1 - T_0 s)$ in the denominator. Multiplying with this factor cancels $\det(\check{\mathcal{H}}_2)$ so the whole expression can be reduced to the following relatively simple form

$$\ln \det(\check{\mathcal{H}}) = \quad (4.110)$$

$$\ln \det((1 - T_0 s)(i\epsilon\tau_z - E_1 - (\mathbf{B} \cdot \check{\boldsymbol{\sigma}})\tau_z) + \Delta E + s\Delta E_S) \quad (4.111)$$

$$+ \frac{i}{2}(\Gamma^R(s)\check{Q}_R + \Gamma^L(s)\check{Q}_L) + \frac{i}{4}\mathbf{\Gamma} \cdot \check{\boldsymbol{\sigma}}(\check{Q}_L\check{Q}_R - \check{Q}_R\check{Q}_L), \quad (4.112)$$

where

$$\Gamma^{L,R}(s) = \Gamma^{L,R} + s\Gamma_S^{L,R}. \quad (4.113)$$

The parameters $\Gamma_{L,R}$, ΔE , $\mathbf{\Gamma}$ have been already defined in our consideration of normal transport. The compact description of superconducting transport brings three additional parameters

$$\Delta E_S = \frac{-E_2 C_7 + \kappa C_8 + \boldsymbol{\kappa} \cdot \mathbf{C}_9}{E_2^2 + \Gamma_2^2/4} \quad (4.114)$$

$$\Gamma_S^L = -T_0 \Gamma_1^L + \frac{\Gamma_R(\gamma_L^2 + \boldsymbol{\gamma}_L^2)}{E_2^2 + \Gamma_2^2/4} \quad (4.115)$$

$$\Gamma_S^R = -T_0 \Gamma_1^R + \frac{\Gamma_L(\gamma_R^2 + \boldsymbol{\gamma}_R^2)}{E_2^2 + \Gamma_2^2/4}. \quad (4.116)$$

Here, ΔE_S is a part of the expression (4.63) for RX but is an independent parameter.

Since both normal and superconducting transport originate from the same scattering matrix, there are many examples when the parameters characterizing the superconducting transport can be directly determined from the results of normal transport measurements, a single channel with transparency T_0 being the simplest one. The presence of the additional parameters ΔE_S , $\Gamma_S^{L,R}$ is therefore rather disappointing: we cannot predict superconducting transport exclusively from the results of normal transport measurements and have to rely on model assumptions.

Let us outline the physical meaning of the overall structure of the expression (4.110). The first term is a product of the terms whose zeros give the Andreev level in the transport channel and energy level in an isolated localized state, the product indicate that these levels are independent. The rest of the terms thus describe the hybridization of these levels. Note that the terms with ΔE cannot be cancelled by a shift of E_1 , so in distinction from the normal case, are active in the presence of superconductivity. The terms with $\Gamma(s)$ are similar to tunnel decay terms in Eq. 4.97, in distinction from normal case the presence of the second dot does not just renormalize Γ . The last term describes spin-orbit effect and is proportional to the same vector $\mathbf{\Gamma}$ as in the normal case. In distinction from all other terms, it is odd in the phase difference since it is proportional to the commutator of two \check{Q} . The combination of this term and that with magnetic field results in a shift of the minimum of superconducting current from 0 or π positions.

4.9. NUMERICAL DETAILS

In this Section, we provide the overall strategy and details of our numerical calculations.

We postpone the discussion of self-consistency assuming that we already know E_1 and B . To find the phase-dependent energy, we have to integrate the log of the determinant over ϵ . We compute directly the determinant of 8×8 matrices implementing the difference of scales numerically. For quick computation at each energy, we represent the matrix $\tilde{\mathcal{H}}$ as a sum over various scalar functions of ϵ ,

$$\tilde{\mathcal{H}} = \tilde{A} + \epsilon \tilde{B} + \frac{\epsilon}{\sqrt{\epsilon^2 + \Delta^2}} \tilde{C} + \frac{\Delta}{\sqrt{\epsilon^2 + \Delta^2}} \tilde{D}(\phi_L, \phi_R) \quad (4.117)$$

where the matrices $\tilde{A} - \tilde{D}$ do not depend on ϵ and only \tilde{D} depends on the superconducting phase. We define the function of ϵ as

Although in our model the phase-dependent energy is not a minus half-sum of ABS energies as it would be for energy-independent transmission, we can use this sum for qualitative estimations. With this, the half-sum of the first and second energies would result in an inverted supercurrent, but the half-sum of the third and fourth states, that is, the contribution of the transport channel, adds to the balance a usual supercurrent of slightly bigger amplitude.

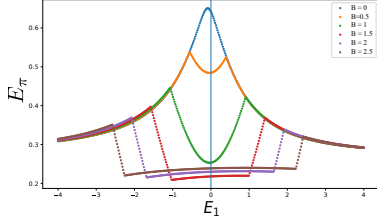
Example B. (Fig. 4.7) This inspired us to check if the $0 - \pi$ transitions can be achieved at very low transmission of the transport channel. We have taken the following set of parameters $\Gamma_2^L, \Gamma_2^R, E_2 = A(0.2, 1.5, -15)$, $\kappa, \gamma_L, \gamma_R = \sqrt{A}(0.8, 0.1, 0.1)$, $\Gamma_1^L, \Gamma_1^R = 1.1, 0.91$. For this choice, $T_0 \simeq 10^{-3}$, $\Gamma_L = 1.1, \Gamma_R = 0.91, \Gamma = 2.03$. The normal conductance traces (Fig. 4.7d) show a classical scenario of resonant transmission that saturates to almost zero far from the resonance.

The check was successful. We plot the traces of $E_T \equiv E_T(\phi = \pi) - E_T(\phi = 0)$ for various magnetic fields in Fig. 4.7a. The traces look like those in Fig. 4.6a except the shift downwards by $\simeq 0.25$. Owing to this, E_T is negative for $B > 0.8$ in an interval of gate voltages that increases with B , $0 - \pi$ transitions are at the ends of the interval.

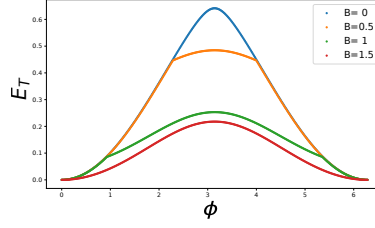
We plot the phase dependence of the supercurrent for $|B| = 2$ and various E_1 in Fig. 4.7b. The $0 - \pi$ transitions at this field take place at $E_1 \approx \pm 1.25$. In accordance with this, the almost sinusoidal curves at $E_1 = -2.5, 2$ are of positive amplitude while those at $E_1 = 0, -1$ are of negative one. Note a rather low value $\simeq 0.02$ of the maximum "negative" current, almost 25 times smaller than the maximum value of the current in a single transport channel. An interesting curve is found close to the transition, at $E_1 = -1.5$. Here, the current jumps between sin-like curves of positive and negative amplitude. The total integral of the current between 0 and π is still positive, so $E_\pi > 0$.

An example of the phase dependence of ABS energies is given in Fig. 4.7c. Since the transmission of the channel is very low, we see only two spin-split ABS. The upper one is close to the gap edge, and eventually merges with continuous spectrum at $\phi \approx 0.6, 2\pi - 0.6$. The lower one is close to zero, and exhibits two zero crossings at $\phi \approx \pi \pm 0.65$ corresponding to the discontinuities in corresponding curve in Fig. 4.7b.

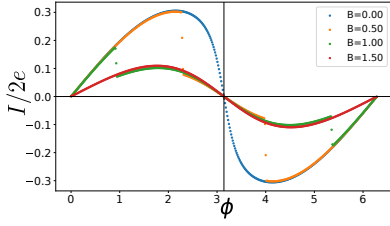
Example C. (Figs. 4.8, 4.9) In this example, we illustrate the effect of SO coupling on the superconducting transport. We choose $\Gamma_2^L, \Gamma_2^R, E_2 = A(1.2, 1.5, -1)$, $\kappa, \gamma_L, \gamma_R = \sqrt{A}(0.2, 0.6, 0.2)$, $\Gamma_1^L, \Gamma_1^R = 1.6, 3.5$. As to spin-dependent parameters, we choose $\kappa = \sqrt{A}SO[0, 0.8, 0]$, $\gamma_L = \sqrt{A}SO[0, 0.2, 0]$, $\gamma_R = \sqrt{A}SO[0, 0.1, 0]$ with $SO = 1$ that gives $T_0 = 0.64, \Gamma_L = 1.1, \Gamma_R =$



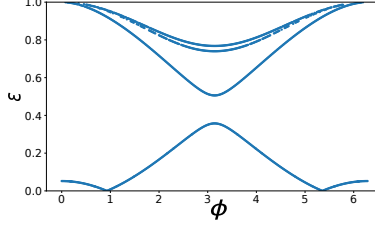
(a) $E_\pi \equiv E_T(\phi = \pi) - E_T(\phi = 0)$ versus E_1 at several values of magnetic field.



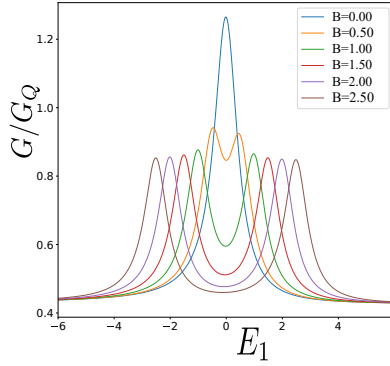
(b) The phase-dependent part of energy $E_T \equiv E_T(\phi) - E_T(\phi = 0)$ at $E_1 = 0$ and several values of magnetic field.



(c) The phase dependence of the superconducting current at $E_1 = 0$ for several values of B .



(d) The phase dependence of ABS energies at $E_1 = 0$ and at $|B| = 1$.



(e) Normal zero-voltage conductance versus E_1 at several values of magnetic field.

Figure 4.6: Example A. Resonant transmission, moderate channel transmission. No SO coupling.

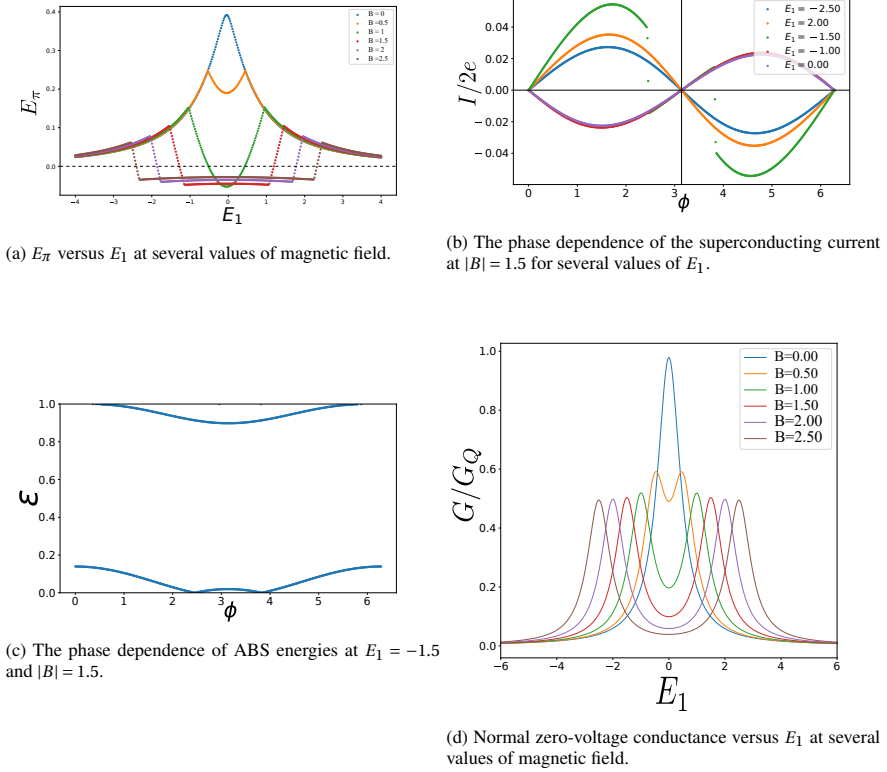


Figure 4.7: Example B. Resonant transmission, low channel transmission. No SO coupling. A pair of $0 - \pi$ transitions occurs at $|B| > 0$.

1.38, $\Gamma = 2.48$ and a significant $\Gamma = 0.45\gamma$. As we see from the Figs. 4.8d, 4.9d that give the traces of normal conductance, this set also illustrates a well-developed Fano resonance with antisymmetric features split in sufficiently high magnetic field.

We consider first $\mathbf{B} \perp \mathbf{\Gamma}$. In this case, the time-reversibility provides the symmetry $\phi \leftrightarrow -\phi$ that was present in all previous plots. Let us concentrate at the $0 - \pi$ energy difference (Fig. 4.8a). The curve at zero magnetic field qualitatively follows the normal conductance. Upon increasing the magnetic field we see the multiple cusps that are already familiar from Figs. 4.6, 4.7 and indicate the spin splitting and eventual zero crossing of ABS. The shape of the trace becomes more complex, and the minimum E_T becomes smaller. However, it does not reach zero that is necessary for $0 - \pi$ transition.

The phase dependence of superconducting current at $B = 2$ and various E_1 is presented in Fig. 4.8b. Most curves display pronounced discontinuities manifesting the zero crossings at corresponding phases. Except for this, the dependence is rather sinusoidal corresponding to moderate transmission. It looks like the current jumps between two sin-like curves of different amplitudes.

It is interesting to see 3 ABS in the plot presenting the phase dependence of ABS energies for $E_1 = -1.5$ and $B = 2$ (Fig. 4.8c). The fourth state is either shifted over the gap edge to the continuous spectrum or is present very close to the edge so we cannot resolve it with accuracy of our numerics. The lowest state displays the familiar zero crossings corresponding to the current jumps.

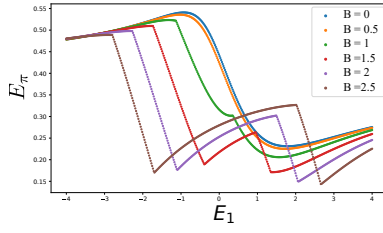
When we change from perpendicular to parallel field (Fig. 4.9) we do not see much change in normal conductance: the difference between the corresponding traces in Figs. 4.9d and 4.8d does not exceed 10 %. This is explained by the fact that the effect is of the second order in Γ , $\propto \Gamma^2/\Gamma^2$, and $|\Gamma|/\Gamma \simeq 0.2$ is not so big. We also do not see much changes in E_T traces (Fig. 4.8a versus Fig. 4.9a).

The most prominent effect of SO coupling is the breaking of $\phi \leftrightarrow -\phi$ symmetry in magnetic field, the effect $\propto |\Gamma|/\Gamma$ at $B \simeq \Gamma$. We see this in Fig. 4.9b where the current-phase dependencies for $B = 2$ are now shifted sin-like curves with jumps. The values of the shift vary from trace to trace, also in sign, and are $\simeq 0.2 - 0.3$. In addition to the shifts of the sin-like curves, the positions of jumps are shifted non-symmetrically, these shifts are $\simeq 0 - 0.5$.

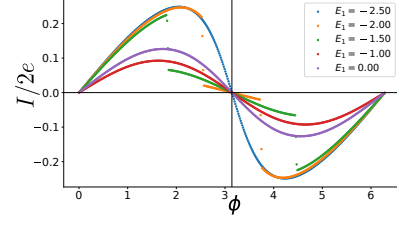
Non-symmetry of the phase dependence of ABS energies is clearly seen in Fig. 4.9c that is done at the same parameters as Fig. 4.8c. Also, beside shift, the energy first ABS is significantly affected by the direction of the magnetic field. A fine detail is the crossing of the second and the third ABS near $\phi \approx 1$. It may seem that in the presence of SO coupling all level crossings shall be avoided, since spin is not a good quantum number. However, since $\mathbf{\Gamma}$ is the only spin vector in our model, for the particular case $\mathbf{B} \parallel \mathbf{\Gamma}$ the projection of spin on \mathbf{B} is a good quantum number and the levels of different projections may cross.

4.10. CONCLUSIONS

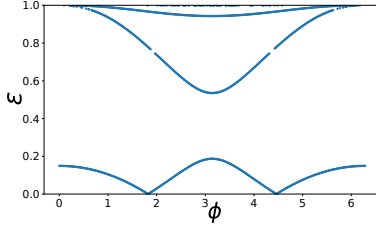
In conclusion, we have formulated a model that accurately describes normal and superconducting transport for a situation where a high transmission in a transport channel is accompanied by propagation through a resonant localized state. The motivation came from experimental observation of a pair of $0 - \pi$ transitions separated by a small interval in the gate voltage. We have presented several examples those by no means exhaust the rich parameter space of



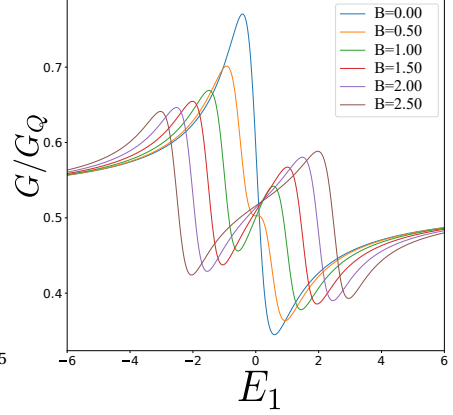
(a) E_π versus E_1 at several values of magnetic field.



(b) The phase dependence of the superconducting current at $B = 2$ for several values of E_1 .



(c) The phase dependence of ABS energies at $E_1 = -1.5$ and $B = 2$.



(d) Normal zero-voltage conductance versus E_1 at several values of magnetic field.

Figure 4.8: Example C. Well-developed Fano features, moderate SO coupling. Magnetic field $\mathbf{B} \perp \mathbf{\Gamma}$

the model. More extensive exploration of this space is required to understand if the model can explain the experimental observation.

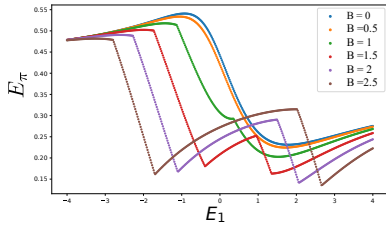
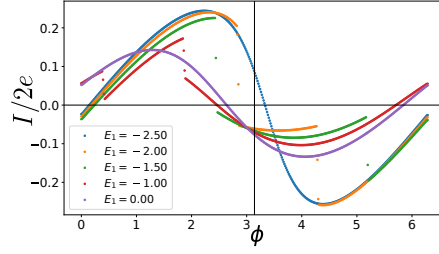
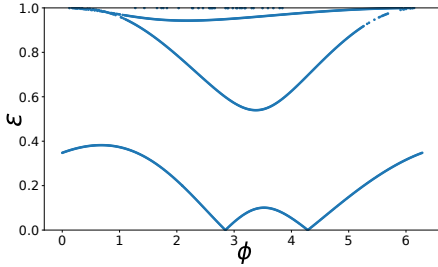
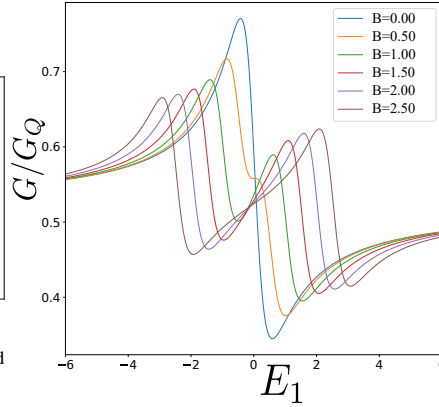
(a) E_π versus E_1 at several values of magnetic field.(b) The phase dependence of the superconducting current at $B = 1.5$ for several values of E_1 .(c) The phase dependence of ABS energies at $E_1 = -2$ and $|B| = 2$.(d) Normal zero-voltage conductance versus E_1 at several values of magnetic field.

Figure 4.9: Example C. Well-developed Fano features, moderate SO coupling. No interaction. Magnetic field $\mathbf{B} \parallel \mathbf{\Gamma}$. Pronounced asymmetry in ϕ .

BIBLIOGRAPHY

- [1] Hristo Barakov and Yuli V. Nazarov. “Supercurrent in the presence of direct transmission and a resonant localized state”. In: *arXiv* (Jan. 2022). eprint: [2201.07848](#). URL: <https://arxiv.org/abs/2201.07848v1>.

5

ABUNDANCE OF WEYL POINTS IN SEMICLASSICAL MULTI-TERMINAL SUPERCONDUCTING NANOSTRUCTURES

*If the doors of perception were cleansed
every thing would appear to man as it is,
Infinite.*

William Blake, The Marriage of Heaven and Hell

This chapter has been published as Abundance of Weyl points in semiclassical multi-terminal superconducting nanostructures [4] and the data is available on https://zenodo.org/record/5806468#.YfuseC8w2_U.

The topological properties of quantum spectra in condensed matter systems got considerable attention in the past decade and are still under active consideration [46, 48, 43, 47]. A large research field that has been formed thereby addresses gapped phases of insulators [18] and superconductors [28] characterized by globally defined topological numbers, and the edge modes [7] at the interfaces separating such phases. In addition to this, the spectra can exhibit topological singularities in the form of level crossings where the topological charge is defined at the singularity rather than globally. The simplest example of such singularity is a Weyl point (WP) [39] corresponding to crossing of two levels in a point in 3D space of parameters. Physical realizations of WPs include special points in the bandstructure of 3D solids [3], spectra of polyatomic molecules [14] and nanomagnets [38], quantum transport systems [23].

The occurrence of WPs have been recently predicted in the spectrum of Andreev bound states (ABS) of generic 4-terminal superconducting nanostructures [30] where the 3D parameter space is formed by three independent superconducting phases of the terminals. Most important WPs are the crossings at *zero energy* that define the topology of the ground state. These WPs in 3D give rise to 2D global Chern numbers that are directly manifested as quantized transconductances of the nanostructure. The ideal periodicity of the space of superconducting phases allows to model higher-dimensional bandstructures with the multi-terminal superconducting nanostructures (MTSN). These ideas resulted in outburst of theoretical [41, 42, 20, 22, 13, 37, 44] and experimental [26, 17, 11, 27, 12] activities in the field of MTSN.

A separate recent development concerned semiclassical MTSN where a big number of ABS form a quasi-continuous spectrum. It has been predicted [25] that this spectrum can be either gapped or gapless depending on specifics of the MTSN and the point in the space of the superconducting phases. A specific topology can be introduced in semiclassical MTSN. It has been discovered and confirmed experimentally [33, 34] that the gapped phases are characterised by topological numbers, and the gapless phase is explained by topological protection of these numbers [45]. The protection-unprotection transition has been discussed in this context [21].

In this Chapter, we analyse the gapless spectrum at the level of discrete states and reveal the abundance of zero-energy topological singularities (Fig. 5.1 c). In 4-terminal structures, those are isolated WPs separated by a typical distance $l_c \simeq (G/G_Q)^{-1/2} \ll 2\pi$. (G is a typical conductance of the nanostructure, $G_Q \equiv e^2/\pi\hbar$). The positions of WPs are random determined by details of electron interference in the structure, while their averaged density and its correlations are determined by the structure design. We relate the density of WPs to the parameter l_c governing the universal parametric correlations [31, 5] in random matrix ensembles, show how to compute this density for concrete nanostructures, investigate the density correlations manifested as the transconductance of the structure, and shortly discuss the opportunities of experimental detection of the WPs in semiclassical MTSN's.

Let us start with qualitative estimations. Given a 4-terminal nanostructure of a typical conductance G one expects $\simeq G/G_Q$, $G_Q \equiv e^2/\pi\hbar$, conduction channels, and, correspondingly, $\simeq G/G_Q$ discrete Andreev bound states affected by superconductivity. This estimation is valid both for "short" nanostructures with the typical size smaller than the superconducting coherence length, where these levels are spread in energy interval Δ , Δ being the superconducting coherence length, and "large" nanostructure where these levels are

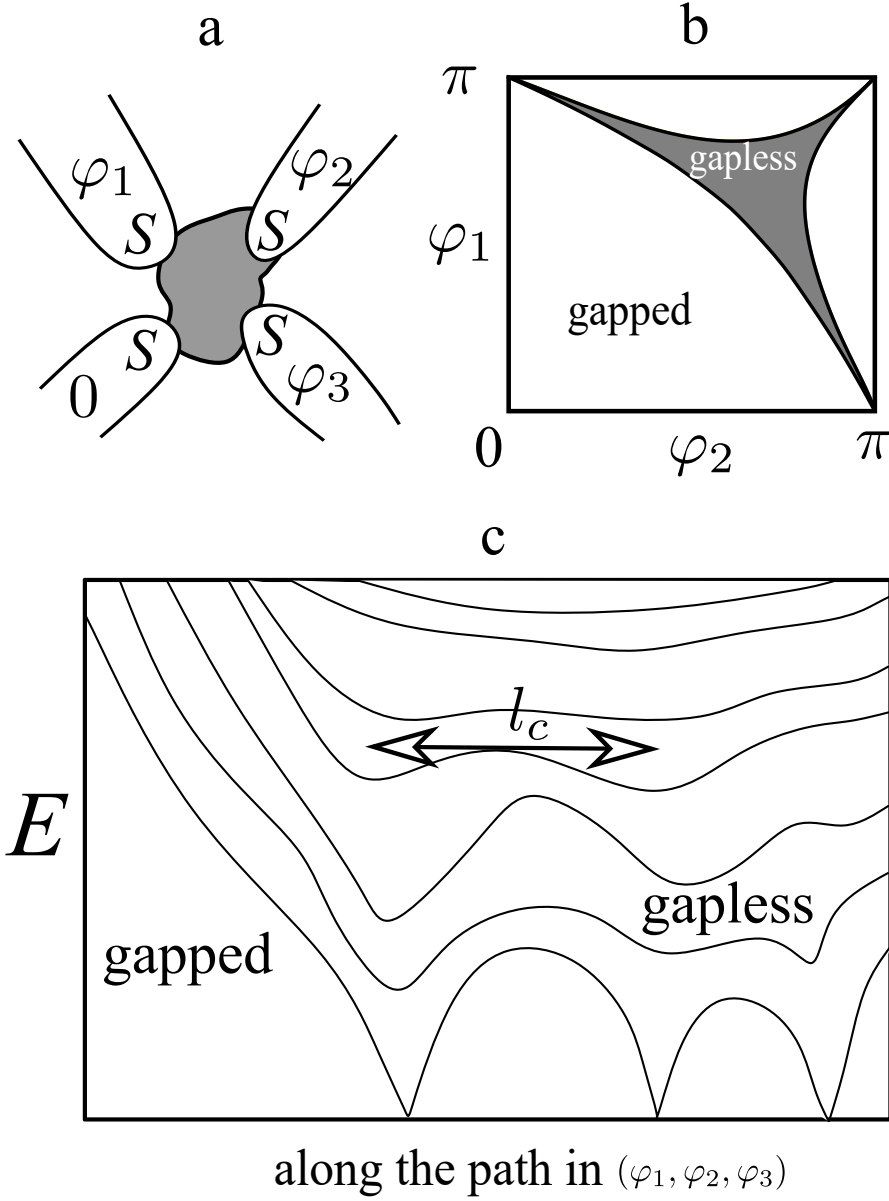


Figure 5.1: Weyl points in semi-classical MTSN. a. 4-terminal semiconducting nanostructure, three independent phases forming a parameter space. b. The domains of gapped and gapless phases at $\varphi_3 = 0$. c. The discrete spectrum near the boundary of gapped and gapless domains plotted along a path in 3D parametric space that goes via the WPs. The distance between the WP's is of the order of the local value of l_c , a parameter governing the universal parametric correlations in the corresponding random matrix ensemble.

concentrated in a much smaller energy interval $E_{\text{Th}} \simeq (G/G_Q)\delta_S$, δ_S being the mean level spacing in the normal state. The energies of these levels depend on the 3 superconducting phases. Owing to periodicity in phases, the spectrum is to be considered in a Brillouin zone (BZ) of the size $\simeq 2\pi$. The RMT of parametric correlations suggests that the level energies wiggle randomly. The energies change at the scale of the level spacing at a typical distance l_c in the parameter space [31, 5]. This distance is determined from comparison of the mean fluctuations of the derivatives of the energies with respect to the parameters and this level spacing. For our situation, the estimation $l_c \simeq \sqrt{G/G_Q}$ in the space of phases holds for both long and short nanostructures. To understand WP's we concentrate on the level that is closest to zero energy. Upon wiggling, it will reach zero at a typical distance of the order of l_c . Therefore, the total number of WP's in the Brillouin zone can be estimated as $N_w \simeq (l_c)^{-3} \simeq (G/G_Q)^{3/2}$.

Our detailed results (See Fig. 5.3) indeed give

$$N_w = A(G/G_Q)^{3/2} \quad (5.1)$$

for the cross-like structures with the arm conductances G where $A = 0.40$ for the ballistic conductor and $A = 0.16$ for the diffusive one. The dimensionless coefficient $A < 1$, this is explained by a rather small fraction of BZ volume taken by the gapless phase (25% for ballistic and 18% for diffusive cross).

As it was shown in [30] the transconductance of the structure is defined by a Chern number of a plane traversing the BZ. The difference of two Chern numbers corresponding to two different planes is given by the total charge of the WP's enclosed between the planes. A naive estimation of the variance of this difference would be the number of WP's enclosed, $\langle\langle(C_1 - C_2)\rangle\rangle \simeq N_w \simeq dl_c^{-3}$, $2\pi \ll d \gg l_c$ being the separation of the planes. This estimation would hold for randomly placed uncorrelated WP's. However, they do correlate similar to ions in an electroneutral gas: a charge of a WP is screened by other points at the distance of the order of their separation, that is, of l_c . Therefore, only WP's at a distance $\simeq l_c$ contribute to the fluctuation of the Chern number and $\langle\langle(C_1 - C_2)\rangle\rangle \simeq l_c^{-2} \simeq (G/G_Q)$. A typical transconductance is thus $\simeq \sqrt{G_Q G}$.

Our quantitative results are obtained in the course of three activities: A. we study numerically a generic RM model to relate the density of WP's to l_c^{-3} and quantify the correlations of WP's. B. we develop a theory to compute $l_c^{-3}(\phi)$ for any MTSN described by the quantum circuit theory [24] and derive concrete expressions for a single-node circuit. C. We find numerically the positions of WP's in the ballistic cross junction (Fig. 3 a) to prove the consistency of the results obtained in the activities A and B. The details of all activities are given in [1].

Activity A. The studies of statistics of spectral crossings have been pioneered by Wilkinson et al. [40, 36, 35]. They introduced a convenient RMT model in a 3D parameter space $\{\phi_i\}$,

$$H(\phi) = \sum_{i=1}^3 (\sin \phi_i X_i + \cos \phi_i Y_i) \quad (5.2)$$

In this model, X_i, Y_i are $2N \times 2N$ random Hermitian matrices with independent normally distributed elements of variance $1/3$, $N \gg 1$. Since we address the WP's in superconducting stuctures at zero energy, in distinction from [40, 36, 35], we choose these random matrices

to obey BdG mirror symmetry of the spectrum (class C [2]). Generally, l_c is defined as $l_c^{-3} = \sqrt{\det\langle\langle v_i v_j \rangle\rangle} / \delta_S^3$, $v_i \equiv \partial E / \partial \phi_i$, δ_S is the mean level spacing at the corresponding energy. For the model in use, $l_c = \pi \sqrt{3/2N}$ conveniently does not depend on ϕ so that the WP density is uniform. We search the positions of WPs by an iterative minimization of the energy of the closest to zero level. To make sure we find all the WPs, we repeat the iteration cycle starting it from a randomly chosen point in the parameter space. We have to do this a number of times that by a factor exceeds the expected number of points. The execution time of the algorithm thus scales as $N^{9/2}$ so we cannot access very large N and work with $N = 40 - 80$. For the WP concentration, we compute

$$N_w / V = (0.83 \pm 0.05) l_c^{-3}. \quad (5.3)$$

This is lower than the concentration of the level crossings in GUE ensemble [36] $(2/3) \sqrt{\pi} l_c^{-3} \approx 1.18 l_c^{-3}$. We reproduce this result searching for the crossings of 10th and 11th levels.

We address the correlator of charges of the WP's, $\langle\langle Q(0)Q(\mathbf{r}) \rangle\rangle$, \mathbf{r} being the vector distance in units of l_c . To enhance the statistics, we have evaluated an equivalent correlator of Berry curvatures of the closest to zero level. The results of 10^5 runs per point are presented in Fig. 5.2 and can be fitted with

$$\langle B^\alpha(0)B^\beta(\mathbf{r}) \rangle = \delta_{\alpha\beta} B(r), \quad r B(r) \approx 10.4 e^{-2.8r - 3.3r^2} \quad (5.4)$$

Since the charge density of WPs is given by the divergence of Berry curvature ([8, 16]),

$$\langle\langle Q(0)Q(\mathbf{r}) \rangle\rangle = (4\pi)^{-2} \nabla^2 B(r), \quad (5.5)$$

see Fig. 5.2 c for the plot. By virtue of electro-neutrality of WP gas, $\int d\mathbf{r} \langle\langle Q(0)Q(\mathbf{r}) \rangle\rangle = -N_w / V$. The fluctuations of Chern number over a surface of the size $\gg l_c$ are governed by $D \equiv -\int d\mathbf{r} r \langle\langle Q(0)Q(\mathbf{r}) \rangle\rangle$,

$$\langle\langle C^2 \rangle\rangle = D \int dS l_c^{-2}(\phi), \quad (5.6)$$

$D \approx 0.5$ from our calculations, dS being an area element of the surface.

Activity B. While there are no perturbative methods to compute the density of WPs directly, they are available for the mesoscopic parametric correlations [32, 15]. With those, one can compute l_c^{-3} for any system characterized by electronic Green functions. We make use of the quantum circuit theory [24] that is a powerful finite-element technique for electronic Green functions. In quantum circuit theory, the structure is subdivided into reservoirs and nodes, the network is formed by connectors of various kinds, for instance, ballistic, tunnel or diffusive. The Green functions are presented by the matrices \hat{G}_a , $\hat{G}^2 = 1$, $\text{Tr} \hat{G} = 0$ defined in the nodes and in the reservoirs. The semiclassical solution is obtained by minimization of an action with respect to \hat{G} in the reservoirs at fixed \hat{G} in the nodes.

The mesoscopic parametric correlations for a general circuit theory have been derived in [9]. For this, one substitutes to the action \hat{G} of double dimension, two diagonal blocks corresponding to the parameter sets 1,2. Near the minimum, the action can be expanded up to quadratic terms with respect to non-diagonal deviations of \check{G} , \check{M} being the matrix characterizing the quadratic expansion. The correlator of mesoscopic fluctuations of the action values at two parameter sets reads [9]

$$\langle\langle \mathcal{S}_1 \mathcal{S}_2 \rangle\rangle = \ln \det' \check{M} \quad (5.7)$$

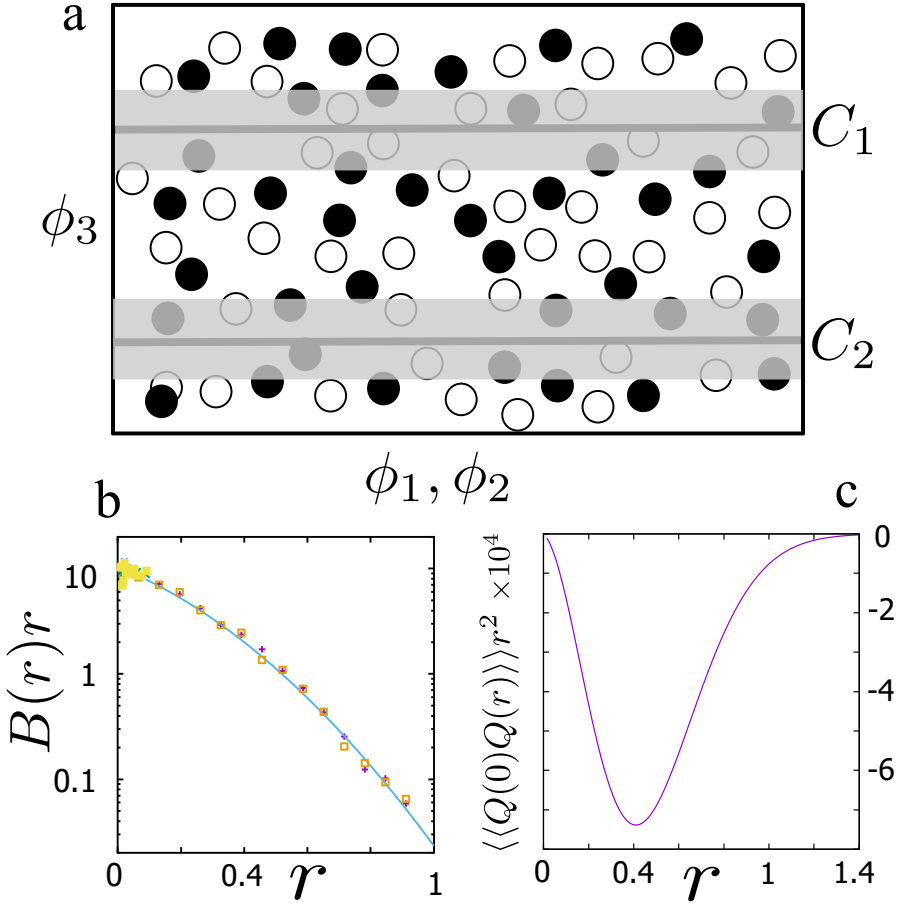


Figure 5.2: Correlations of Weyl points. a. The distribution of WP charge is "electroneutral". Owing to this, the fluctuations of Chern numbers in the planes 1,2 are contributed by WPs at the distance $\simeq l_c$ from the planes (in grey strips). b. The numerical results for the correlator of Berry curvatures and the fit. c. The charge-charge correlator as computed from the fit.

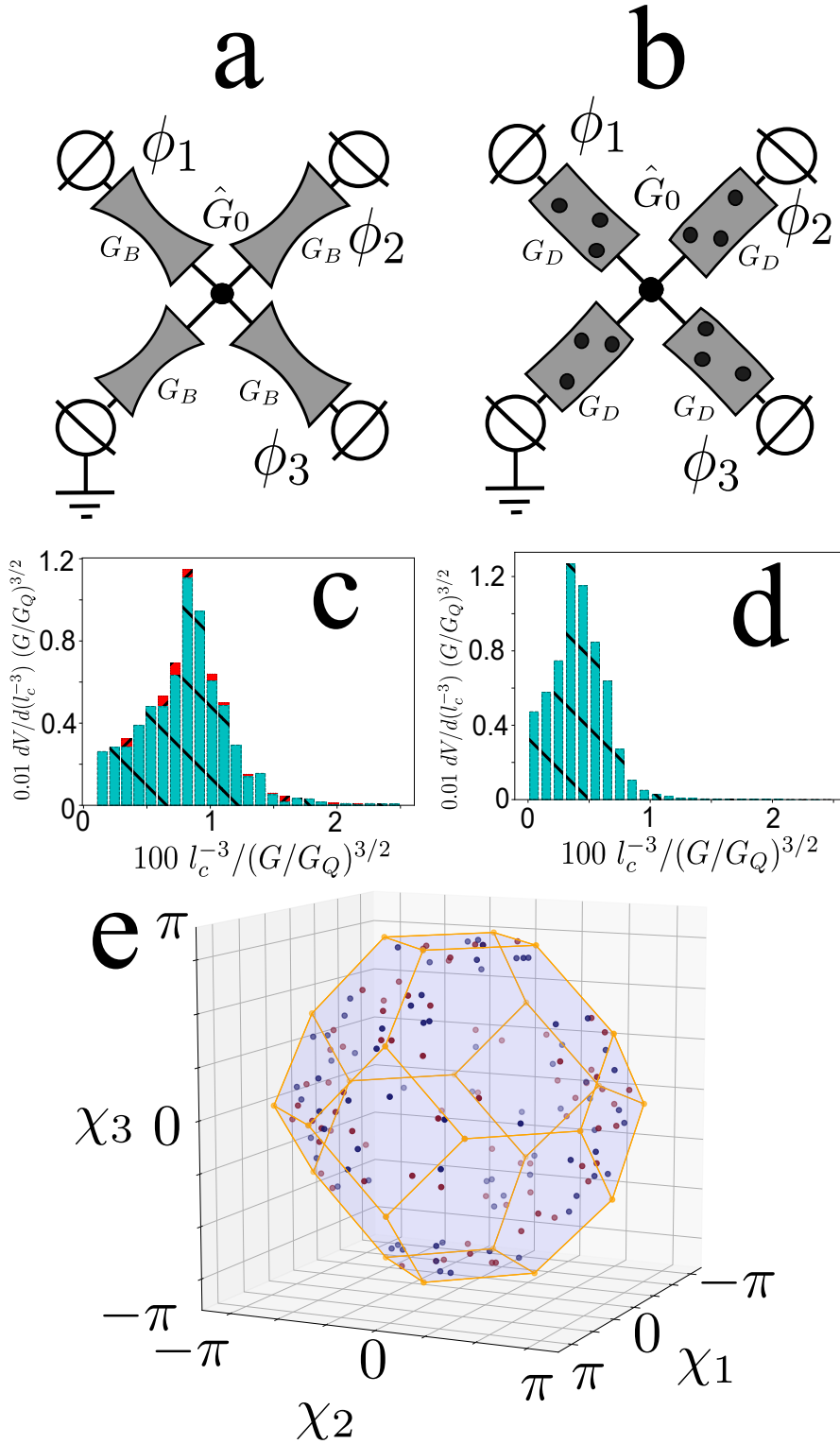


Figure 5.3: Weyl points in concrete nanostructures. Example circuits: ballistic (a) and diffusive (b) crosses of identical arm conductances G . The results for $dV/d(l_c^{-3})$ for the ballistic (c) and diffusive (d) cross. In (c), we compare estimations obtained from the analytical formula (green bars) and the actual positions of the WPs found (red bars) to demonstrate the correspondence within the statistical error. An example of WP positions found (e), $G/G_Q = 50$.

where 'prime' excludes the zero eigenvalues of \check{M} from the determinant.

We implement this general technique to compute I_c^{-3} for concrete superconducting nanostructures. It is known [6] that the energies of Andreev bound states are expressed in terms of the effective scattering matrix SS^* , S being the electron scattering matrix in the space of all channels coming to the nanostructure, S^* being the hole scattering matrix, the superconducting phases included. The circuit-theory action at the imaginary energy $\Delta \sin \theta$ (see e.g. [29]) before the averaging over the mesoscopic fluctuations can be expressed in terms of eigenvalues $SS^* \rightarrow -e^{i\lambda}$ of the effective scattering matrix, these eigenvalues coming in \pm pairs

$$\mathcal{S}(\theta, \phi) = -\sum_{\lambda} \ln(1 - \cos^2 \theta \cos^2(\lambda/2)) \quad (5.8)$$

$$\approx -\sum_{\lambda} \ln(\theta + i\lambda) \quad (5.9)$$

the last equality holding for close to zero energies/eigenvalues. The correlator of the velocities in this limit is related to the correlator of the action values,

$$\langle\langle \partial_{\alpha} \mathcal{S}(\theta) \partial_{\beta} \mathcal{S}(\theta') \rangle\rangle = \pi \frac{\langle\langle v_{\alpha} v_{\beta} \rangle\rangle \rho_{\lambda}}{|\theta| + |\theta'|}. \quad (5.10)$$

The action can be represented in a quantum circuit theory of 2×2 matrices, and the correlator is to be computed with the aid of Eq. 5.7. In Supplementary Material [1], we derive an explicit expression of I_c^{-3} for a single-node structure.

We concentrate on two simplest example MTSN (Fig. 5.3 a,b): a chaotic cavity connected to four leads by ballistic conductors of the same conductance G , ballistic cross, and the corresponding diffusive structure, diffusive cross. With the expressions obtained, we compute the distribution of I_c^{-3} , and, consequently, the WP density, over the phase space, by evaluating I_c^{-3} in random points and collecting the data into histograms: this gives a fraction of the phase space volume $dV/d(I_c^{-3})$, at a given I_c^{-3} . The histograms for these two examples are qualitatively similar but distinct. Summing up the histograms and employing the result (5.1) gives the already mentioned estimations of the number of WP's, Eq. 5.3.

Activity C. We explicitly compute the WP positions for random chaotic cavities. For this, we pick up the electron scattering matrix S from the circular orthogonal ensemble, and find all phase settings at which SS^* has an eigenvalue -1 [6]. We find 75-95 WPs for $N = G/G_Q = 50$ conform to the results of the activities A,B and verify the scaling of the number of points with N . We also perform a more thorough check evaluating I_c^{-3} in the random positions found and collecting the data to the histogram. The resulting estimation of $dV/d(I_c^{-3})$ that involves 2686 WP's coincides with the results of activity B within the statistical error (Fig. 5.3 c). In Fig. 5.3 e, we plot the positions of WP's found for a realization of S at $G/G_Q = 50$. We choose the coordinate system in the space of phases to be consistent with the symmetry of the structure,

$$\chi_1 = \frac{1}{2}(\phi_1 - \phi_2 - \phi_3), \quad (5.11)$$

$\chi_{2,3}$ are defined by the above relation with cyclically permuted indexes. In these coordinates, the BZ is the truncated octahedron, as for a fcc lattice. The gapped region is in the centre

of the BZ, the gapless region encloses its boundary [19]. The special points where the gapless region becomes infinitesimally thin [21] are located in the centres of the squares and hexagons, and, as seen in the Figure, the WPs are mostly concentrated in the corners of the BZ.

Let us shortly discuss the methods of experimental detection of WPs in MTSN. For sufficiently large level splitting $G \simeq G_Q$, the WPs can be found spectroscopically as the zeros of the lowest Andreev state. For $G \simeq G_Q$ where the level splitting is small not exceeding $k_B T$, the detection is more challenging. For this case, we envisage the following detection methods: i. (Telegraph) noise measurements of the inductive or Berry curvature response of the MTSN. These responses diverge for a single discrete state at WP position. While the averaging over the states with thermal Boltzmann weights cancels the divergence, it is manifested in the noise at the time scale of the order of the time of switching between the states. ii. Transconductance (noise) measurements. We predict a transconductance $\simeq \sqrt{GG_Q}$. While in the presence of thermal averaging this transconductance is not quantized, its value will exhibit fluctuations as a function of the control phase [30] that can be used for scanning the WP positions. iii. Transport spectroscopy. If the MTSN is in a weak tunnel contact with a normal lead, the differential conductance of this tunnel junction exhibits low-voltage anomalies at the WP positions [10]. There is also a WP signature persisting at high voltage bias [10].

5.1. SUPPLEMENTAL MATERIAL

In this Supplemental Material, we present additional details about the activities A, B, and C.

5.2. ACTIVITY A: DENSITY AND CHARGE CORRELATIONS OF WP IN A UNIFORM PARAMETER SPACE

The goal of this activity is to relate the actual density of WP's with the universal correlation parameter l_c . We implement a variation of Wilkinson model with random class C $2N \times 2N$ matrices (Eq. 1 of the main text) where $l_c \equiv \pi\sqrt{3/2N}$ does not depend on the position in the 3d space of the phases. $N=60$ $l_c = 0.496$ $N=80$ $l_c = 0.430$

To find the WP's, we implement an iterative optimization procedure in the 3D parameter space. The optimization function is the smallest in modulus eigenvalue of the matrix. Since it involves the matrix diagonalization, the computation time scales as N^3 . The initial position is chosen randomly. The coordinates of a WP are found after several tens of iterations. To find *all* WP's, we repeat the procedure again and again, keeping the list of WP's found to exclude the duplicates. We learned from the experience that the procedure has to be repeated five times the expected number of WP's: further runs do not deliver new points. Since the expected number of points scales as $N^{3/2}$, the total computation time scales as $N^{9/2}$ and really big N are not accessible for practical calculations. The following table summarizes our concrete results for the number of WP averaged for a number of runs :

N	40	60	80
# runs	34	5	2
$\langle N_W \rangle$	930.5 ± 60.5	1692.0 ± 49.9	2571.5 ± 24.5
c_W	0.844 ± 0.054	0.836 ± 0.024	0.825 ± 0.007

This brought us to the value $c_W = 0.83 \pm 0.05$ (Eq. 2 of the main text).

As an extra check of the method in use, we compute the concentration of the level crossings far from zero energy, namely between the 10th and 11th level. We expect this to be close to the concentration of WP's in the GUE ensemble. Wilkinson et al. have computed this concentration to be $(2/3)\sqrt{\pi} \approx 1.18$ in units of l_c^{-3} . Our calculation for $N = 40$ averaged over 6 runs gives a consistent value 1.146 ± 0.065 .

In the course of calculations, we have accumulated significant statistics of WP coordinates and their charges. We hoped that these statistics suffices to compute the charge-charge correlations of WP distribution. However, this did not work. The histograms approximating the charge density at a given distance from a WP exhibited significant fluctuations at relatively large distances. Our attempts to smooth these fluctuations considering the Laplace transform of the charge-charge correlator initially led us to an erroneous conclusion of a power-like tail in this correlator.

Fortunately, we checked these conclusions with an alternative method. We have computed the correlator of Berry curvatures at given distances. The most general form of the correlator of two vector quantities B^α in the dimensionless coordinates \mathbf{r} reads

$$\langle \langle B^\alpha(\mathbf{R}) B^\beta(\mathbf{R} + \mathbf{r}) \rangle \rangle = \delta_{\alpha\beta} B(r) + \frac{r^\alpha r^\beta}{r^2} B_1(r) \quad (5.12)$$

Since $Q(\mathbf{r}) = (4\pi)^{-1} \partial_\alpha B^\alpha(\mathbf{r})$, the charge-charge correlator is then expressed as

$$(4\pi)^2 \langle \langle Q(\mathbf{R}) Q(\mathbf{R} + \mathbf{r}) \rangle \rangle = \frac{3}{r^2} \frac{\partial}{\partial r} (r B_1(r)) - \frac{1}{r^2} \frac{\partial}{\partial r} \left(r^2 \frac{\partial}{\partial r} B(r) \right) \quad (5.13)$$

We compute the correlator at each r separately accumulating the statistics of Berry curvatures $B_{1,2}^\alpha$ in two random points 1,2 separated by the distance r . The computation is relatively fast so for each point we can accumulate 10^4 samples for $N = 40$ and 10^5 samples for $N = 20$. It may seem that the two independent functions in the correlator are just given by the average products

$$B(r) = \frac{1}{4} \left(\langle B_1^\alpha B_2^\alpha \rangle - \langle B_1^\alpha n^\alpha B_2^\beta n^\beta \rangle \right); \quad (5.14)$$

$$B_1(r) = -\frac{1}{2} \langle B_1^\alpha B_2^\alpha \rangle + \frac{3}{2} \langle B_1^\alpha n^\alpha B_2^\beta n^\beta \rangle. \quad (5.15)$$

However, the evaluation is not so simple. As has been mentioned in [8], the distribution of B^α has long power-law tails resulting in an infinite variance. Owing to this, the accuracy of computed averages does not increase with the number of samples in the statistics.

The universal prescription to evaluate the averages in this situation is to disregard the large values. We implement it in the following fashion: we rescale the accumulated values of B^α to decrease it if large,

$$\tilde{B}^\alpha = \frac{B^\alpha}{\sqrt{1 + B^\beta B^\beta / B_0^2}}. \quad (5.16)$$

Here, B_0 is a parameter and the modulus of the rescaled \bar{B}^α never exceeds B_0 . The variance of \bar{B}^α is thus finite, and usual statistical considerations do apply. The value of B_0 should not be taken too small since the averages would not approximate the correlator, nor too large since the large values of B^α would not be suppressed. In practice, we plot the averages versus B_0 and pick up the value of the average that persist in a large interval of B_0 .

Within statistical error, $B_1(r) = 0$ for all r . We can prove this analytically for $r \ll 1$. With this,

$$\langle\langle Q(0)Q(r) \rangle\rangle = (4\pi)^{-2} \nabla^2 B(r). \quad (5.17)$$

As stated in the main text, the correlator of Berry curvatures can be approximated with

$$B(r) \approx 10.4e^{-2.8r-3.3r^2} \quad (5.18)$$

This has no trace of long-distance power-law correlations.

This expression also proves the electro-neutrality of the WP distribution,

$$\int d\mathbf{r} \langle\langle Q(0)Q(\mathbf{r}) \rangle\rangle = -N_w/V \quad (5.19)$$

that is, the presence of a WP with the charge +1 at a point results in a depletion of average charge density around the point, the charge depleted being -1.

After completion of these calculation, we became aware of a similar calculation of the Berry curvature correlations. [16]. The authors address the correlator in a general GUE ensemble that is similar but distinct from near-zero energy correlator of interest. However, they use the same fitting function and end up with similar coefficients. In our notations, they give

$$rB(r) \approx 7.42e^{-3.56x-2.03x^2}. \quad (5.20)$$

5.3. ACTIVITY B: FINDING l_c IN QUANTUM CIRCUIT THEORY

The goal of this activity is to find the scale governing universal parametric correlations for concrete nanostructures that can modelled with quantum circuit theory [24]. For a 3D parameter space, this scale is defined as

$$l_c^{-3} = \sqrt{\det\langle\langle v_i v_j \rangle\rangle} / \delta_S^3 \quad (5.21)$$

where $v_i \equiv \partial E / \partial \phi_i$ is the "velocity" of an energy level in the spectrum and δ_S is the mean level spacing. The parameter l_c^{-3} depends on energy as well as on a point in the parameter space.

5.3.1. THE ACTION, MEAN LEVEL SPACING, AND THE VELOCITY CORRELATOR

At quantum level, the nanostructure is characterized by an electron scattering matrix S in the space of the quantum channels incoming from the leads where the superconducting phase is incorporated with a factor $e^{i\phi_i}$ ascribed to a channel coming from the lead i . One can derive (see e.g. [29]) an action for imaginary-time Green functions characterizing the nanostructure,

$$\mathcal{S}(\epsilon) = -\frac{1}{2} \text{Tr} \ln \left(\frac{E + \epsilon}{2E} + \frac{E - \epsilon}{2E} S S^* \right) \quad (5.22)$$

ϵ being the imaginary energy, $E \equiv \sqrt{\epsilon^2 + \Delta^2}$. It is known [6] that the Andreev bound states are related to the eigenvalues of SS^* . For these eigenvalues, we will use

$$SS^* \rightarrow -e^{i\lambda}. \quad (5.23)$$

The eigenvalues λ come in \pm pairs. The energies of the bound states correspond to zeros of the expression under the log. We introduce the notation $\epsilon/E = \sin\theta$, $-\pi/2 < \theta < \pi/2$, and rewrite the action as

$$\mathcal{S}(\theta) = -\sum_{\lambda} \ln(1 - \cos^2\theta \cos^2(\lambda/2)) \quad (5.24)$$

Since we are interested in characteristics of the spectrum near zero energy, we can expand in small θ, λ so the action becomes:

$$\mathcal{S} = -\sum_{\lambda} \ln(\theta - i\lambda/2) = -\sum_{\lambda>0} \ln(\theta^2 + \lambda^2/4) \quad (5.25)$$

In this limit, each λ gives a bound state at energy $\Delta\lambda$. Let us compute the derivative of the action with respect to θ :

$$\frac{\partial \mathcal{S}}{\partial \theta} = -\sum_{\lambda>0} \frac{2\theta}{\theta^2 + \lambda^2/4} = -\rho_{\lambda} \int_0^{\infty} d\lambda \frac{2\theta}{\theta^2 + \lambda^2/4} = -2\pi \text{sgn}(\theta) \rho_{\lambda} \quad (5.26)$$

where we made a semiclassical approximation replacing the summation over the discrete λ with integration over their continuous density ρ_{λ} . The semiclassical action has therefore a cusp at $\theta = 0$, the value of the cusp determines the density of the eigenvalues, that is directly related to the mean level spacing.

Let us look at the random velocities of the levels, the velocity with respect to a parameter α being $v_{\alpha} \equiv \partial_{\alpha} \lambda$. The derivative of the action then reads

$$\partial_{\alpha} \mathcal{S} = -\sum_{\lambda>0} \frac{\lambda v_{\alpha}}{2(\theta^2 + \lambda^2/4)} \quad (5.27)$$

The velocities correlate at the same level only. For the correlator of the derivatives, this gives

$$\langle\langle \partial_{\alpha} \mathcal{S}(\theta) \partial_{\beta} \mathcal{S}(\theta') \rangle\rangle = \langle\langle v_{\alpha} v_{\beta} \rangle\rangle \frac{\rho_{\lambda}}{4} \int_0^{\infty} \frac{d\lambda \lambda^2}{(\theta^2 + \lambda^2/4)(\theta'^2 + \lambda^2/4)} = \pi \frac{\langle\langle v_{\alpha} v_{\beta} \rangle\rangle \rho_{\lambda}}{|\theta| + |\theta'|} \quad (5.28)$$

This implies that if we know $\langle\langle \mathcal{S}(\theta, \phi) \mathcal{S}(\theta', \phi) \rangle\rangle$, we can evaluate the velocity correlators and L_c^{-3}

5.3.2. SEMICLASSICS: SADDLE POINT

In quantum circuit theory approach, the same action is expressed as a functional of the matrices \check{G} , $\check{G}^2 = 1$, $\text{Tr} \check{G} = 0$ that is defined in the nodes and reservoirs of the nanostructure. The situation in hand we can describe with 2×2 matrices. These matrices are fixed in the leads

$$\check{G}_i = \begin{bmatrix} \sin\theta & \cos\theta e^{-i\phi_i} \\ \cos\theta e^{i\phi_i} & -\sin\theta \end{bmatrix}. \quad (5.29)$$

The matrices in the nodes are obtained by minimization of the action. In case of a short nanosctructure, the action is a sum of contributions of each connector,

$$\mathcal{S} = \sum_c \mathcal{S}_c; \quad \mathcal{S}_c = \frac{1}{2} \text{Tr} \mathcal{F}_c \left(\frac{1}{2} (\check{G}_a \check{G}_b + \check{G}_b \check{G}_a) \right). \quad (5.30)$$

The function \mathcal{F}_c is proportional to the conductance of the connector and depends on the type of the connector. For instance, for a quantum point contact of conductance G $\mathcal{F}(x) = -(G/G_Q) \ln((x+1)/2)$. Generally, a connector is characterized by a set of transmission coefficients T_p , and

$$\mathcal{F}(x) = - \sum_p \ln \left(1 + \frac{T_p}{2} (x-1) \right). \quad (5.31)$$

Long nanostructures can be described with addition of "leakage" connectors [24], yet we do not need this extension since the density of Weyl points is determined by the spectrum properties at zero energy that do not depend on the size of the nanostructure.

We will restrict ourselves to the simplest situation with a single node in the nanostructure and any number of the reservoirs. The connectors can be labelled with the lead index i , and

$$\mathcal{S} = \frac{1}{2} \sum_i \text{Tr} \mathcal{F}_i \left(\frac{1}{2} (\check{G}_i \check{G} + \check{G} \check{G}_i) \right) \quad (5.32)$$

where \check{G} is the matrix in the node. We will make use of the fact that $\check{G}_i \check{G} + \check{G} \check{G}_i$ is a number rather than a matrix for any 2×2 matrices.

It is constructive to map the 2×2 matrices on the corresponding 3D vectors,

$$\check{G}_i \rightarrow (\cos \theta \cos \phi_i, \cos \theta \sin \phi_i, \sin \theta) \quad (5.33)$$

while the node matrix

$$\check{G} \rightarrow (\cos \Theta \cos \Phi, \cos \Theta \sin \Phi, \sin \Theta) \quad (5.34)$$

This gives the following inner products for each connector,

$$s_i = \sin \theta \sin \Theta + \cos \Theta \cos \theta \cos(\phi_i - \Phi), \quad (5.35)$$

so the action reads

$$\mathcal{S} = \sum_i \mathcal{F}_i(s_i) \quad (5.36)$$

To find \check{G} , we minimize with respect to Θ, ϕ . This gives two conditions:

$$0 = \sum_i \mathcal{F}'_i(s_i) \partial_\Theta s_i = \sum_i \mathcal{F}'_i(s_i) (\sin \theta \cos \Theta - \sin \Theta \cos(\phi_i - \Phi)) \quad (5.37)$$

$$0 = \sum_i \mathcal{F}'_i(s_i) \partial_\Phi s_i = \sum_i \mathcal{F}'_i(s_i) \sin(\phi_i - \Phi) \quad (5.38)$$

In the limit of $\theta \rightarrow 0$, this becomes

$$0 = \sum_i \mathcal{F}'_i(s_i) \cos(\phi_i - \Phi) = \sum_i \mathcal{F}'_i(s_i) s_i \quad (5.39)$$

$$0 = \sum_i \mathcal{F}'_i(s_i) \sin(\phi_i - \Phi) \quad (5.40)$$

We can extract level spacing from the cusp of the action at small θ . By virtue of optimization, $\text{sgn}\Theta = \text{sgn}\theta$. Therefore, at small values of θ $s_i \rightarrow s_i + |\theta||\sin\Theta|$, and the cusp part of the action reads

$$\mathcal{S} = |\theta||\sin\Theta| \sum_i \mathcal{F}'_i(s_i) \quad (5.41)$$

The density of the eigenvalues is then extracted with the aid of Eq. 5.26.

5.3.3. SEMICLASSICS: CORRELATIONS

To compute the correlations of the action at two different parameter settings, (θ, ϕ_i) , and (θ', ϕ'_i) , we have to double the dimension of the matrices. So we consider 4×4 matrices. We need to do this separately for diffusion and Cooperon channels [9]. For the reservoirs, these matrices are made from two diagonal blocks, each corresponding to a setting of the corresponding reservoir. We will distinguish the settings marking or not marking then with a prime,

$$\check{G}_i \rightarrow \begin{bmatrix} G_i & 0 \\ 0 & G'_i \end{bmatrix} \quad (5.42)$$

For the diffusion channel, G'_i is just given by Eq. 5.29. For the Cooperon channel, G'_i is *transposed*.

The optimization of the action results in the block-diagonal matrix in the node

$$\hat{G}_0 \rightarrow \begin{bmatrix} G_0 & 0 \\ 0 & G'_0 \end{bmatrix} \quad (5.43)$$

To compute the correlations, we have to derive the quadratic expansion of the action near this optimum. With the quadratic accuracy, \hat{G} is given by

$$\check{G} = \check{G}_0 + \check{g} - \frac{1}{2} \check{G}_0 \check{g}^2; \quad \check{g} \check{G} + \check{G} \check{g} = 0 \quad (5.44)$$

We need to substitute this to the action and expand it to the terms quadratic in \check{g} . The first-order terms cancel since \check{G}_0 corresponds to the minimum of the action.

This calculation is made most efficiently in the basis where G_0 is a diagonal matrix,

$$\hat{G}_0 = \begin{bmatrix} 1 & 0 & 0 & 0 \\ 0 & -1 & 0 & 0 \\ 0 & 0 & 1 & 0 \\ 0 & 0 & 0 & -1 \end{bmatrix} \quad (5.45)$$

In this basis, a matrix of a reservoir read

$$\hat{G}_i = \begin{bmatrix} s & u & 0 & 0 \\ u^* & -s & 0 & 0 \\ 0 & 0 & s' & u' \\ 0 & 0 & u'^* & -s' \end{bmatrix} \quad (5.46)$$

where s, u possess the index i , $s^2 + |u|^2 = 1$, s being inner product introduced earlier. The minimization equation in these basis reads:

$$0 = \sum_i \mathcal{F}'(s_i) u_i. \quad (5.47)$$

Let us specify those more explicitly. We choose a basis in the space of 3d vectors with the z-axis in the direction of G_0 , the angle ϕ is counted from Φ ,

$$\mathbf{x} = (-\sin\Theta, 0, \cos\Theta) \quad (5.48)$$

$$\mathbf{y} = (0, 1, 0) \quad (5.49)$$

$$\mathbf{z} = (\cos\Theta, 0, \sin(\Theta)) \quad (5.50)$$

From this,

$$u = -\sin\Theta \cos\theta \cos(\phi_i - \Phi) + \cos\Theta \sin\theta + i \cos(\theta) \sin(\phi_i - \Phi). \quad (5.51)$$

At $\theta \rightarrow 0$,

$$u = -\sin\Theta \cos(\phi_i - \Phi) + i \sin(\phi_i - \Phi). \quad (5.52)$$

Let us proceed with the expansion. We need to choose the \check{g} in the non-diagonal blocks and guarantee that it anti-commutes with \check{G} - otherwise, it will not modify \check{G} and the value of the action will not change. The most general matrix of this kind can be parametrized as

$$\begin{bmatrix} 0 & 0 & 0 & w_2 \\ 0 & 0 & w_1 & 0 \\ 0 & v_1 & 0 & 0 \\ v_2 & 0 & 0 & 0 \end{bmatrix} \quad (5.53)$$

A straightforward but lengthy calculation results in the following form:

$$\delta\mathcal{S} = \frac{1}{2} \sum_i \begin{bmatrix} v_1 \\ v_2 \end{bmatrix} \begin{bmatrix} A_i & B_i^* \\ B_i & A_i \end{bmatrix} \begin{bmatrix} w_1 \\ w_2 \end{bmatrix} \quad (5.54)$$

with

$$A_i = \frac{\mathcal{F}'_i(s_i)(1 - s_i^2) - \mathcal{F}'_i(s'_i)(1 - s_i'^2)}{s_i - s'_i}; \quad B_i = u_i u'_i \frac{\mathcal{F}'(s_i) - \mathcal{F}'(s'_i)}{s_i - s'_i} \quad (5.55)$$

This expression is for the diffusion channel, for the Cooperon channel we need to replace $u' \rightarrow u'^*$.

5.3.4. CLOSE POINTS

For our task, we need to analyse the quadratic form in close points, $\phi_i \rightarrow \phi'_i$. The form of the correlator given by Eq. 5.28 suggests that there is an eigenvalue of this matrix that goes to 0 at $\phi_i \rightarrow \phi'_i$ and $\theta \rightarrow 0$, and the parametric dependence of this eigenvalue defines the correlations. The calculation shows no such eigenvalue in the diffusion channel, so from now on we concentrate on the Cooperon one. In this case,

$$A = \sum_i (\mathcal{F}'(s_i)(1 - s_i^2))' = \sum_i \mathcal{F}''(s_i)(1 - s_i^2) - 2 \sum_i \mathcal{F}'(s_i) s_i; \quad B = \sum_i \mathcal{F}''(s_i)(1 - s_i^2) \quad (5.56)$$

At $\theta \rightarrow 0$, $\sum_i \mathcal{F}'(s_i) s_i \rightarrow 0$ and the determinant $A^2 - |B|^2$ vanishes indicating the small eigenvalue expected. The determinant can be presented as

$$(A - \text{Re}B)(A + \text{Re}B) - (\text{Im}B)^2 \quad (5.57)$$

where $A - \text{Re}B$ goes to zero in close points at $\theta \rightarrow 0$, $A + \text{Re}B$ does not, and $\text{Im}B$ goes to zero in close points irrespective of θ .

Let us compute $A - B$ in coinciding points.

$$A = (\mathcal{F}'(s)(1 - s^2))'; B = (1 - s^2)\mathcal{F}''(s) \rightarrow A - B = -2s\mathcal{F}'(s) \quad (5.58)$$

Here, the summation over i is implied. We know that $\sum_i \mathcal{F}'(s_i)u_i = 0$ at any θ . We note that

$$s_i = \sin\theta \sin\Theta + \cos\theta \cos\Theta \cos(\phi_i - \Phi) \quad (5.59)$$

$$\text{Re}(u_i) = -\sin\Theta \cos\theta \cos(\phi_i - \Phi) + \sin\theta \cos\Theta \quad (5.60)$$

To this end, we evaluate

$$\sum_i \mathcal{F}'(s_i)s_i = \sum_i \mathcal{F}'(s_i)(s_i + \cotan\Theta \text{Re}u_i) = \frac{\sin\theta}{\sin\Theta} \sum_i \mathcal{F}'(s_i) \quad (5.61)$$

Generalizing to small θ and the same points in the phase space, we obtain

$$A - B = -\frac{|\theta| + |\theta'|}{\sin\Theta} \sum_i \mathcal{F}'(s_i) \quad (5.62)$$

Let us compute $A + B$. We can neglect θ and the difference between the points to obtain

$$A + B = 2 \sum_i \mathcal{F}''(s_i)(1 - s_i^2) \quad (5.63)$$

Let us compute the terms in $A - \text{Re}B$ that are proportional to the squares of the differences between the points. We start with

$$A - \text{Re}B = \frac{\mathcal{F}'(s)(1 - s^2) - \mathcal{F}'(s')(1 - s'^2)}{s - s'} - \frac{uu'^* + u'u^*}{2} \frac{\mathcal{F}'(s) - \mathcal{F}'(s')}{s - s'} \quad (5.64)$$

Let us represent

$$u = \sqrt{1 - s^2}e^{i\mu}; u' = \sqrt{1 - s'^2}e^{i\mu'} \quad (5.65)$$

With this, the difference becomes

$$A - \text{Re}B = \frac{\mathcal{F}'(s)(1 - s^2) - \mathcal{F}'(s')(1 - s'^2)}{s - s'} - \sqrt{1 - s^2}\sqrt{1 - s'^2} \cos(\mu - \mu') \frac{\mathcal{F}'(s) - \mathcal{F}'(s')}{s - s'} \quad (5.66)$$

There are two contributions to the difference. One comes from $\delta\mu_i$ and reads

$$A - \text{Re}B = \frac{1}{2} \sum_i (\delta\mu)_i^2 (1 - s_i^2) \mathcal{F}''(s_i) \quad (5.67)$$

For another one, one can set $\delta\mu = 0$.

$$A - \text{Re}B = \quad (5.68)$$

$$\frac{\mathcal{F}'(1 - s^2) - \mathcal{F}'(s')(1 - s'^2) + \sqrt{(1 - s^2)(1 - s'^2)}(\mathcal{F}'(s') - \mathcal{F}'(s))}{s - s'} = \quad (5.69)$$

$$- \frac{s + s'}{\sqrt{1 - s^2} + \sqrt{1 - s'^2}} \left(\mathcal{F}'(s)\sqrt{1 - s^2} + \mathcal{F}'(s')\sqrt{1 - s'^2} \right) \quad (5.70)$$

To simplify, we may add $\mathcal{F}'(s)s + \mathcal{F}'(s')s'$ that is zero under sum provided $\theta = 0$. This gives

$$A - \text{Re}B = \frac{\sqrt{(1-s^2)(1-s'^2)}}{\sqrt{1-s^2} + \sqrt{1-s'^2}} (\mathcal{F}'(s) - \mathcal{F}'(s')) \left(\frac{s}{\sqrt{1-s^2}} - \frac{s'}{\sqrt{1-s'^2}} \right) \quad (5.71)$$

With this, we get for the difference

$$A - \text{Re}B = \frac{1}{2} \sum_i (\delta s)_i \frac{\mathcal{F}''(s_i)}{1-s_i^2} + \frac{1}{2} \sum_i (\delta \mu)_i^2 (1-s_i^2) \mathcal{F}''(s_i) \quad (5.72)$$

We also have to inspect $\text{Im}B$.

$$\text{Im}B = i \frac{uu'^* - u^*u}{2} \frac{\mathcal{F}'(s) - \mathcal{F}'(s')}{s-s'} \approx \delta \mu (1-s^2) \mathcal{F}''(s) \quad (5.73)$$

With all this,

$$\ln \det = \ln(C + D) \quad (5.74)$$

$$C = -\frac{|\theta| + |\theta'|}{\sin \Theta} \sum_i \mathcal{F}'(s_i) \quad (5.75)$$

$$D = \frac{1}{2} \sum_i (\delta s)_i \frac{\mathcal{F}''(s_i)}{1-s_i^2} + \frac{1}{2} \sum_i (\delta \mu)_i^2 (1-s_i^2) \mathcal{F}''(s_i) \quad (5.76)$$

$$- \frac{(\sum_i \delta \mu_i (1-s_i^2) \mathcal{F}''(s_i))^2}{2 \sum_i \mathcal{F}''(s_i) (1-s_i^2)} \quad (5.77)$$

The latter part can be presented as

$$D = \frac{1}{2} D_{\alpha\beta} \delta \phi_\alpha \delta \phi_\beta \quad (5.78)$$

α, β labelling the independent phases. For this, we need to express $\delta s_i, \delta \mu_i$ in terms of $\delta \phi_i$. The corresponding formulas are straightforward but rather cumbersome. In fact, we do not use those in numerical calculations, but rather compute $\delta s_i, \delta \mu_i$ in terms of $\delta \phi_i$ to evaluate the quadratic form $D_{\alpha\beta}$. So we do not give these formulas here.

5.3.5. RESULTING RELATION

We recall that the density in the phase space can be expressed as

$$l_c^{-3} = \sqrt{\det < v_\alpha v_\beta > \rho_\lambda^3} \quad (5.79)$$

We have derived that

$$\rho_\lambda = \frac{|\sin \Theta|}{2\pi} \left| \sum_i \mathcal{F}'(s_i) \right| \quad (5.80)$$

$$\mathcal{S}_{\alpha\beta} = \pi \frac{\langle \langle v_\alpha v_\beta \rangle \rangle \rho_\lambda}{|\theta| + |\theta'|} \quad (5.81)$$

$$\mathcal{S}_{\alpha\beta} = \frac{D^{\alpha\beta}}{C} \quad (5.82)$$

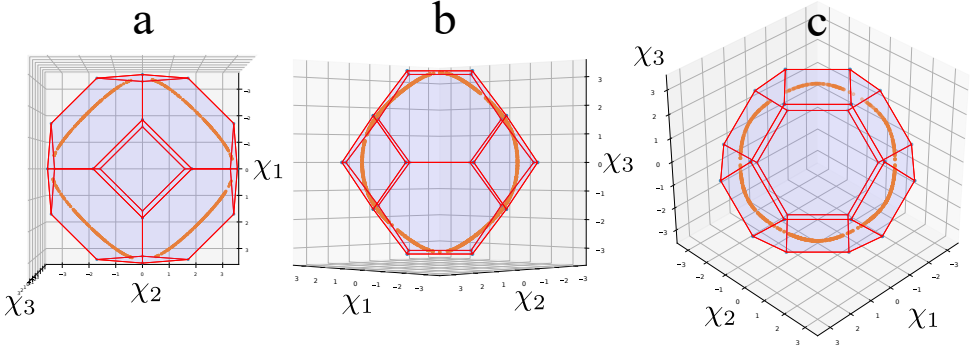


Figure 5.4: The boundary of the gapless region (orange points) for several cross-sections plotted in a 3D along with the edges of the Brillouin zone. The view axis is perpendicular to the cross-section plane. a: cross-section plane $\chi_3 = 0$, b: cross-section plane $\chi_1 = \chi_2$, c: cross-section plane $\chi_1 + \chi_2 + \chi_3 = 0$.

So we get

$$\pi^2 < v_\alpha v_\beta > \rho_\lambda^2 = D_{\alpha\beta} \frac{\sin^2 \Theta}{2} \quad (5.83)$$

Finally, collecting all terms, we obtain:

$$l_c^{-3} = \sqrt{\det D_{\alpha\beta}} \frac{\sin^3 \Theta}{2\sqrt{2}\pi^3}. \quad (5.84)$$

We will use this formula for numerical evaluations. We stress this requires minimization for each set of ϕ_i to compute Θ, Φ and minimization around this point to evaluate $D_{\alpha\beta}$.

5.4. ACTIVITY C: WP POSITIONS FOR BALLISTIC CROSS

Within the activity, we find the coordinates of the WP's in a ballistic cavity model connected to four superconducting leads. We take a random realization of the $4N \times 4N$ electron scattering matrix, augment it with the phases of the superconducting reservoirs and find the points where SS^* has an eigenvalue -1 with the optimization procedure similar to that described in Section 5.3. Our results for the total number of points are summarized in the following table

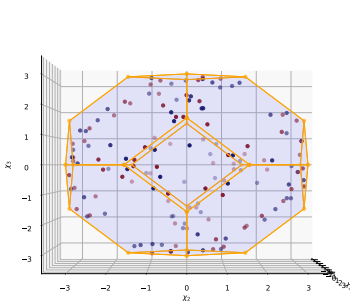
N	50	35	20
# runs	15	8	10
$< N_W >$	153.5 ± 13.8	93.0 ± 11.8	46.4 ± 6.7

From this, we inherit $N_w = 0.40G/G_Q$ as cited in the main text.

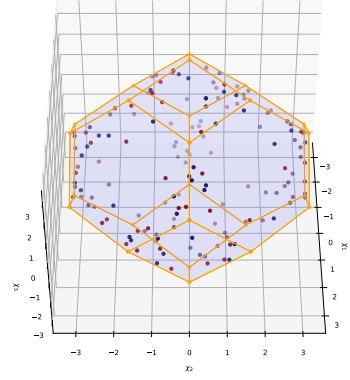
The points are found within the gapless region predicted by the semiclassical calculation. In Fig. 5.4 we present the boundaries of the gapless region for several cross-sections of the Brillouin zone in $\chi_{1,2,3}$ coordinates. We see that the boundary touches the centres of the squares and hexagons bounding the Brillouin zone.

To check the correspondence of the positions of the WP's found with the predictions of the semi-classical theory, we compute the semi-classical density l_c^{-3} in the positions found

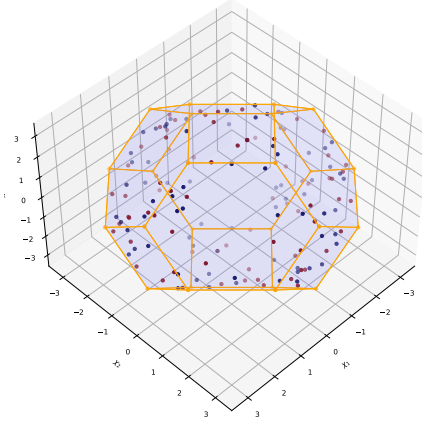
and accumulate the data to a histogram. The resulting distribution should differ by a factor of l_c^{-3} from the distribution of l_c^{-3} itself. Indeed, when we plot together the distribution of l_c^{-3} and the distribution corrected by the factor, we observe a satisfactory correspondence (Fig. 3c of the main text). In conclusion, we present several 3D views of a realization of WP for $N = 50$. (Fig. 5.5)



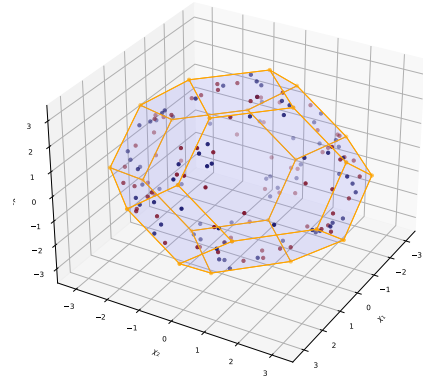
(a) View angles 0,0



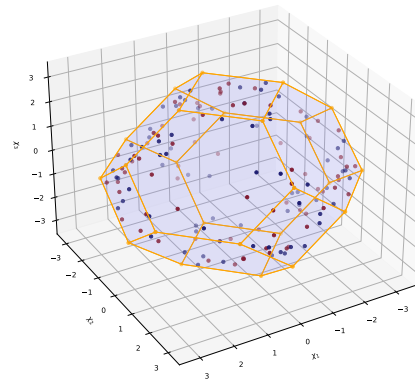
(b) View angles 45,0



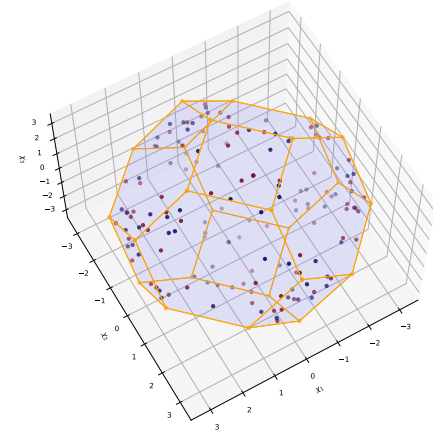
(c) View angles 45,45



(d) View angles 30,30



(e) View angles 30,60



(f) View angles 60,60

Figure 5.5: Positions of Weyl points for a given realization of S at $N = 50$ at various view angles.

BIBLIOGRAPHY

- [1] See Supplemental Material at [URL will be inserted by publisher] for a detailed explanation of all activities of this project.
- [2] Alexander Altland and Martin R. Zirnbauer. “Nonstandard symmetry classes in mesoscopic normal-superconducting hybrid structures”. In: *Phys. Rev. B* 55 (2 Jan. 1997), pp. 1142–1161. DOI: [10.1103/PhysRevB.55.1142](https://doi.org/10.1103/PhysRevB.55.1142). URL: <https://link.aps.org/doi/10.1103/PhysRevB.55.1142>.
- [3] N. P. Armitage, E. J. Mele, and Ashvin Vishwanath. “Weyl and Dirac semimetals in three-dimensional solids”. In: *Rev. Mod. Phys.* 90 (1 Jan. 2018), p. 015001. DOI: [10.1103/RevModPhys.90.015001](https://doi.org/10.1103/RevModPhys.90.015001). URL: <https://link.aps.org/doi/10.1103/RevModPhys.90.015001>.
- [4] Hristo Barakov and Yuli V. Nazarov. “Abundance of Weyl points in semiclassical multi-terminal superconducting nanostructures”. In: *arXiv* (Dec. 2021). eprint: [2112.13928](https://arxiv.org/abs/2112.13928). URL: <https://arxiv.org/abs/2112.13928v1>.
- [5] C. W. J. Beenakker. “Brownian-motion model for parametric correlations in the spectra of disordered metals”. In: *Phys. Rev. Lett.* 70 (26 June 1993), pp. 4126–4129. DOI: [10.1103/PhysRevLett.70.4126](https://doi.org/10.1103/PhysRevLett.70.4126). URL: <https://link.aps.org/doi/10.1103/PhysRevLett.70.4126>.
- [6] C. W. J. Beenakker. “Random-matrix theory of quantum transport”. In: *Rev. Mod. Phys.* 69 (3 July 1997), pp. 731–808. DOI: [10.1103/RevModPhys.69.731](https://doi.org/10.1103/RevModPhys.69.731). URL: <https://link.aps.org/doi/10.1103/RevModPhys.69.731>.
- [7] B.A. Bernevig and T.L. Hughes. *Topological Insulators and Topological Superconductors*. Princeton University Press, 2013. ISBN: 9780691151755. URL: <https://books.google.nl/books?id=wOn7JHSSxrsC>.
- [8] M. V. Berry and Pragya Shukla. “Geometric Phase Curvature Statistics”. In: *Journal of Statistical Physics* 180.1 (Sept. 2020), pp. 297–303. ISSN: 1572-9613. DOI: [10.1007/s10955-019-02400-6](https://doi.org/10.1007/s10955-019-02400-6). URL: <https://doi.org/10.1007/s10955-019-02400-6>.
- [9] G. Campagnano and Yu. V. Nazarov. “ G_Q corrections in the circuit theory of quantum transport”. In: *Phys. Rev. B* 74 (12 Sept. 2006), p. 125307. DOI: [10.1103/PhysRevB.74.125307](https://doi.org/10.1103/PhysRevB.74.125307). URL: <https://link.aps.org/doi/10.1103/PhysRevB.74.125307>.
- [10] Y. Chen and Y. V. Nazarov. “Spintronics with a Weyl point in superconducting nanostructures”. In: *Phys. Rev. B* 103 (16 Apr. 2021), p. 165424. DOI: [10.1103/PhysRevB.103.165424](https://doi.org/10.1103/PhysRevB.103.165424). URL: <https://link.aps.org/doi/10.1103/PhysRevB.103.165424>.

- [11] Anne W. Draelos et al. “Supercurrent Flow in Multiterminal Graphene Josephson Junctions”. In: *Nano Lett.* 19.2 (FEB 2019), pp. 1039–1043. ISSN: 1530-6984. DOI: [10.1021/acs.nanolett.8b04330](https://doi.org/10.1021/acs.nanolett.8b04330).
- [12] Elham M. T. Fadaly et al. “Observation of Conductance Quantization in InSb Nanowire Networks”. In: *Nano Lett.* 17.11 (2017). PMID: 28665621, pp. 6511–6515. DOI: [10.1021/acs.nanolett.7b00797](https://doi.org/10.1021/acs.nanolett.7b00797). eprint: <https://doi.org/10.1021/acs.nanolett.7b00797>. URL: <https://doi.org/10.1021/acs.nanolett.7b00797>.
- [13] Valla Fatemi, Anton R. Akhmerov, and Landry Bretheau. “Weyl Josephson circuits”. In: *Phys. Rev. Research* 3 (1 Mar. 2021), p. 013288. DOI: [10.1103/PhysRevResearch.3.013288](https://doi.org/10.1103/PhysRevResearch.3.013288). URL: <https://link.aps.org/doi/10.1103/PhysRevResearch.3.013288>.
- [14] F. Faure and B. I. Zhilinskii. “Topological Chern indices in molecular spectra”. In: *Phys. Rev. Lett.* 85 (2000), p. 960.
- [15] Shechao Feng. “Chapter 4 - Conductance Fluctuations and 1/f Noise Magnitudes in Small Disordered Structures: Theory”. In: *Mesoscopic Phenomena in Solids*. Ed. by B.L. Altshuler, P.A. Lee, and R.A. Webb. Vol. 30. Modern Problems in Condensed Matter Sciences. Elsevier, 1991, pp. 107–129. DOI: <https://doi.org/10.1016/B978-0-444-88454-1.50010-3>. URL: <https://www.sciencedirect.com/science/article/pii/B9780444884541500103>.
- [16] Omri Gat and Michael Wilkinson. “Correlations of quantum curvature and variance of Chern numbers”. In: *SciPost Phys.* 10 (6 2021), p. 149. DOI: [10.21468/SciPostPhys.10.6.149](https://doi.org/10.21468/SciPostPhys.10.6.149). URL: <https://scipost.org/10.21468/SciPostPhys.10.6.149>.
- [17] Gino Graziano V et al. “Transport studies in a gate-tunable three-terminal Josephson junction”. In: *Phys. Rev. B* 101.5 (FEB 24 2020). ISSN: 2469-9950. DOI: [10.1103/PhysRevB.101.054510](https://doi.org/10.1103/PhysRevB.101.054510).
- [18] M. Z. Hasan and C. L. Kane. “Colloquium: Topological insulators”. In: *Rev. Mod. Phys.* 82 (4 Nov. 2010), pp. 3045–3067. DOI: [10.1103/RevModPhys.82.3045](https://doi.org/10.1103/RevModPhys.82.3045). URL: <https://link.aps.org/doi/10.1103/RevModPhys.82.3045>.
- [19] B. van Heck, S. Mi, and A. R. Akhmerov. “Single fermion manipulation via superconducting phase differences in multiterminal Josephson junctions”. In: *Phys. Rev. B* 90 (15 Oct. 2014), p. 155450. DOI: [10.1103/PhysRevB.90.155450](https://doi.org/10.1103/PhysRevB.90.155450). URL: <https://link.aps.org/doi/10.1103/PhysRevB.90.155450>.
- [20] Manuel Houzet and Julia S. Meyer. “Majorana-Weyl crossings in topological multiterminal junctions”. In: *Phys. Rev. B* 100.1 (JUL 29 2019). ISSN: 2469-9950. DOI: [10.1103/PhysRevB.100.014521](https://doi.org/10.1103/PhysRevB.100.014521).
- [21] Xiao-Li Huang and Yuli V. Nazarov. “Topology protection–unprotection transition: Example from multiterminal superconducting nanostructures”. In: *Phys. Rev. B* 100 (8 Aug. 2019), p. 085408. DOI: [10.1103/PhysRevB.100.085408](https://doi.org/10.1103/PhysRevB.100.085408). URL: <https://link.aps.org/doi/10.1103/PhysRevB.100.085408>.

- [22] R. L. Klees et al. “Microwave Spectroscopy Reveals the Quantum Geometric Tensor of Topological Josephson Matter”. In: *Phys. Rev. Lett.* 124.19 (MAY 13 2020). ISSN: 0031-9007. DOI: [10.1103/PhysRevLett.124.197002](https://doi.org/10.1103/PhysRevLett.124.197002).
- [23] R. Leone, L. P. Lévy, and P. Lafarge. “Cooper-pair pump as a quantized current source”. In: *Phys. Rev. Lett.* 100.11 (2008), p. 117001.
- [24] Y. V. Nazarov and Y. M. Blanter. *Quantum transport: Introduction to Nanoscience*. Cambridge: Cambridge University Press, 2009.
- [25] C. Padurariu et al. “Closing the proximity gap in a metallic Josephson junction between three superconductors”. In: *Phys. Rev. B* 92 (20 Nov. 2015), p. 205409. DOI: [10.1103/PhysRevB.92.205409](https://doi.org/10.1103/PhysRevB.92.205409). URL: <https://link.aps.org/doi/10.1103/PhysRevB.92.205409>.
- [26] Natalia Pankratova et al. “Multiterminal Josephson Effect”. In: *Phys. Rev. X* 10.3 (SEP 2 2020). ISSN: 2160-3308. DOI: [10.1103/PhysRevX.10.031051](https://doi.org/10.1103/PhysRevX.10.031051).
- [27] A. H. Pfeffer et al. “Subgap structure in the conductance of a three-terminal Josephson junction”. In: *Phys. Rev. B* 90 (7 Aug. 2014), p. 075401. DOI: [10.1103/PhysRevB.90.075401](https://doi.org/10.1103/PhysRevB.90.075401). URL: <https://link.aps.org/doi/10.1103/PhysRevB.90.075401>.
- [28] Xiao-Liang Qi and Shou-Cheng Zhang. “Topological insulators and superconductors”. In: *Rev. Mod. Phys.* 83 (4 Oct. 2011), pp. 1057–1110. DOI: [10.1103/RevModPhys.83.1057](https://doi.org/10.1103/RevModPhys.83.1057). URL: <https://link.aps.org/doi/10.1103/RevModPhys.83.1057>.
- [29] E. Repin V, Y. Chen, and Y. Nazarov V. “Topological properties of multiterminal superconducting nanostructures: Effect of a continuous spectrum”. In: *Phys. Rev. B* 99.16 (APR 10 2019). ISSN: 2469-9950. DOI: [10.1103/PhysRevB.99.165414](https://doi.org/10.1103/PhysRevB.99.165414).
- [30] R.-P Riwar et al. “Multi-terminal Josephson junctions as topological matter”. In: *Nat. Comm.* 7 (2016), p. 11167.
- [31] B. D. Simons and Boris L. Altshuler. “Universal velocity correlations in disordered and chaotic systems”. In: *Phys. Rev. Lett.* 70 (26 June 1993), pp. 4063–4066. DOI: [10.1103/PhysRevLett.70.4063](https://doi.org/10.1103/PhysRevLett.70.4063). URL: <https://link.aps.org/doi/10.1103/PhysRevLett.70.4063>.
- [32] B.Z. Spivak and A.Yu. Zyuzin. “Chapter 2 - Mesoscopic Fluctuations of Current Density in Disordered Conductors”. In: *Mesoscopic Phenomena in Solids*. Ed. by B.L. Altshuler, P.A. Lee, and R.A. Webb. Vol. 30. Modern Problems in Condensed Matter Sciences. Elsevier, 1991, pp. 37–80. DOI: <https://doi.org/10.1016/B978-0-444-88454-1.50008-5>. URL: <https://www.sciencedirect.com/science/article/pii/B9780444884541500085>.
- [33] E. Strambini et al. “The o-SQUIPT as a tool to phase-engineer Josephson topological materials”. In: *Nature Nanotechnology* 11 (Sept. 2016), 1055 EP -. URL: <https://doi.org/10.1038/nnano.2016.157>.

- [34] F. Vischi et al. “Coherent transport properties of a three-terminal hybrid superconducting interferometer”. In: *Phys. Rev. B* 95 (5 Feb. 2017), p. 054504. DOI: [10.1103/PhysRevB.95.054504](https://doi.org/10.1103/PhysRevB.95.054504). URL: <https://link.aps.org/doi/10.1103/PhysRevB.95.054504>.
- [35] Paul N. Walker, Maria José Sánchez, and Michael Wilkinson. “Singularities in the spectra of random matrices”. In: *J. Math. Phys.* 37.10 (Oct. 1996), pp. 5019–5032. ISSN: 0022-2488. DOI: [10.1063/1.531686](https://doi.org/10.1063/1.531686).
- [36] Paul N. Walker and Michael Wilkinson. “Universal Fluctuations of Chern Integers”. In: *Phys. Rev. Lett.* 74 (20 May 1995), pp. 4055–4058. DOI: [10.1103/PhysRevLett.74.4055](https://doi.org/10.1103/PhysRevLett.74.4055). URL: <https://link.aps.org/doi/10.1103/PhysRevLett.74.4055>.
- [37] H. Weisbrich, G. Rastelli, and W. Belzig. “Geometrical Rabi oscillations and Landau-Zener transitions in non-Abelian systems”. In: *Phys. Rev. Res.* 3.3 (AUG 6 2021). DOI: [10.1103/PhysRevResearch.3.033122](https://doi.org/10.1103/PhysRevResearch.3.033122).
- [38] W. Wernsdorfer, N. E. Chakov, and G. G. Christou. “Quantum phase interference and parity effects in Mn₁₂ single-molecule magnets”. In: *Phys. Rev. Lett.* 95 (2005), p. 037203.
- [39] H. Weyl. “Electron und Gravitation”. In: *Z. Phys.* 56 (1929), p. 330.
- [40] Michael Wilkinson and Elizabeth J. Austin. “Densities of degeneracies and near-degeneracies”. In: *Phys. Rev. A* 47 (4 Apr. 1993), pp. 2601–2609. DOI: [10.1103/PhysRevA.47.2601](https://doi.org/10.1103/PhysRevA.47.2601). URL: <https://link.aps.org/doi/10.1103/PhysRevA.47.2601>.
- [41] Hong-Yi Xie and Alex Levchenko. “Topological supercurrents interaction and fluctuations in the multiterminal Josephson effect”. In: *Phys. Rev. B* 99 (9 Mar. 2019), p. 094519. DOI: [10.1103/PhysRevB.99.094519](https://doi.org/10.1103/PhysRevB.99.094519). URL: <https://link.aps.org/doi/10.1103/PhysRevB.99.094519>.
- [42] Hong-Yi Xie, Maxim G. Vavilov, and Alex Levchenko. “Topological Andreev bands in three-terminal Josephson junctions”. In: *Phys. Rev. B* 96 (16 Oct. 2017), p. 161406. DOI: [10.1103/PhysRevB.96.161406](https://doi.org/10.1103/PhysRevB.96.161406). URL: <https://link.aps.org/doi/10.1103/PhysRevB.96.161406>.
- [43] Zhesen Yang et al. “Dissipative Floquet Majorana Modes in Proximity-Induced Topological Superconductors”. In: *Phys. Rev. Lett.* 126 (8 Feb. 2021), p. 086801. DOI: [10.1103/PhysRevLett.126.086801](https://doi.org/10.1103/PhysRevLett.126.086801). URL: <https://link.aps.org/doi/10.1103/PhysRevLett.126.086801>.
- [44] Tomohiro Yokoyama and Yuli V. Nazarov. “Singularities in the Andreev spectrum of a multiterminal Josephson junction”. In: *Physical Review B* 92.15 (Oct. 2015), p. 155437. DOI: [10.1103/physrevb.92.155437](https://doi.org/10.1103/physrevb.92.155437).
- [45] Tomohiro Yokoyama et al. “Order, disorder, and tunable gaps in the spectrum of Andreev bound states in a multiterminal superconducting device”. In: *Phys. Rev. B* 95 (4 Jan. 2017), p. 045411. DOI: [10.1103/PhysRevB.95.045411](https://doi.org/10.1103/PhysRevB.95.045411). URL: <https://link.aps.org/doi/10.1103/PhysRevB.95.045411>.

- [46] Rui-Xing Zhang and S. Das Sarma. “Anomalous Floquet Chiral Topological Superconductivity in a Topological Insulator Sandwich Structure”. In: *Phys. Rev. Lett.* 127 (6 Aug. 2021), p. 067001. DOI: [10.1103/PhysRevLett.127.067001](https://doi.org/10.1103/PhysRevLett.127.067001). URL: <https://link.aps.org/doi/10.1103/PhysRevLett.127.067001>.
- [47] Rui-Xing Zhang and S. Das Sarma. “Intrinsic Time-Reversal-Invariant Topological Superconductivity in Thin Films of Iron-Based Superconductors”. In: *Phys. Rev. Lett.* 126 (13 Mar. 2021), p. 137001. DOI: [10.1103/PhysRevLett.126.137001](https://doi.org/10.1103/PhysRevLett.126.137001). URL: <https://link.aps.org/doi/10.1103/PhysRevLett.126.137001>.
- [48] Y. X. Zhao et al. “Switching Spinless and Spinful Topological Phases with Projective PT Symmetry”. In: *Phys. Rev. Lett.* 126 (19 May 2021), p. 196402. DOI: [10.1103/PhysRevLett.126.196402](https://doi.org/10.1103/PhysRevLett.126.196402). URL: <https://link.aps.org/doi/10.1103/PhysRevLett.126.196402>.

ACKNOWLEDGEMENTS

First of all, it is a pleasant duty to pay my respect to my supportive supervisor Prof. Yuli Nazarov. His help, wise guidance and overall insights in the field have made this an inspiring experience for me. Second, I would like to thank Zvezdomir Todorov who continuously provided encouragement and always made me feel confident in my abilities. I would like to express my deepest appreciation to Albert Franquet and Pablo Piskunow for the casual coffee breaks outside, on the few sunny days in the Netherlands. Those shared moments allowed me to stay grounded and clear-headed about my stage in life. I feel it is important to pay tribute to Evgeny Repin for the interesting discussions. They were vital in inspiring me to think outside the box, from multiple perspectives to form a comprehensive and objective critique. Special thanks to Thierry van Thiel who was always willing and enthusiastic to assist in any way he could. To conclude, I would also like to extend my deepest gratitude to my family and friends for all the unconditional emotional support during this intense academic venture.

CURRICULUM VITÆ

Hristo Sabev BARAKOV

06-05-1993 Born in Karlovo, Bulgaria.

EDUCATION

2007-2012 High School
Lycée de la langue française Plovdiv, Bulgaria

2012-2015 Bachelors degree Physics
Université Grenoble Alpes, Grenoble, France

2015-2017 Masters degree Quantum matter
Université Grenoble Alpes, Grenoble, France

2017-2022 PhD. Physics
Delft University of Technology, Delft, Netherlands
Thesis: Andreev bound states in potentially topological setups
Promotor: Prof. dr. Yuli V. Nazarov
Promotor: Prof. dr. Yaroslav Blanter

RESEARCH INTERNSHIPS

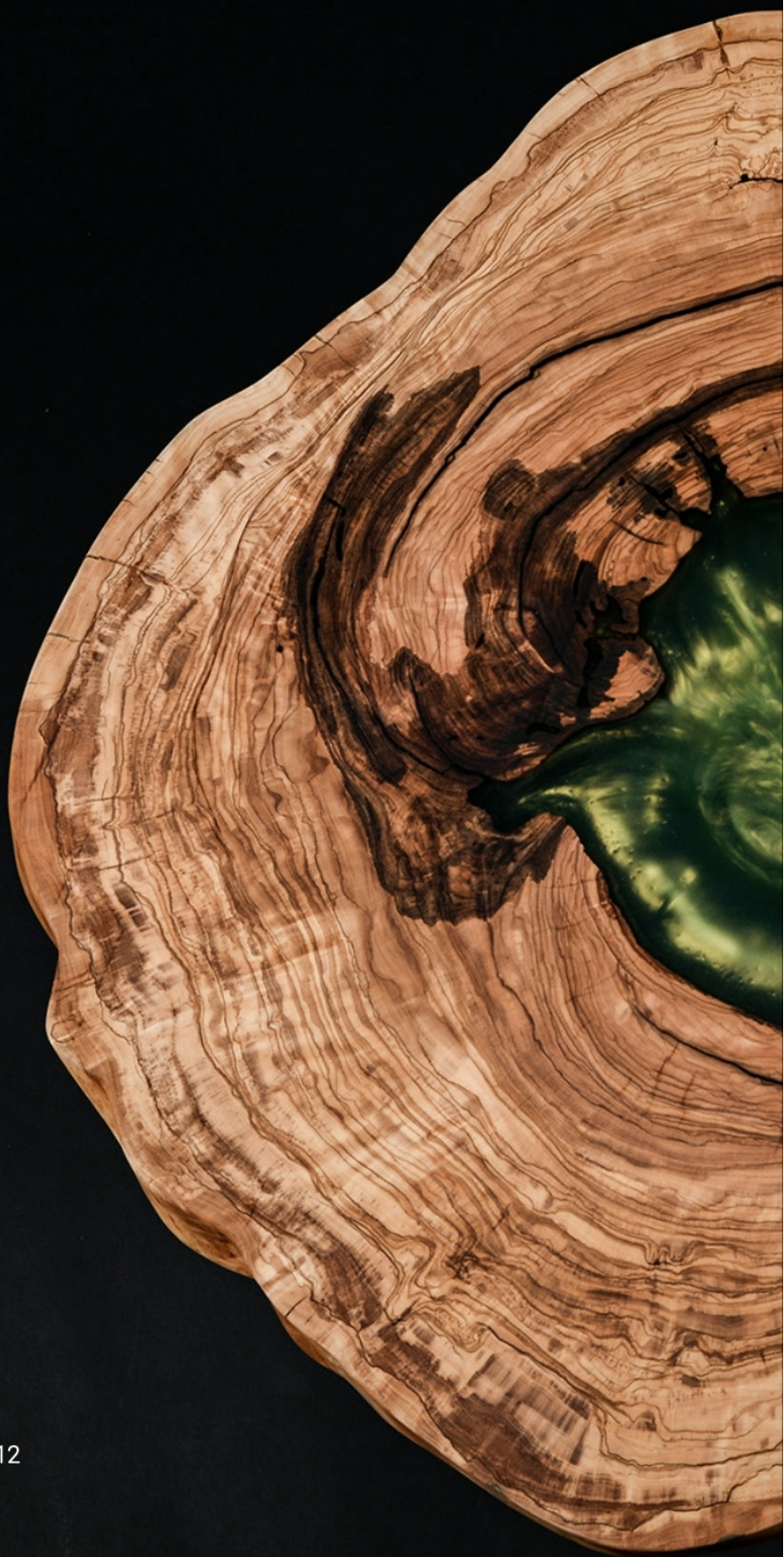
2015 Laboratoire National des Champs Magnétiques Intenses, Grenoble, France
Thesis: Structural properties and superconductivity in FeSe
Supervisor: Dr. Marc-Henri Julien

2016 Université Grenoble Alpes, Grenoble, France
Thesis: Majorana fermions in topological Josephson junctions
Supervisors: Dr. Manuel Houzet and Prof. Dr. Julia Meyer

2017 Chalmers University of Technology, Göteborg, Sweden
Thesis: Spin and pseudospin relaxation times in quantum dot setups
Supervisor: Prof. Dr. Janine Splettstoesser

LIST OF PUBLICATIONS

4. Viktoriia Kornich, **Hristo S. Barakov**, and Yuli V. Nazarov , *Fine energy splitting of overlapping Andreev bound states in multiterminal superconducting nanostructures*, [Phys. Rev. Research](#) **1**, 033004 (2019)
3. Viktoriia Kornich, **Hristo S. Barakov**, and Yuli V. Nazarov , *Overlapping Andreev states in semiconducting nanowires: Competition of one-dimensional and three-dimensional propagation*, [Phys. Rev. B](#) **101**, 195430 (2020).
2. **Hristo S. Barakov**, and Yuli V. Nazarov , *Abundance of Weyl points in semiclassical multi-terminal superconducting nanostructures*, [arXiv:2112.13928](#) (2021) - submitted to PRL.
1. **Hristo S. Barakov**, and Yuli V. Nazarov , *Supercurrent in the presence of direct transmission and a resonant localized state*, [arXiv:2201.07848](#) (2022)



Casimir PhD Series 2022-12
ISBN 978-90-8593-523-0